

**Influences Of Titanium Oxide Additions On The
Electrochromic Properties Of WO₃ Thin Films**

Gui Yang

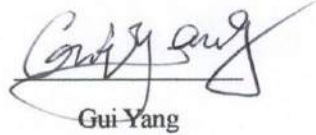
**A THESIS SUBMITTED
FOR THE DEGREE OF Ph.D. OF ENGINEERING
DEPARTMENT OF MATERIALS SCIENCE AND
ENGINEERING
NATIONAL UNIVERSITY OF SINGAPORE**

2015

DECLARATION

I hereby declare that the thesis is my original work and it has been written by me in its entirety. I have duly acknowledged all the sources of information which have been used in the thesis.

This thesis has also not been submitted for any degree in any university previously.



Gui-Yang

2015.03.10

10 March 2015

Acknowledgment

First and foremost, I am sincerely thankful to my supervisor, A/P Daniel John Blackwood, whose encouragement, patient and support from the initial to the final level enabled me to develop an understanding of the project. I am grateful to his invaluable advice, support, detailed instructions and guidance throughout of years of my study. It is extremely pleasant to work with him.

I would like to express my cordial thanks to Dr. Wang Qing and A/P Stefan Adams for their heartily suggestions during my qualification examination. The support from the students and staffs in their research group is mostly appreciated.

I will take this opportunity to appreciate the friendship and support from my group colleagues Dr. Pang Jianjun, Dr. Mohammad Reza Khajavi, Dr. Seyyedhamed Mirabolghasemi, Dr. Liu Dongqing and Tan Yong Teck. I would also like to extend my thanks to my dear friends Cho Swee Jen, Neo Chin Yong, Mei Xiaoguang, Chen Mao Hua, Gu Wen Yi, Yang Zheng Chun, Zheng Min Rui, Tang Chun Hua and Li Kang Le. In addition, I have to give my deepest thanks to all the staffs in MSE department.

Last, but not least, I am especially grateful to my family members for their unconditional love, encouragement and support.

Table of Contents

| | |
|--|-----------|
| DECLARATION..... | 错误!未定义书签。 |
| Acknowledgment..... | iii |
| Table of Contents | iv |
| Summary..... | vi |
| List of Tables | x |
| List of Figures..... | xii |
| List of Symbols | xvii |
| Chapter 1 Introduction..... | 1 |
| 1.2 Brief review of the development of research on electrochromic transition metal oxides | 5 |
| 1.3 Fundamental researches on tungsten oxides..... | 7 |
| 1.3.1 Structural models for amorphous tungsten trioxide | 8 |
| 1.3.2 Crystal structures for tungsten trioxide | 9 |
| 1.3.3 Electrochromic mechanisms for tungsten trioxide crystals | 10 |
| 1.4 Methods of synthesis of tungsten oxide | 11 |
| 1.4.1 Sol-Gel | 11 |
| 1.4.2 Hydrothermal method | 12 |
| 1.4.3 Electrodeposition | 13 |
| 1.4.4 Electrochemical anodization..... | 15 |
| 1.4.4.1 Researches on anodic oxidation of tungsten | 16 |
| 1.4.4.2 Electrochemical anodization mechanism | 18 |
| 1.4.4.3 Effects of anodization parameters on WO ₃ structure | 19 |
| 1.5 Investigations on electrochromism of metal/metal oxide doped WO ₃ films..... | 23 |
| 1.6 Scope of this thesis..... | 26 |
| References:..... | 27 |
| Chapter 2 Experiments Details..... | 36 |
| 2.1 Preparation of Samples Used for Hydrothermal Method | 36 |
| 2.1.1 Substrates cleaning | 36 |
| 2.1.2 Seed layer fabrication..... | 36 |
| 2.1.3 Hydrothermal deposition..... | 37 |
| 2.2 Preparation of Samples Used for Anodic Anodization | 38 |
| 2.2.1 Film deposition by magnetron sputtering..... | 38 |
| 2.2.2 Anodization of W/Ti thin films in organic solution | 39 |
| 2.2.3 Anodization of W/Ti thin films in aqueous solution | 40 |
| 2.3 Characterization..... | 40 |
| 2.3.1 Morphology, Elemental Distribution and Structure Characterization .. | 40 |
| 2.3.2 Electrochemistry Characterization | 41 |
| 2.3.3 Characterization of Electrochromic Feature | 43 |
| References..... | 43 |
| Chapter 3 A self-assembled two-layer structured TiO₂ doped WO₃ film with improved electrochromic capacities | 44 |
| 3.1 Introduction..... | 44 |
| 3.2 Result and discussion | 45 |
| 3.2.1 Morphology and composition analysis | 45 |
| 3.2.2 Structural analysis | 51 |
| 3.2.3 Electrochemical analysis..... | 54 |

| | |
|---|------------|
| 3.2.4 <i>Electrochromic results</i> | 57 |
| 3.2.5 <i>Electrochemical impedance analysis</i> | 65 |
| 3.3 Conclusions | 70 |
| References:..... | 72 |
| Chapter 4 Comparison of WO₃ and TiO₂ doped WO₃ thin films formed by co-anodizing in organic solutions and their electrochromic properties | 75 |
| 4.1 Introduction | 75 |
| 4.2 Results and discussion | 77 |
| 4.2.1 <i>The anodization transient curves</i> | 77 |
| 4.2.2 <i>Morphology observation and corresponding elemental distribution analysis</i> | 79 |
| 4.2.3 <i>Structural analysis</i> | 86 |
| 4.2.4 <i>Raman spectroscopy</i> | 91 |
| 4.2.5 <i>XPS investigation</i> | 94 |
| 4.2.6 <i>Cyclic Voltammetry</i> | 95 |
| 4.2.7 <i>Electrochromic properties</i> | 99 |
| 4.2.8 <i>UV-vis spectroscopy</i> | 106 |
| 4.2.9 <i>Electrochemical Impedance Spectroscopy</i> | 107 |
| 4.3 Conclusions | 109 |
| References:..... | 110 |
| Chapter 5 Studying on influence of different amount of TiO₂ dopants on the electrochromic property of WO₃ | 113 |
| 5.1 Introduction | 113 |
| 5.2 Results and discussions | 115 |
| 5.2.1 <i>Morphology and elemental distribution analysis</i> | 115 |
| 5.2.2 <i>Structural analysis</i> | 122 |
| 5.2.3 <i>Cyclic voltammetry</i> | 130 |
| 5.2.4 <i>Electrochromic properties</i> | 136 |
| 5.2.5 <i>Electrochemical Impedance Spectrum</i> | 143 |
| 5.3 Conclusions | 146 |
| References:..... | 147 |
| Chapter 6 Conclusions | 150 |
| References | 155 |
| Chapter 7 Suggestions on future research work | 156 |

Summary

This thesis aims to investigate TiO₂ doped WO₃ thin films and their corresponding electrochromism properties as a candidate for application on “Smart Windows”. The configuration of the entire thesis includes seven chapters. In chapter 1, a brief introduction on the importance of electrochromic concept and literature review focusing on tungsten oxide based electrochromic materials have been presented. Through reviewing the works done by other scientists, the properties of tungsten oxide and the corresponding development on “Smart Windows” application based on WO₃ system have been exhibited. Through comparing the fabrication methods, the hydrothermal and co-anodization technique provides the advantages and conveniences on producing oxides thin films on the desired substrates with different morphologies. Moreover, to the best of my knowledge, co-anodizing of Ti/W thin film for electrochromic investigation has not been reported except in this thesis. Next, the experimental methods are elaborated in chapter 2, with results and discussion presented in the later chapters. In chapter 2, the specific methods used for the thin film synthesis have been listed. Furthermore, the related characterization and testing conditions have been stated in this chapter as well. In chapter 3, the critical technique used for the synthesis of TiO₂ doped WO₃ thin film is one step hydrothermal method which has the benefit of producing thin films with good crystallinity. In addition, the hydrothermal parameters, containing hydrothermal time, temperature and precursor proportion in

hydrothermal proportions, are easily controlled. The hydrothermally synthesized TiO₂ doped WO₃ thin films show two layer structures consisting of nanopillars on top of a compact layer with uniform Ti/W atomic ratio of 4:1. In the present work, on the one hand, this thin film presents a large light transmittance change range of 67% at 632.8 nm, twice that of an equivalent pure WO₃ film. On the other hand, its coloration efficiency is increased by 50% to 39.2 cm² C⁻¹. Additionally, it is well adhered to the substrate and shows good electrochromic reversibility. In the colored state, the transmittance of the TiO₂ doped WO₃ thin film within visible light range is below 5%, whilst in the bleach state this exceeds 70%.

Continuing the observation from chapter 3 which demonstrates the improved electrochromic property through doping TiO₂ into WO₃ host, chapter 4 also investigates the TiO₂ doped WO₃ thin film but this time the film is produced by the co-anodization of co-sputtered Ti/W thin film in an organic solution. The purpose is to obtain the thin films with different nano-morphologies with improved specific surface area and convenient charge transport channels like pores to further enhance its electrochemical kinetic properties. The synthesized TiO₂ doped WO₃ thin film, with titanium atomic percentage of ca. 10 at.%, shows honeycomb structure with macro-porous surface. The light transmittance change range of this anodized film can reach at 70% at the wavelength of 632.8nm which is 12% higher than an equivalent pure WO₃ thin film. It also

exhibits higher reversibility of 93% and coloration efficiency at a wavelength of 800nm of $64\text{cm}^2/\text{C}$, compared to 73% and $19\text{cm}^2/\text{C}$ for the pure WO_3 thin film.

Based on these improvements on electrochromic properties by doping TiO_2 into WO_3 thin films in chapter 4, chapter 5 studies the effect of different amounts of titanium atoms in the WO_3 matrix on the related morphological, structural, electrochemical and electrochromic properties of the thin films. Furthermore, in this chapter, the pure thin film and the titanium doped thin films are anodized in aqueous acidic solutions, as this is more attractive to industry than an organic solvent. It was observed that the morphology of the thin films undergoes an evolution from nano-pores, nano-flake to nano-block interweaved porous structures accompanying with Ti atomic percentage varies from 0%, 7%, 10% and 15%. The electrochromic experiments demonstrate that the optimum titanium level is 10 at.%, with the TiO_2 doped WO_3 film at this level having a transmittance change range of 58.5%, 72% and 77.7% at 550 nm, 632.8 nm and 800 nm respectively, which is more than a 25% improvement at all wavelengths over a pure WO_3 film formed in the same way. The 10 at.% titanium film also provided shorter coloration/bleach times, especially in the critical near infrared region with values of 10 s/64 s compared with 32 s/90 s of a pure WO_3 thin film. Finally, cyclic voltammetry showed that the addition of titanium improved the film's stability, with the best films losing less than 5% of their capacity after

1000 switching cycles.

Finally, physical characterization of the various electrochromic thin films was also conducted. In all cases, XPS spectroscopy proves that the valence of tungsten and titanium elements in both as prepared pure WO_3 and TiO_2 doped WO_3 thin films were 6+ and 4+ respectively without any traces of alternative valences. In addition, both XRD and Raman results revealed no evidence of separate TiO_2 phases, with indications that the Ti^{4+} replaced W^{6+} within the WO_3 lattice causing a reduction in the structural crystallinity.

List of Tables

Table 3.1 Element distribution list corresponding to the SEM-EDS results

Table 3.2 Lattice parameters of pure WO_3 and Titanium doped WO_3 thin films after refinement

Table 3.3 Influence of wavelength on the coloration efficiency, the coloration and bleaching times and the transmittance modulation range for the two types of film.

Table 3.4 Parameters determined from fitting the EIS data to the equivalent circuit in Figure 3.14, along with the variation between nominally the same films and the percentage fit errors that give an indication of the quality of the fit to an individual film (see Chapter 2).

Table 4.1 List of peak positions for pure WO_3 and TiO_2 doped WO_3 films

Table 4.2 Charge density list of pure WO_3 and TiO_2 doped WO_3 thin films for their first cycle in CV test

Table 4.3 List of optical and kinetic parameters for pure WO_3 and TiO_2 doped WO_3 thin films obtained from Figure 4.13 and 4.14 at wavelengths of 550, 632.8 and 800 nm.

Table 4.4 List of electrochromic rate parameters for pure WO_3 and TiO_2 doped WO_3 at wavelengths of 550, 632.8 and 800 nm respectively

Table 4.5 List of impedance fitting parameters for the pure WO_3 and TiO_2 doped WO_3 thin films

Table 5.1 List of XRD peak positions for WT0, WT7, WT10 and WT15

Table 5.2 Binding energy list of atoms orbits of W4f, Ti2p and O1s for film WT0, WT10, WT10 and WT15

Table 5.3 List of charge densities and charge/discharge rate of all films corresponding to curves in Figure 5.8

Table 5.4 List of optical and kinetic parameters for WT0, WT7, WT10 and WT15 obtained from Figure 5.12 at wavelengths of 550, 632.8 and 800 nm

Table 5.5 List of impedance fitting parameters of film WT0, WT7, WT10 and WT15

List of Figures

Figure 1.1 Schematic of an electrolytic cell used in the electrodeposition process.

Figure 3.1 SEM images of a plan view of (a) TiO₂ doped WO₃ film, (b) pure WO₃ film, a cross-sectional view of (c) TiO₂ doped WO₃ film and (d) pure WO₃ film.

Figure 3.2 SEM-EDS spectrum of TiO₂ doped WO₃ film. (a) Mapping result of a top view and (b) Point distribution of a cross-sectional view of underlayer and nano-pillar respectively. The inset image is the corresponding SEM image.

Figure 3.3. Schematic growth development of the two-layer structured TiO₂ doped WO₃ thin film

Figure 3.4 XRD patterns of pure WO₃ films and TiO₂ doped WO₃ films on FTO substrates. Peaks of Hexagonal WO₃ recorded by ICDD No. 01-085-245g.

Figure 3.5 (a) HRTEM image of TiO₂ doped WO₃ nano-pillar and (b) corresponding elemental distribution maps.

Figure 3.6 Cyclic voltammograms showing the 1st, 100th, 500th and 1000th cycles for (a) TiO₂ doped and (b) pure WO₃ films in 1 M LiClO₄ dissolved in propylene carbonate at a sweep rate of 50 mV s⁻¹.

Figure 3.7 Comparison of (a) intercalated charge density against the number of circles and (b) extracted charge density against the number of circles corresponding to Figure 3.6. Solid squares with TiO₂ dopants, open triangles without TiO₂ dopants. (The values and the corresponding deviation in the image come from the average of the result based on conducting the test twice.)

Figure 3.8 UV-vis transmittance spectrum of the TiO₂ doped (red solid lines) and pure (black dashed lines) WO₃ films in the colored and bleached states.

Figure 3.9 Digital photographs of the TiO₂ doped WO₃ films at different stages: (a) as-prepared; (b) colored at -1.0 V for 30 s; (c) colored at -2.0 V for 30 s; (d) bleached at 2.0 V for 60 s.

Figure 3.10 Chronoamperometry curves and the corresponding in situ transmittance at 632.8 nm for TiO₂ doped WO₃ films (a), (b) and pure WO₃ films (c), (d). Recorded by switching the applied potential repeatedly between -2.0 V and +2.0V vs Ag/Ag⁺ in 1 M LiClO₄ dissolved in propylene carbonate for 60s and 100s respectively. Solid lines show the initial response, dashed lines show the response after 500 cycles.

Figure 3.11 The variation of the *in-situ* change in optical density (ΔOD) versus the charge density for the (a) TiO_2 doped WO_3 films and (b) pure WO_3 films. The ΔOD was measured at 632.8 nm at a potential of -2.0 V Ag/Ag^+ . (Note that the deviation of the CE is calculated based on the Figure 3.10(b). In Figure 3.10(b), the transmittance - time curve of TiO_2 doped WO_3 has four cycles, so each cycle gives a value of CE, based on these values an average deviation of the CE of TiO_2 doped WO_3 is obtained and shown in the above image. The value of 23.8 is the average value of the four values of CE. The CE deviation of pure WO_3 is obtained with the same method.)

Figure 3.12 *in situ* transmittance at 500nm (solid line), 632.8 nm (dashed line) and 1200nm (dot-dash line) for pure WO_3 films (a) and TiO_2 doped WO_3 films (b).

Figure 3.13 Nyquist plots for WO_3 films with (a) and without (b) TO_2 dopants at -0.4V vs Ag/Ag^+ 1 M $LiClO_4$ dissolved in propylene carbonate. (c) Magnification of the high frequency region for the pure WO_3 film.

Figure 3.14 Equivalent circuit used to fit the impedance data of WO_3 films both with and without TiO_2 dopants.

Figure 4.1 Characteristic anodization profiles of pure W and Ti/W thin film in 0.3 M NH_4F solution dissolved in ethylene glycol/DI water solution (volume ratio of 50:2). The anodize potential was increased from 0 V to 10 V at 50 mVs^{-1} and fixed at 10 V for 40 minutes.

Figure 4.2 elemental distributions of pure WO_3 film and TiO_2 doped WO_3 film detected by SEM-EDS. Accordingly the titanium contributes 10 at.% of the metallic component.

Figure 4.3 SEM images of (a) top and (b) cross section view for sputtered pure W on conductive FTO glass and likewise (c), (d) for the co-sputtered Ti/W.

Figure 4.4 SEM images of films formed by anodization (a) Pure WO_3 thin film top view; (b) TiO_2 doped WO_3 (10 at.% Ti) thin film top view; (c) Pure WO_3 thin film top view cross section; (d) TiO_2 doped WO_3 thin film cross section; (e) TiO_2 doped WO_3 thin film bottom view. All these anodized film images were captured after annealing at 450°C for 3 hours

Figure 4.5 Comparison of the XRD results before and after anodization of W thin films with and without titanium. (Cubic structure* is indexed from ICDD 00-001-1204).

Figure 4.6 Comparison of the XRD results of pure WO_3 and TiO_2 doped WO_3

thin film formed by anodization after annealing at 450°C for 3h. The peaks passed through by dash lines belong to FTO substrate.

Figure 4.7 High-resolution TEM image of (a) Pure WO₃ thin film formed by anodization after scratching from FTO substrate and being dispersed in ethanol on to a Cu grid. The inset is the region outlined by a square after performing a reversed Fourier transform; (b) diffraction image corresponds to (a); (c) TiO₂ doped WO₃ thin film after the same process as pure WO₃ and (d) diffraction image corresponding to (c)

Figure 4.8 Raman spectra of Pure WO₃ thin film and TiO₂ doped WO₃ thin film.

Figure 4.9 XPS spectra of the orbits of (a) W 4f, (b) O 1s and (c) Ti 2p

Figure 4.10 Cyclic voltammetry curves of (a) Pure WO₃ thin film and (b) TiO₂ doped WO₃ thin film. The CV is conducted in 1M LiClO₄ dissolved in propylene carbonate solutions with a sweep rate of 50mV s⁻¹ from -2V to 1V vs. Ag/Ag⁺. The solid line “—” denotes the first cycle; dash line “-----” denotes the 500th cycle and dotted line “.....” denotes the 1000th cycle.

Figure 4.11 Comparison of inserted ion charge density at selected cycle numbers corresponding to the cyclic voltammetry curves of pure WO₃ and TiO₂ doped WO₃ thin film.

Figure 4.12 Chronoamperometry curves of pure WO₃ and TiO₂ doped WO₃ thin films. The test is conducted by providing alternative potentials between -1 V and 1 V vs. Ag/Ag⁺ (0.1M AgNO₃/0.01M TBPA in acetonitrile) for 50 s and 150 s respectively in 1 M LiClO₄ dissolved in propylene carbonate solutions.

Figure 4.13 (a), (b) and (c) are *in-situ* UV-vis kinetic curves corresponding to Figure 4.12. The black and red solid line “—” represent $\Delta T\% \sim \lambda$ features of the TiO₂ doped WO₃ thin film at the first and the last five cycles of 500 cycles respectively; the dash line “-----” represents pure WO₃ thin film at its first five cycles

Figure 4.14 (a), (b) and (c) are the related coloration efficiency at different wavelengths. The filled square “■” represents the coloration efficiency of pure WO₃; empty square “□” for TiO₂ doped WO₃ at the 1st cycle and the filled triangular “▲” for TiO₂ doped WO₃ at the 500th cycle

Figure 4.15 UV-vis spectra of pure WO₃ and TiO₂ doped WO₃ thin films in their bleached and colored states and their corresponding optical images. “O” stands for original state (i.e. before coloration); “C” for color state (after coloring under -1 V for 50 s) and “B” for bleach state (after bleach under 1 V for 150 s”). The

solid line “—” denotes TiO₂ doped WO₃ thin film and the dash line “- - -” represents pure WO₃ thin film.”

Figure 4.16 Electrochemical impedance spectra of the pure WO₃ and TiO₂ doped WO₃ thin films. The solid line is the fitting results, for the equivalent circuit shown in Figure 3.14.

Figure 5.1 SEM images (a) top view and (b) cross section of as-sputtered pure tungsten thin film. The morphologies of the as-sputtered tungsten/titanium thin films with different atomic percentage of titanium do not show significant variations from the pure WO₃.

Figure 5.2 SEM top images of (a) WT0, (b) WT7, (c) WT10 and (d) WT15 films. All these films were anodized in 0.3 wt% NaF dissolved in 1 M H₂SO₄ under 40 V for 40 mins and annealed at 450°C for 3 h.

Figure 5.3 SEM cross section images of (a) WT0, (b) WT7, (c) WT10 and (d) WT15 films. All these films were anodized in 0.3 wt% NaF dissolved in 1 M H₂SO₄ under 40 V for 40 mins and annealed at 450°C for 3 h.

Figure 5.4 Anodic current density transients for W/Ti films in 0.3 wt% NaF Dissolved in 1 M H₂SO₄ under a sweep potential rate of 1 V s⁻¹ for 40 s to a fixed potential of 40 V for 40 min.

Figure 5.5 XRD patterns for WT0, WT7, WT10 and WT15.

Figure 5.6 Raman spectra of WT0, WT7, WT10 and WT15

Figure 5.7 Comparison of XPS spectrum of thin film WT0, WT7, WT10 and WT15 (a) W4f orbit, (b) O1s orbit and (c) Ti2p orbit

Figure 5.8 Cyclic voltammograms collected on their 1st, 500th and 1000th cycle in 1M LiClO₄ dissolved in propylene carbonate at a sweep rate of 50 mV s⁻¹ from -2V to 1V vs. Ag/Ag⁺ for (a) WT0, (b) WT7, (c) WT10, (d) WT15.

Figure 5.9 Comparison of cyclic voltammograms corresponding to figure 6.8 at their respective (a) first cycle and (b) the 1000th cycle

Figure 5.10 Charge accommodation capacities of WT0, WT7, WT10 and WT15 at their 1st, 500th and 1000th cycle respectively calculated from the result of Fig 5.8.

Figure 5.11 Comparison of chemical diffusion coefficient calculated from the respective cyclic voltammograms at their first cycle based on the Randles-Sevcik

equation.

Figure 5.12 Chronoamperometric measurements performed by applying alternative potentials of -1 V for 50 s followed by 1 V for 150 s, i.e. coloration and bleaching respectively, in 1M LiClO₄ dissolved in propylene carbonate.

Figure 5.13 Photo images of the films at their colored (left) and bleached (right) states. The films are placed in traditional three electrode cell containing 1M LiClO₄ dissolved in propylene carbonate and supplied negative potential of -1 V for 50 s, followed by positive potential of 1 V for 150 s. The suffix character of C or B in the figure denotes color and bleach state respectively.

Figure 5.14 *In situ* transmittance corresponding to Figure 5.10 recorded at a wavelength of (a) 550nm, (b) 632.8nm and (c) 800nm.

Figure 5.15 Plots of the variation of the *in situ* optical density vs. the charge density corresponding to the *in situ* transmittance in Figure 5.12 at wavelengths of (a) 550 nm, (b) 632.8 nm and (c) 800 nm

Figure 5.16 Impedance spectrums of WT0, WT7, WT10 and WT15. The squares are the raw data collected and the solid lines are the fitting results

List of Symbols

| | |
|----------------------|--|
| a- | Amorphous |
| AAO | Aluminum oxide |
| Ag/Ag ⁺ | 0.001M AgNO ₃ plus 0.1M tetrabutylammonium perchlorate dissolved in acetonitrile |
| AFM | Atomic force microscopy |
| CA | Chronoamperometry |
| CE | Coloration Efficiency |
| CV | Cyclic voltammetry |
| CVD | Chemical Vapor Deposition |
| DI | Milli-Q water (resistivity ~10 MΩ•cm) |
| e ⁻ | Electron |
| EC | Electrochromic Window |
| EDS | Energy-dispersive X-ray Spectroscopy |
| EIS | Electrochemical impedance spectroscopy |
| FESEM | Field Emission Scanning Electron Microscopes |
| FTIR | Fourier transform infrared |
| FTO | Fluorine coated tin oxide glass |
| HRTEM | High Resolution Transmission Electron Microscope |
| I ⁺ | Small cation ion |
| M ⁺ | H ⁺ , Li ⁺ , Na ⁺ and K ⁺ |
| Me | Transition metal |
| NIR | Near Infrared |
| PEG | Polyethylene Glycol |
| PVA | Polyvinyl Alcohol |
| <i>q</i> | Injected or ejected charge density |
| <i>r_b</i> | Bleaching Rate |
| <i>r_c</i> | Coloration Rate |
| RMS | Root Mean Square |

| | |
|-------------|--|
| SEM | Zeiss Field Emission Scanning Electron Microscope |
| SHE | Standard hydrogen electrode |
| T_b | Transmittance before coloration at a given wavelength |
| T_c | Transmittance after coloration at a given wavelength |
| TEM | JEM3010 F transmission electron microscope |
| TG | Thermogravimetric analysis |
| UV | Ultraviolet |
| UV-Vis | Ultraviolet-Visible light spectroscopy (Shimadzu UV-Vis 1800 spectrometer) |
| XPS | X-ray Photoelectron Spectroscopy |
| XRD | X-ray Diffraction |
| τ_c | Coloration Switching Time |
| τ_b | Bleaching Switching Time |
| ΔOD | Change in optical density |
| ΔT | Transmittance Change/light modulation |
| λ | Wavelength |

Chapter 1 Introduction

Nowadays, saving energy, which is more efficient than finding new ways of energy generation, is critical for sustainable development of the world. In tropical countries like Singapore, providing comfortable working environment requires high cost on air-conditioning systems to resist on heating due to the transmission of infrared (IR) light through window. Nevertheless the aesthetically pleasing attribute of glass still warrants its widespread usage in building construction. Therefore, investigations on “Smart Window” materials, which can simultaneously impart energy efficiency and augment human comfort by controlling the throughput of both solar radiation and visible light into buildings, can greatly reduce energy consumption and thus raised interest in energy efficiency research. Such “Smart Windows” hold out the promising prospect of allowing the wide usage of glasses without the drawback of solar heating.

The critical technique applied on “Smart Windows” is to add a controllable layer of thin film which can regulate the incoming solar flux by blocking the transmission of IR keeping rooms cool yet still allowing good visibility due to its reversible color change. There are two advantages on “Smart Windows”: firstly, only a small voltage needs to be applied so it can be considered energy saving; secondly, it can regulate both the indoor light and temperature by

adjusting transmittance to different levels when required.

At present, there are a wide range of options for producing “Smart Windows” including electrochromic windows, gasochromic windows and thermochromic windows. Among all these, electrochromic windows are favorable in tropical conditions for their guarantee on controlling solar light flux input while providing better visual lighting inside of the buildings.

The electrochromic window is named under its chromic mechanism called electrochromism. This phenomenon can be observed with a series of materials which exhibit the property of reversible color change upon being imparted a burst of electrical charges. Because of such unique behavior, these electrochromic materials, fabricated by different method, have been investigated to capitalize on their exceptional capability.

1.1 A brief history of electrochromism

History of the electrochromic materials involved many famous scientists and started as early as in 1704, when Diesbach firstly discovered Prussian blue in the laboratory of Dippel in Berlin. ^[1] In 1815 Berzelius showed that pure WO_3 , which is pale yellow, changed color when reduced by warming under a flow of

dry hydrogen gas ^[2] and in 1824 Wohler effected a similar chemical reduction with metallic sodium.^[3]

Different applications of such useful material property soon followed suit. An early form of photography, which is a ubiquitous example of a photochromic color change involving electron transfer, was devised in 1842 by Sir John Frederick William Herschel for technological application. ^[4] This technique involved generation of Prussian blue $\text{KFeIII}[\text{FeII}(\text{CN})_6](\text{s})$ from moist paper pre-impregnated with ferric ammonium citrate and potassium ferricyanide, forming yellow Prussian brown $\text{Fe}^{3+}[\text{Fe}(\text{CN})_6]^{3-}$ or $\text{FeIII}[\text{FeIII}(\text{CN})_6]$. Wherever light struck the photographic plate, photo reduction of FeIII yielded FeII in the complex, hence Prussian blue formation. Herschel called his method ‘cyanotype’. By 1880s, the so-called ‘blueprint’ paper had already been manufactured on a large scale. Soon after Herschel’s work, Bain patented a primitive form of fax transmission that again relied on the generation of a Prussian blue compound.^[5] Probably the first suggestion of an electrochromic device involving electrochemical formation of color was presented in a London patent of 1929, which concerned the electrogeneration of molecular iodine from iodide ion.^[6] One year later, Kobosew and Nekrassow reported the first recorded color change following electrochemical reduction of solid tungsten trioxide.^[7] By 1942 Talmay had a patent for electrochromic printing called electrolytic writing paper involving MoO_2 and/ or WO_3 .^[8-9] In 1951, Brimm *et al.* extended

their work to effect reversible color changes, for Na_xWO_3 immersed in 1 mol dm^{-3} sulfuric acid.^[10] Two years later, Kraus elaborated the basis of a display using the reversible color-bleach behavior of WO_3 immersed in sulfuric acid.^[11]

In the early 1960s, Philips developed commercial electrochromic products utilizing an aqueous organic viologen. Their first patent dated from 1971 and published academic paper in 1973.^[12-13] However, the first widely accepted suggestion of an electrochromic device should be attributed to Deb, who in 1969 formed an electrochromic color by applying an electric field of 104 V cm^{-1} across a thin film of dry tungsten trioxide vacuum deposited on quartz.^[14] In 1971, Blanc and Staebler produced an electrochromic effect superior to most prior arts by applying electrodes to the opposing faces of doped crystalline SrTiO_3 and observed an electrochromic color move into the crystal from the two electrodes.^[15] The following year, Beegle developed a display of WO_3 having identical counter and working electrodes, with an intervening opaque layer.^[16]

Nowadays most workers make reference to Deb's later paper, which dated from 1973, as the true birth of electrochromic technology with a film of WO_3 immersed in an ion-containing electrolyte.^[17] In 1975, Faughnan *et al.* of the RCA Laboratories in Princeton reported WO_3 undergoing reversible electrochromic color changes while immersed in aqueous sulfuric acid in a key review paper.^[18] Mohapatra of the Bell Laboratories in New Jersey published

the first description of the reversible electro-insertion of lithium in 1978.^[19] In 1979, Diaz *et al.* developed the first account of an electrochromic conducting polymer by synthesizing of thin film poly(pyrrole).^[20]

In this thesis the electrochromic material of interest is focused on transition metal oxides and there have been many reports on the electrochromic properties and uses of transition metal oxides in the scientific literatures, such as tungsten trioxide (WO₃), titanium oxide (TiO₂), molybdenum oxide (MoO₃) and niobium (Nb₂O₅).^[21-22]

1.2 Brief review of the development of research on electrochromic transition metal oxides

Electrochromism arises from ion intercalation/de-intercalation processes which can be defined schematically by:

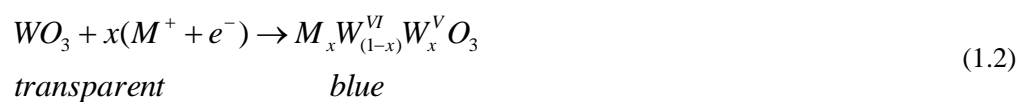


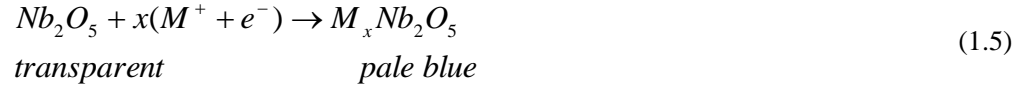
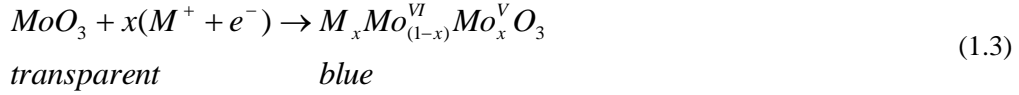
where Me, I⁺ and e⁻ and n denote a metal atom, a singly charged small ion such as Li⁺ or H⁺ and an electron and n is a variable parameter related to specific type of oxide. For example, the value of n is 3 for defect perovskites, 2 for rutile, 1.5 for carborundums and 1 for rock-salts.^[22] Accompanying with this ion insertion/extraction, the electrochromic layer can regulate the optical transmittance reversibly and persistently associating with coloring/bleaching

processes by alternated potential polarity.

Various electrochromic materials have been investigated and these can be classed into two main categories. The first is the inorganic transition metal oxides and the second are organic materials, which accomplish the process of color change by electrochemical redox reactions such as viologen, 1,1'-Diheptyl-4,4'-bipyridinium and some conductive polymers. [23] As compared to the inorganic materials, the organic electrochromic materials, show advantages in short response time, easy molecular design and relatively high coloration efficiency. However, they also have limitations such as poor reliability and UV instability results in irreversible side reactions that are a major limitation for their applications. [24-25]

The electrochromic transition metal oxides can be further divided into three subcategories based on their crystal structure: perovskite-like, rutile-like, and layer and block structure. Alternatively these inorganic electrochromic materials can be classified as being cathodic or anodic, depending on whether coloration occurs when the material is acting as a cathode or an anode. The oxides of Ti, Nb, Mo, Ta and W are all cathodic with coloration occurring with the insertion of positive ions: [26]





where $M^+ = H^+, Li^+, Na^+, \text{ or } K^+$ and $0 < x \leq 1$.

Through comparing with other transition metal oxides, WO_3 shows the most promising prospects for commercial electrochromic displays and smart windows by virtue of its appearance, response time, charge consumption, reliability and manufacturing yield.^[27-34] Therefore there are a great number of investigations on WO_3 which are focused on its morphology of nanostructure,^[35] fundamental electrochromic principle and widespread applications.^[36-37]

1.3 Fundamental researches on tungsten oxides

Tungsten oxide, which is an n-type indirect band gap semiconductor, has proven to be the most favored transition metal oxide alternative for application in electrochromic displays or “Smart Windows”.^[38-39] Because that the band gap of WO_3 is usually reported as 2.7 eV, however, it can vary from 2.4 eV (cubic ReO_3 structure) to 3.15eV (orthorhombic WO_3 crystal), which lead to high transparency of tungsten trioxide deposited windows.^[40-42] With the rapidly escalating research on semiconductor nanostructures, the texturing of WO_3 by

different methods is also the subject of more attention for the purpose of further enhancing its electrochromic performance.

1.3.1 Structural models for amorphous tungsten trioxide

Non-crystallite/amorphous tungsten trioxide (α - WO_3) films with characteristic electro- and photo-chromic abilities have been extensively investigated in the past years and several structural models have been proposed. According to the literatures, arranged in chronology, in 1977 Zeller and Beyelek pointed out traces of corner sharing WO_6 octahedra information by analyzing their XRD results. ^[33] Later, Shiojiri *et al* and Kaito *et al*, one after the other, observed under TEM that the WO_3 film consisted of micro crystallites with sizes 10-30 Å. ^[43-44] In 1987, Ramans *et al.* ^[45-46] claimed the film consisted of clusters which were formed through three to eight WO_6 octahedral sharing their edges and corners, with Raman spectroscopy showing evidence of $\text{W}=\text{O}$ bonds. In addition, these authors suggested a layered structure similar to the findings in MoO_3 system. ^[47] In the meantime, Arnoldussen suggested that their amorphous WO_3 films formed by evaporation consisting of trimetric W_3O_9 molecules were bonded weakly to each other by water bridges, as well as hydrogen and van der waals bonding. ^[48] In 1989, Nanba & Yasui investigated the microstructure of amorphous WO_3 thin films in further details. They analyzed quantitative water content in their films using TG & FTIR and pointed out $\text{WO}_3 \cdot 1/3\text{H}_2\text{O}$ cluster models in these amorphous WO_3 films. ^[49] In recent years, the

transformation of WO_3 from amorphous to crystalline has been investigated through annealing the film under different temperatures, with Ozkan *et al.* finding that when the annealing temperature is increased to 390°C , the amorphous structure of WO_3 can still be seen. However, after annealing at 450°C , only monoclinic crystalline WO_3 can be found. ^[50]

1.3.2 Crystal structures for tungsten trioxide

Tungsten trioxide shows a perovskite-like (ReO_3) atomic configuration comprising corner sharing with WO_6 regular octahedral. In this structure, the W atom is positioned at the center of an octahedron constructed by O atoms located at the corners. However, respective to the ideal ReO_3 cubic structure the symmetry is lowered by two distortions: one originates from the tilt of the WO_6 octahedral and the other is the deviation of tungsten atom away from the center of the octahedron. ^[51]

These distortions, occurred as a consequence of the phase transitions, are observed in crystal structures of WO_3 . However, the magnitude of the spontaneous distortions is reported to be dependent on the process temperature. As the temperature is increased from -189°C to 900°C , the structures of the single crystals of pure WO_3 are transformed following a sequence of monoclinic \rightarrow triclinic \rightarrow monoclinic \rightarrow triclinic \rightarrow tetragonal, accompanying with the

space group transitions of Pc (monoclinic) ($Z = 4$, D, 230 K) \rightarrow (triclinic) ($Z = 8$, D, 300 K) $\rightarrow P2_1/n$, (monoclinic) ($Z = 8$, C, 623 K) $\rightarrow Pbcn$, (orthorhombic) ($Z = 8$, D, 973 K) $\rightarrow P2_1/c$ (monoclinic) ($Z = 4$, C, 1073 K) $\rightarrow P4/ncc$ (tetragonal) ($Z = 4$, C, > 1173 K) $\rightarrow P4/nmm$, (tetragonal) ($Z = 2$), where D and C denotes discontinuous and continuous transitions respectively and the temperatures are the transition points. ^[52] Therefore, the electrical and optical performance of tungsten oxides is greatly influenced by the change of crystal phases. According to the literature, the monoclinic structure is the most stable form at room temperature and the orthorhombic phase will be formed when temperature rises to 330°C . This orthorhombic structure can be maintained even as the temperature is increased to 740°C . The phase boundary regions from monoclinic to orthorhombic is recognized as the WO_6 octahedron tilting caused by the shift of tungsten atoms ascribed to a decrease in the W-O displacement at the (001) orientation. ^[53] However, according to the recent studies, the monoclinic structure is obtained after annealing samples at 450°C, followed by natural cooling to room temperature. ^[54-56]

1.3.3 Electrochromic mechanisms for tungsten trioxide crystals

The widely accepted electrochromic mechanism for crystalline WO_3 is a Drude-like free electron absorption with a behavior very similar to a heavily doped semiconductor with ionized impurities. ^[57] This model, used for explaining the electrochromic property in crystalline WO_3 system, is built on a double injection

of electrons and ions. It proposes that the inserted ions and electrons would like to occupy the extended state of the WO_3 band structure, which are in the band gap and could be caused by the variations in bond lengths and angles, grain boundaries or strain effects, and be scattered by impurities inducing high reflectance in the IR range. [58-59]

1.4 Methods of synthesis of tungsten oxide

1.4.1 Sol-Gel

Sol-gel reaction was first discovered in the late 1800s and intensively investigated since the early 1930s. [60-61] According to literatures, most of hydrated tungsten oxides films are synthesized by sol-gel methods and heat treatment is usually required for producing WO_3 with crystal structure. [49]

The most popular precursors for WO_3 sol preparation are tungstic acid and peroxotungstic acid solutions in aqueous system. [62-68] The tungstic acid solution is usually prepared by acidifying sodium tungstate solution, [69] while the peroxotungstic acid by resolving pure tungsten in 30wt%~35wt% hydrogen peroxide to form $[\text{WO}_2(\text{O}_2)\text{H}_2\text{O}].n\text{H}_2\text{O}$ complexes. [70] The precipitates, formed during the aging process in the tungstic acid solution, are ascribed to the condensation of the intermediates due to the hydrolysis of H_2WO_4 . The same agglomerates in the form of $\text{WO}_3.n\text{H}_2\text{O}$ are observed during the gelation of

peroxotungstic acid solution and a series of organic acids, assisting in the gelation, need to be added into the solution at 50°C-60°C for 24h-48h. [71]

Despite the advantages of the sol-gel method in synthesizing materials with desired structures, this method exhibits some drawbacks including long processing time, difficulties in removing organic residuals completely and large shrinkage related to the gelation processes.

1.4.2 Hydrothermal method

In the case of the hydrothermal technique, it shows advantages in scalability (such as a commercial-scale hydrothermal process for culturing quartz crystals), low energy consumption, reduced process steps, utilization of water as solvent and low precursor cost. [72-73] However, the requirement for safe operation of a large pressure vessel that needs to be combined with a high aggregation rate currently hinders wider use of this technique.

Generally, the synthesis of WO₃ film consists of precursor solutions such as H₂WO₄, WCl₆ or Na₂WO₄ solution, followed by addition of chelating ligands or capping agent such as inorganic chemicals of Li₂SO₄, (NH₄)₂SO₄, or NaCl [74-78] and organics of polyethylene glycol (PEG), polyvinyl alcohol (PVA), sulfates and oxalic acid for obtaining the crystals with desired shape. [72, 79-87]

By now, different morphologies of WO₃ film have been reported through the hydrothermal method, such as one dimensional nano-wires and nano-rods;^[79-80, 83-84] two dimensional nano-belts and nano-plates.^[85-86]

Besides the capping agents, other hydrothermal parameters also play important roles in shaping and controlling the morphologies. These parameters are pH of hydrothermal solution, hydrothermal temperature and period, even the order of adding precursors. All these conditions show different influences on the property of the obtained materials.^[87]

In 2009 Zhao *et al.*^[87] composed varieties of WO₃ with different morphologies that evolved from hollow spheres, then hollow boxes and finally to nanotubes originated from the prototype of hollow structures of tungstic acid. They achieved the synthesis via the hydrothermal method through regulating the component proportions in the solution, which consisted of WCl₆/urea/ethanol system, as well as altering the experimental factors like hydrothermal temperature, duration and pH value.

1.4.3 Electrodeposition

Another commonly used liquid phase reaction is electro-chemical deposition method, which is an effective way to produce coatings on the desired substrate

from the aqueous solutions. A schematic description for an electro-chemical deposition set up is shown in Figure 1.1.

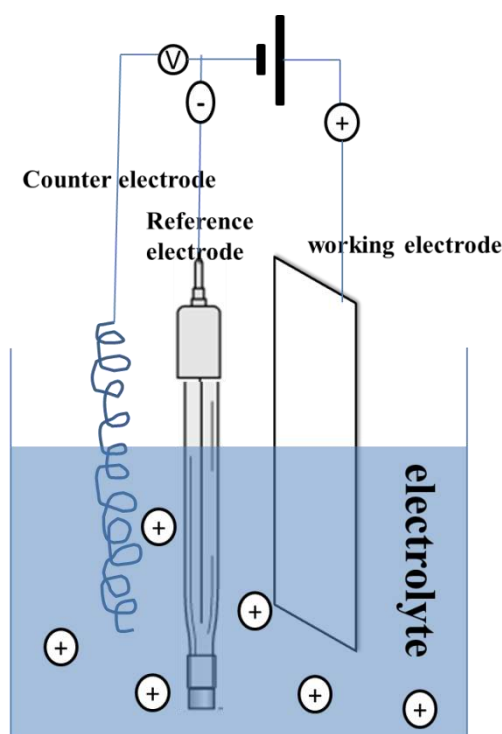


Figure 1.1 Schematic of an electrolytic cell used in the electrodeposition process.

According to the literatures, the most favored electro-deposition precursor solution for WO_3 is peroxotungstic acid. However, this peroxotungstic acid is highly unstable and forms precipitations through condensation reactions within several hours. Therefore, alcohols like iso-2-propanol or ethanol is usually added into the peroxotungstic acid solution to react with it and form a peroxotungstic ester. The produced peroxotungstic ester is soluble and can be kept for up to 2 weeks under the same conditions.^[88] Additionally, a lamellar structure of WO_3 is reported by Baeck *et al.* through adding sodium dodecyl sulfate into the electrodeposition solution. Besides, this observed lamellar phase exhibits not only enhancements on photocatalytic activity, but also greater

current density for hydrogen intercalation due to its larger surface area and facilitated charge transport channels ascribed to its mesoporous morphology, that are beneficial for electrochromism.^[89] Wang *et al.* has reported nanoballs morphology of WO₃ thin film with diameters ranging from 40nm to 350 nm, which is achieved by electrodepositing from the aqueous tungstic solution.^[90]

However, the electrodeposition method faces difficulty in obtaining thin films with even surface and equal thickness, especially with porous structures. In order to achieve this purpose of producing WO₃ thin film with ordered pores, the electrochemical anodization method can be used.

1.4.4 Electrochemical anodization

Anodizing is an electrolytic passivation process for the purpose of increasing the thickness of the oxide layer on metallic surfaces. This method has long been used as a metallic surfaces finishing technique on the industrial scale.^[91]

Initially, this method was only used for obtaining a compact oxide layer on the metallic surface for protection. However, in recent years the formation of ordered porous morphologies have been found and many self-ordered nanoporous structures were reported in the early 90's, such as porous silicon and porous alumina.^[92-94] Since then, other valve metals, like Ti, Ta, Zr, Cd and Bi, have been investigated as well.^[92, 95-100]

The formed nano-structures of these investigated materials can significantly enhance their properties and extend the range of their applications due to drastically increased surface areas. ^[54, 101-104] The nano-porous architecture can also reduce resistances to mass and charge transport compared with bulk materials for energy storage devices, such as batteries or electrochromic windows. ^[101, 103]

By comparing with the other methods mentioned above for fabricating WO₃ films, electrochemical anodization can synthesize the most ordered nano-porous architectures with high ratio of surface to volume and advanced characters on electro-optical aspects. ^[105] In addition, the anodization parameters that are in charge of controlling and modulating the morphology of the desired nano-porous structures are easily tuned. Furthermore, the resulting nano-porous oxide film exhibits good conformability and uniformity for large area applications. ^[106-107] Besides, combining with other physical methods like magnetron sputtering, it is convenient to produce various oxide films with ordered nano-porous structures on various substrates which significantly broadens the film applications, especially for uses such as “Smart Windows”. ^[108]

1.4.4.1 Researches on anodic oxidation of tungsten

The first report on producing nanoporous WO₃ by electrochemical anodization

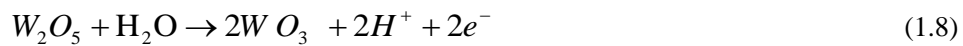
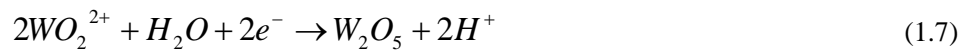
method in 2003, realized under galvanostatic mode in the oxalic acid electrolyte, was not satisfactory due to its lack of thickness (150 nm) and non-uniform nanoporous structures. ^[109] Subsequently, more WO₃ films with good uniformity and desired thickness were synthesized by anodizing tungsten foil in fluoride containing solutions, which can accelerate the etching rate during the anodizing process. ^[102-103, 105] Particularly, Tsuchiya *et al.* demonstrated their self-organized nano-porous WO₃ film with thickness of approximate 500 nm through the anodization of W foil under potentiostatic mode in NaF electrolyte. ^[102] Later on, Zheng *et al.* successfully transferred this method to apply it on conductive glass by anodizing a tungsten film sputtered on a FTO substrate through magnetron sputtering technique. This latter film greatly improved electrochromic efficiencies in comparison with WO₃ sputtered directly on the same substrate. The enhancement on the efficiency was ascribed to the formed macro-porous structure. ^[110] However, due to hazards associated with using HF, handling of the chemicals and the experimental protocol must be in accordance with applicable risk management practices.

Soon afterwards, various investigations on the anodized WO₃ were reported and were focused on different aspects including anodizing mechanism, potentials, duration, substrates, electrolyte, heat treatment and temperatures, even film thickness and so on. ^[108, 111] All these conditions were important for controlling the pore size in order to get optimized electrochromic properties.

1.4.4.2 Electrochemical anodization mechanism

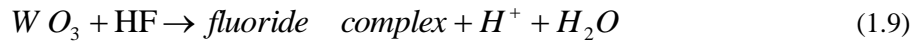
Recently, numerous efforts have been made in order to explore the mechanism of the electrochemical growth of WO_3 by using the anodization technique.^[112] However, unfortunately, experimental evidence is still lacking to substantiate the presently proposed model or theory. According to previous investigations on the anodization mechanisms of producing porous oxides, there are two main theories that need to be discussed. One is deduced from the anodization of nanoporous aluminum oxide (AAO). According to the work reported by Jessensky *et al.*,^[113] the anodic aluminum oxide with pores is formed via a two-step process, with first step being metal oxidation under an applied electric field and followed by oxide dissolution step in anodic electrolyte.

Although this analogous process is also used for explaining the tungsten anodization process, there are still discrepancies between aluminum and tungsten, such as the role of fluoride ions in pore formation processes during anodization of tungsten. Hence, another more favored and accepted proposition is that the anodic growth of tungsten includes series of oxides at the metal/metal oxide interface based on the following reactions:^[114]



Simultaneously, the dissolution of produced tungsten oxides will be dissolved

into the electrolyte by the formation of fluoride complexes: ^[115]



From above description it can be concluded that the competition between oxidation rate, which is determined by the magnitude of the external applied voltage, and the dissolution rate, controlled by amounts of F⁻ in the solution, is the prerequisite conditions for the pore formation. With the reactions going on, eventually, a balance will be established between the oxidation rate and dissolution rate to arrive at a steady state condition, under which the oxidation rate equals to the dissolution rate. This mechanism of the anodic growth of WO₃ is recommended by various researchers based on the experimental results, hence is widely accepted. ^[101-102, 116]

1.4.4.3 Effects of anodization parameters on WO₃ structure

I. Anodization electrolyte

Over the past 35 years, numerous researchers found that a compact layer of tungsten oxide will be formed during anodization of tungsten in H₃PO₄ solutions, which may imply the involvement of other anions coming from the electrolyte into the film. ^[117-138] Later on, Mukherjee *et al.* and Tsuchiya *et al.* have reported the formation of nano-porous structure of WO₃ by anodizing in oxalic acid solution and sulphate-fluoride electrolytes. ^[102, 109] However, Mukherjee *et al.* did not get very ordered pores as observed from Al₂O₃. ^[109]

Subsequently, series of WO_3 films with self-assembled ordered nano-porous structures were obtained by anodizing in F^- containing electrolytes. [101, 110] Recently, Chin *et al.* synthesized WO_3 films with nanotube structures by anodization of tungsten in the solution including sodium sulfate and ammonium fluoride. [139] In view of a study by Tsuchiya *et al.*, [102] which is focused on the effects of NaF, the best quantity of NaF to obtain the most ordered pores should be lied within the range of 0.2 wt% ~ 0.5 wt%.

Otherwise, for modifying the morphology of the obtained WO_3 , some additives were also studied and it was found that the addition of organic solvents such as poly(ethylene glycol) or ethylene glycol showed detrimental effects on producing porous WO_3 film, as these caused aggregates which reduced the surface area of the film greatly. [107]

By contrasting with the acid solutions, basic electrolytes have also been investigated, however these were found to be undesirable. According to literatures, so far, the anodization of tungsten in sodium hydroxide solutions performed by Chen *et al.* induced porous structure with mixture of irregular trenches or separated nano-bubbles. [140]

II. Anodization potential

Besides the electrolyte composition, another significant anodization parameter

is the voltage. The voltage is the critical source resulting in localized breakdown during anodization process. Hence, in order to keep ordered porous morphology, appropriate potentials must be selected otherwise the mesh-like morphology will be produced owing to the severe breakdown. Aiming at elucidating such effect, Hahn *et al.* investigated voltage related structures of the oxides during the anodization in their early work, especially on TiO₂ and WO_x.^[116] They pointed out that at least 10V must be provided to generate localized breakdown in chloride containing solutions in the case of WO_{3.84} or TiO₂ and an optimum voltage lied within a range of 40~60V, during which the WO₃ film with uniform pores was obtained and the average pore size was 60~100nm, based on discussions by numerous groups.^[102, 105] Otherwise, thinner WO₃ film with either scattered nano-hole or non-porous structures were obtained. On the opposite aspect, if the voltage went beyond 60V, for example in within a range of 60~80V, the results showed an evolution of nano-pores to tepee-like nanowires due to the excessive electrical field intensity which leads to the collapse of the formed pores.^[141-142]

III. Anodization time

Tacconi *et al.* were the first to investigate the relationship between anodization time and the morphology of the films at selected voltages.^[142] They observed that when tungsten foil was anodized under 35 V for 30 min in 0.30 M oxalic acid solution only a low fraction of the film's surface exhibited a porous

structure. However, on extending the time to 300 min and increasing the voltage to 55 V the porous structure was lost being replaced by cracks throughout the entire film. Later a similar observation was also reported by Watcharenwong *et al.*, who pointed out that the best anodization time to obtain the most porous structure should be chosen within the range 1-3 hours. ^[104] In other words, a short period of anodization time, such as 30 min, was insufficient for forming nanostructures, while a long period, such as 4-6 h, lead to the collapse of the formed nanostructures. This has subsequently been confirmed by other authors, where an anodization period of 1 -3 h exhibited optimum porous film morphology. ^[105, 143]

Time is also a feasible tool to control the film thickness. Yang *et al.* ^[141] obtained WO₃ films with a thicknesses from 500 nm to 2.5 μm by extending the anodization time from 5 min to 40 min in 8M HF and concentrated phosphoric acid containing solutions. Besides, a film with thickness of 0.6 μm-8.7 μm was synthesized by Lee *et al.* by anodizing in the range of 6 h~26 h in 10Wt. % K₂HPO₄/glycerol electrolyte at 50°C. However, further extending the anodizing period failed to further increase the film thickness, since the establishment of steady state between oxidation and dissolution rates would inhibit any further increase of the film thickness. ^[144]

1.5 Investigations on electrochromism of metal/metal oxide doped WO₃ films

In the Section 1.4, it is explained that the properties of WO₃ films are related to the synthesis method used. Among all the aqueous-phase methods, hydrothermal method and anodization are more flexible, simple and low cost-effect ones in controlling and modelling the morphology of films. Therefore, the hydrothermal and anodization method will be applied for the fabrication of the desired films in this thesis. To improve the electrochromic properties, both choosing an appropriate film synthesis method and doping of transition metal oxide with WO₃ system are playing important roles. The application of doped oxide films on electrochromism have been discussed earlier by Granqvist^[52] and Monk.^[145]

The previous researches showed that the addition of small quantity of guest oxide into the electrochrome host can generate obvious effects on the material properties, such as conductivity, absorption spectrum and the potential capacity for electrochromic window application.^[146-149] Additionally, the oxide material showed the capability to solve the problems related to material reversibility, stability or optical modulation and so on, which are difficult to be overcome in pure metal oxide system^[146, 150-153]

By now, there are many reports on doping of metal or metal oxide with WO₃

system for improving its electrochromic properties. The metal or metal oxide included oxides of barium, ^[154] cobalt or nickel, ^[155-156] molybdenum, ^[157] tin ^[158] and titanium. ^[159-160] Moreover, the oxides of silver and copper have also been studied and incorporated into the WO₃ matrix respectively. ^[156] However, these last two oxides may not be beneficial for improving the electrochromism of WO₃, since metallic products, not oxides, will be formed during reduction process.

More recently, many efforts of employing Ti or TiO_x as dopant have been made to improve the electrochromic performance of tungsten oxide. However, there are few reports revealing the nature of the titanium incorporation. Some reports claimed that the TiO₂ doped WO₃ system does not form solid solution. ^[160-163] Most observations found that the incorporation of certain quantity of titanium can improve the electrochromic reversibility, because titanium creates disorder in the structure of the crystalline WO₃ that results in more convenient channels for charges transport.

Hashimoto and Matsuoka firstly reported that the amorphous TiO₂ doped WO₃ film, produced by electron beam deposition method, exhibits longer lifetime comparing with pristine tungsten oxide film. ^[164] Subsequently, Gottsche *et al.* compared the electrochromic properties of TiO₂ doped WO₃ films that fabricated by sputtering and sol-gel techniques. They pointed out that the

addition of TiO₂ with molar percentages from 10% to 15% reduces the crystallinity of WO₃ host and leads to significant structural changes.^[165] Later, Wang and Hu successfully composed TiO₂-doped WO₃ film by spin coating method and found that the Ti-addition can stabilize the peroxotungstic acid sol in the spin coating solutions and preserve amorphous structure in the main matrix, which in turn improves the electrochromic capacity of TiO₂-doped WO₃ film.^[147]

In 2005, Patil *et al.*^[166] investigated the effects of TiO₂ on the electrochromic property of WO₃ film, which was prepared through spray pyrolysis. They found that the increase of TiO₂ content improves electrochromic performance of WO₃ film with electrochromic reversibility and coloration efficiency, and the addition of TiO₂ is helpful in facilitating process of charge intercalation / de-intercalation due to more open channels observed in the morphology of TiO₂ doped WO₃ film.^[166] However, the coloration efficiency was not improved significantly in that study, and the other study showed that certain additions of TiO₂ are detrimental to the coloration efficiency. Presently, Cai *et al.*^[167] studied the effect of different concentrations of titanium on the electrochromic property of WO₃ films prepared by a hydrothermal method and found the optimum content of 3 mol%, leading to three times higher coloration efficiency than the pristine WO₃ film. This improvement was because of the reduced charge transfer and diffusion resistances that caused by the improved structure disorder

after adding TiO₂.

In review of the previous researches, it can be seen that doping of TiO₂ in WO₃ host is an effective way to change the film structure and in turn improve the electrochromic properties. However, there are no reports on producing TiO₂ doped WO₃ film by anodization of co-sputtered Ti/W films on conductive glass substrates until now. In this thesis, the objects are i). to investigate the influences of doping different percentages of TiO₂ into WO₃ matrix on the electrochromic property in comparison with the pristine WO₃ film, and the determine the optimized molar proportion between Ti and W; ii). to study the morphologies of TiO₂ doped WO₃ anodizing in aqueous and non-aqueous solutions respectively and investigate the influence of morphologies on the coloration efficiency and light transmittance; iii). to investigate the improvement of electrochromic properties of TiO₂ doped WO₃ thin film with nano-rod morphology fabricated by using hydrothermal method, which is first reported here.

1.6 Scope of this thesis

The scope of the whole thesis consists of seven chapters, except for chapter 1, which is the introduction, the remaining chapters are:

Chapter 2 describes the experimental methods and characterization techniques

used in present work.

Chapter 3 presents the findings from the hydrothermally prepared TiO₂ doped WO₃ thin films and its corresponding electrochromic properties.

Chapter 4 discusses the observations and electrochromic features of TiO₂ doped WO₃ thin films prepared by the electrochemical anodization of co-sputtered W/Ti in the organic electrolyte.

Chapter 5 elaborates influences of different amount of TiO₂ dopant on the electrochromic properties of pure WO₃ thin film. The TiO₂ doped WO₃ films are prepared by electrochemical anodization of co-sputtered Ti/W thin film with varied atomic percentages of titanium in aqueous electrolyte.

Chapter 6 makes general conclusions drawn from this work.

Chapter 7 points out works which are valuable to be investigated in future.

References:

- [1] Diesbach, cited in Gmelin, *Handbuch der Anorganischen Chemie*, **59** (1930) 671
- [2] J. J. Afhandlingar i fysik. Berzelius, *Kemi Och Mineralogie*, **4** (1815) 293
- [3] F. Wohler, *Ann. Phys.*, **2** (1824) 350
- [4] P. Marshall, photography.about.com/library/weekly/aa061801b.htm (accessed 26 January 2006).

- [5] A. Bain, *UK Patent*, 27 May 1843
- [6] F. H. Smith, *British Patent*, **328, 017** (1929).
- [7] N. Kobosew and N. I. Z. Nekrassow, *Electrochem.* **36** (1930) 529
- [8] P. Talmay, *US Patent 2*, **281, 013** (1942)
- [9] P. Talmay, *US Patent 2*, **319, 765** (1943)
- [10] E. O. Brimm, J. C. Brantley, J. H. Lorenz and M. H. Jellinek, *J. Am. Chem. Soc.*, **73** (1951) 5427
- [11] T. Kraus, Laboratory report: Balzers AG, Lichtenstein, entry date 30 July 1953
- [12] Philips Electronic and Associated Industries Ltd. Image display apparatus. *British Patent 1*, **302, 000** (1973)
- [13] C. J. Schoot, J. J. Ponjee, H. T. van Dam, R. A. van Doorn and P. T. Bolwijn, *Appl. Phys. Lett.* **23** (1973) 5
- [14] G. D. Short and L. Thomas, *British Patent 1*, **310, 813** (1973)
- [15] J. Blanc and D. L. Staebler, *Phys. Rev. B.*, **4** (1971) 57
- [16] L. C. Beegle, *US Patent 3*, **704, 057** (1972)
- [17] M. Green and D. Richman, *Thin Solid Films*, **24** (1974) 6
- [18] B. W. Faughnan, R. S. Crandall and P. M. Heyman, *RCA Rev.*, **36** (1975) 97
- [19] S. K. Mohapatra, *J. Electrochem. Soc.* **285** (1978) 8
- [20] K. K. Kananzawa, A. F. Diaz, R. H. Geiss, W. D. Gill, J. F. Kwak, J. A. Logan, J. F. Rabolt and G. B. Street, *J. Chem. Soc., Chem. Commun.*, (1979) 5
- [21] C. Santato, M. Ulmann, J. Augustynski, *J Phys Chem B*, **105** (2001) 936.
- [22] C.G.Granqvist, *Solid State Ionics*, **70/71** (1994) 678
- [23] R. J. Mortimer, A. L. Dyer, J. R. Reynolds, *Displays*, **27** (2006) 2.
- [24] T. Oi, *Ann. Rev. Mater. Sci.*, **16** (1986) 185
- [25] B. Klaus, G. Thomas, *Adv. Muter.*, **2** (1990) 1
- [26] C. G. Granqvist, *Renewable Energy*, **5, Part I** (1994) 141
- [27] B. W. Faughnan, R. S. Crandal, *Display Devices*, **181** (1980) 252
- [28] I. F. Chang, *Nonemissive Electrooptic Displays*, **155** (1976) 360
- [29] K. Yamanaka, *Jpn. J. Appl. Phys.*, **21** (1982) 926
- [30] C. Ho, D. Raistrick, R. A. Huggins, *J. Electrochem. Soc.*, **127** (1980) 343
- [31] B. W. Faughnan and R. S. Cranda1, *Appl. Phys. Lett.*, **31** (1977) 834

- [32] K. Yamanaka, *J. Appl. Phys.*, **54** (1983) 1128
- [33] H. R. Zeller, H. U. Beyeler, *Appl. Phys.*, **13** (1977) 231
- [34] H. Okamoto, K. Yamanaka, T. Kudo, *Mater. Res. Bull.*, **21** (1986) 551
- [35] X. X. Cao, X. B. Zhang, J. X. Hu, *J. Nanosci. Nanotechnol.*, **14** (8) (2014) 6368
- [36] G. A. de Wijs and R. A. de Groot, *Phys. Rev. B*, **60** (24) (1999) 16463
- [37] Y. S. Shim, L. H. Zhang, D. H. Kim, *Sensor Acuat B-Chem.*, **198** (2014) 294
- [38] W. Wang, Y. Pang, S. N. B. Hodgson, *J. Sol Gel Sci. Technol.*, **54** (2010) 19.
- [39] S. R. Bathe, P. S. Patil, *Smart Mater. Struct.*, **18** (2009) 025004
- [40] Y. P. Xie, G. Liu, G. Q. Lu and H. M. Cheng, *Nanoscale*, **4** (2012) 1267;
- [41] E. Washizu and A. Yamamoto, *Solid State Ionics*, **165**(1-4) (2003) 175.;
- [42] T. Vogt, P. M. Woodward and B. A. Hunter, *J. Solid State Chem.* **144** (1999) 209.
- [43] M. Shiojiri, T. Miyano, C. Kaito, *Japan. J. Appl. Phys.*, **17** (1987) 567
- [44] C. Kaito, T. Shimizu, Y. Nakata, Y. Saito, *Japan. J. Appl. Phys.*, **24** (1985) 117
- [45] G. M. Ramans, J. V. Gabrusenoks, A. A. Veispals, *Phys. Status Solidi*, **74** (1982) K41
- [46] J. V. Gabrusenoks, P. D. Cikmach, A. R. Lasis, J. J. Kleperis, G. M. Ramans, *Solid State Ionics*, **14** (1984) 25
- [47] G. M. Ramans, I. V. Gabrusenoks, A. R. Lasis, A. A. Patmalnieks, *J. Non-Cryst. Solids*, **90** (1987) 637.
- [48] T. C. Arnoldussen, *J. Electrochem. Soc.*, **I** (1981) 117
- [49] T. Nanba, I. Yasui, *J. Solid State Chem.*, **83** (1989) 304
- [50] E. Ozkan, S-H. Lee, C. E. Tracy, J. R. Pitts, S. K. Deb, *Sol Energ Mat. Sol C.*, **79** (2003) 439
- [51] A. Baserga, V. Russo, F. Di Fonzo, A. Bailini, D. Cattaneo, C. S. Casari, A. Li Bassi, C. E. Bottani, *Thin Solid Films*, **515** (2007) 6465.
- [52] C.G. Granqvist, *Handbook of Inorganic Electrochromic Materials*, New York, (1995)
- [53] C. V. Ramana, S Utsunomiya, R. C. Ewing, C. M. Julien, U. Becker, *Phys Status Solidi A*, **202** (2005) R108.
- [54] A. Z. Sadek, H. Zheng, M. Breedon, V. Bansal, S. K. Bhargava, K. Latham, J. Zhu, L. Yu, Z. Hu, P. G. Spizzirri, W. Wlodarski, K. Kalantar-

- Zadeh, *Langmuir*, **25** (2009) 9545.
- [55] P. Judeinstein, R. Morineau, J. Livage, *Solid State Ionics*, **51** (1992) 239
- [56] A. Al Mohammad and M. Gillet, *Thin Solid Films*, **408** (2002) 302
- [57] J. S. E. M. Svensson and C. G. Granqvist, *Appl. Phys. Lett.*, **45** (1984) 828
- [58] S. F. Cogan, T.D. Plante, M.A. Parker, R.D. Rauh, *J. Appl.Phys.*, **60** (1986) 2735.
- [59] F.O. Arntz, R.B. Goldner, B. Morel, T.E. Haas, K.K. Wong, *J.Appl. Phys.*, **67** (1990) 3177.
- [60] L. L. Hench, J.K. West, *Chem. Rev.*, **90** (1990) 35
- [61] O. Lev, *Analytical Chemistry.*, **67(1)** (1995) 22A
- [62] E. Bica, L. E. Mureşan, L. Barbu-Tudoran, E. Indrea, I. C. Popescu, E. Popovici, *Dig. J. Nanomater. Bios.*, **6** (2011) 1935
- [63] W. Wang, Y. Pang, S. N. B. Hodgson, *J. Sol Gel Sci. Technol.*, **58** (2011) 135.
- [64] M. Deepa, T. K. Saxena, D. P. Singh, K. N. Sood, S. A. Agnihotry, *Electrochim. Acta*, **51** (2006) 1974.
- [65] M. Deepa, P. Singh, S. N. Sharma, S. A. Agnihotry, *Sol Energ Mat. Sol C.*, **90** (2006) 2665.
- [66] Y. Fang, X. Sun, H. Cao, *J. Sol Gel Sci. Technol.*, **59** (2011) 145.
- [67] A. K. Srivastava, S. A. Agnihotry, M. Deepa, *Thin Solid Films*, **515** (2006) 1419.
- [68] X. Sun, H. Cao, Z. Liu, J. Li, *Appl. Surf. Sci.*, **255** (2009) 8629.
- [69] M. Breedon, P. Spizzirri, M. Taylor, J. D. Plessis, D. McCulloch, J. Zhu, L. Yu, Z. Hu, C. Rix, W. Wlodarski, K. Kalantar-Zadeh, *Cryst. Growth Des.*, **10** (2010) 430
- [70] J. Livage, D. Ganguli, *Sol Energ Mat. Sol C.*, **68** (2001) 365.
- [71] B. Yang, Y. Zhang, E. Drabarek, P. R. F. Barnes, V. Luca, *Chem. Mater.*, **19** (2007) 5664.
- [72] D. J. Ham, A. Phuruangrat, S. Thongtem, J. S. Lee, *Chem. Eng. J.*, **165** (2010) 365.
- [73] S. Rajagopal, D. Nataraj, D. Mangalaraj, Y. Djaoued, J. Robichaud, O. Y. Khyzhun, *Nanoscale Res. Lett.*, **4** (2009) 1335.
- [74] J. M. Wang, E. Khoo, P. S. Lee, J. Ma, *J. Phys. Chem. C.*, **112** (2008) 14306.
- [75] J. M. Wang, E. Khoo, P. S. Lee, J. Ma, *J. Phys. Chem. C.*, **113** (2009) 9655.

- [76] Z. J. Gu, T. Y. Zhai, B. F. Gao, X. H. Sheng, Y. B. Wang, H. B. Fu, Y. Ma, J. N. Yao, *J. Phys. Chem. B.*, **110** (2006) 23829.
- [77] A. Phuruangrat, D. J. Ham, S. J. Hong, S. Thongtem, J. S. Lee, *J. Mater. Chem.*, **20** (2010) 1683.
- [78] Z. J. Gu, Y. Ma, W. S. Yang, G. J. Zhang, J. N. Yao, *Chem. Commun.*, (2005) 3597.
- [79] J. Su, X. Feng, J. D. Sloppy, L. Guo, C. A. Grimes, *Nano Lett.*, **11** (2011) 203
- [80] J. Zhang, J. Tu, X. Xia, X. Wang, C. Gu, *J. Mater. Chem.*, **21** (2011) 5492.
- [81] Y. Xu, L. Huo, X. Cheng, H. Zhao, S. Gao, *Chi. J. Inorg. Chem.*, **23** (2007) 867.
- [82] G. Zou, H. Li, Y. Zhang, K. Xiong, Y. Qian, *Nanotechnology*, **17** (2006) S313.
- [83] Y. Zhang, Y. Chen, H. Liu, Y. Zhou, R. Li, M. Cai, X. Sun, *J. Phys. Chem. C.*, **113** (2009) 1750
- [84] J. Ha, P. Muralidharan, D. K. Kim, *J. Alloys Compounds*, **475** (2009) 446.
- [85] X. Song, Y. Zhao, Y. Zheng, *Mater Lett.*, **60** (2006) 3405.
- [86] X. Su, F. Xiao, Y. Li, J. Jian, Q. Sun, J. Wang, *Mater. Lett.*, **64** (2010) 1232.
- [87] Z. Zhao, M. Miyauchi, *J. Phys. Chem. C.*, **113** (2009) 6539.
- [88] P. K. Shen and A. C. C. Tseung, *J. Mater. Chem.*, **2** (1992) 1141.
- [89] S. H. Baeck, K. S. Choi, T. F. Jaramillo, G. D. Stucky and E. W. McFarland, *Adv. Mater.*, **15** (2003) 1269
- [90] S. Wang, X. Feng, J. Yao and L. Jiang, *Angew. Chem. Int. Ed.*, **45** (2006) 1264.
- [91] Y. C. Ha, D. Y. Jeong, *J. Korean Phys. Soc.*, **57** (2010) 1661
- [92] G. K. Mor, O. K. Varghese, M. Paulose, K. Shankar, C. A. Grimes, *Sol Energ Mat. Sol. C.*, **90** (2006) 2011.
- [93] L. T. Canham, *Appl. Phys. Lett.*, **57** (1990) 1046.
- [94] H. Masuda, K. Fukuda, *Science*, **268** (1995) 1466.
- [95] A. Ghicov, P. Schmuki, *Chem. Comm.*, **20** (2009) 2791.
- [96] I. Sieber, B. Kannan, P. Schmuki, *Electrochem. Solid-State Lett.*, **8** (2005) J10.
- [97] L. V. Sieber, P. Schmuki, *J. Electrochem. Soc.*, **152** (2005) C639.
- [98] H. Tsuchiya, P. Schmuki, *Electrochem. Commun.*, **6** (2004) 1131.

- [99] M. Yang, N. K. Shrestha, P. Schmuki, *Electrochim. Acta*, **55** (2010) 7766.
- [100] M. Yang, N. K. Shrestha, R. Hahn, P. Schmuki, *Electrochem. Solid-State Lett.*, **13** (2010) C5.
- [101] Y. Nah, A. Ghicov, D. Kim, P. Schmuki, *Electrochem. Commun.*, **10** (2008) 1777.
- [102] H. Tsuchiya, J. M. Macak, I. Sieber, L. Taveira, A. Ghicov, K. Sirotna, P. Schmuki, *Electrochem. Commun.*, **7** (2005) 295
- [103] S. Berger, H. Tsuchiya, *Appl. Phys. Lett.*, **88** (2006) 203119.
- [104] A. Watcharenwong, W. Chanmanee, N. R. d. Tacconi, C. R. Chenthamarakshan, P. Kajitvichyanukul, K. Rajeshwar, *J. Electroanal. Chem.*, **612** (2008) 112.
- [105] H. Zheng, A. Z. Sadek, K. Latham, K. Kalantar-Zadeh, *Electrochem. Commun.*, **11** (2009) 768
- [106] T. Oishi, T. Matsubara, A. Katagiri, *Electrochemistry* (in. Japanese), **68** (2000) 106.
- [107] Y. Guo, X. Quan, N. Lu, H. Zhao, S. Chen, *Environ. Sci. Technol.*, **41** (2007) 4422.
- [108] J. Z. Ou, S. Balendhran, M.R. Field, D.G. McCulloch, A.S. Zoofakar, R.A. Rani, S. Zhuiykov, A.P. O'Mullane, K. Kalantar-Zadeh, *Nanoscale.*, **4** (2012) 5980
- [109] N. Mukherjee, M. Paulose, O. K. Varghese, G. K. Mor, C. A. Grimes, *J. Mater. Res.*, **18** (2003) 2296.
- [110] H.D. Zheng, Abu Z. Sadek, K. Latham, K. Kalantar-Zadeh, *Electrochem. Commun.*, **11** (2009) 768
- [111] J. Zhang, X.L. Wang, X.H. Xia, C.D. Gu, Z.J. Zhao, J.P. Tu, *Electrochim. Acta*, **55** (2010) 6953
- [112] V. Cristino, S. Caramori, R. Argazzi, L. Meda, G. L. Marra, C. Bignozzi, *Langmuir*, **27** (2011) 7276.
- [113] O.Jessensky, F. Muller, U. Gosele, *Appl. Phys. Lett.*, **72** (1998) 1173
- [114] M. Pourbaix, *Atlas of Electrochemical Equilibria in Aqueous Solutions*, Houston, Texas, (1966)
- [115] M. L. Wang, Y. N. Liu, H. Yang, *Electrochim. Acta*, **62** (2012) 424
- [116] R. Hahn, J. M. Macak, P. Schmuki, *Electrochem. Commun.*, **9** (2007) 947.
- [117] A. DiPaola, F. DiQuarto, G. Serravalle, *J. Less-Common Met.*, **42** (1975) 315
- [118] M.R. Arora, R. Kelly, *J. Electrochem. Soc.*, **124** (1977) 1493.
- [119] A. DiPaola, F. DiQuarto, *Electrochim. Acta*, **22** (1977) 63.

- [120] B. Reichman, A.J. Bard, *J. Electrochem. Soc.*, **126** (1979) 583.
- [121] F. DiQuarto, A. DiPaola, C. Sunseri, *J. Electrochem. Soc.*, **127** (1980) 1016.
- [122] F. DiQuarto, A. DiPaola, C. Sunseri, *Electrochim. Acta*, **26** (1981) 1177.
- [123] F. DiQuarto, G. Russo, C. Sunseri, A. DiPaola, *J. Chem. Soc. Faraday Trans.*, **78** (1) (1982) 3433.
- [124] A. Goossens, D.D. Macdonald, *Electrochim. Acta*, **38** (1993) 1965.
- [125] A. Goossens, D.D. Macdonald, *J. Electroanal. Chem.*, **352** (1993) 68.
- [126] S.R. Biaggio, R.C. Rocha Filho, J.R. Vilche, F.E. Varela, L.M. Gassa, *J. Braz. Chem.Soc.*, **5** (1994) 123.
- [127] E. Sikora, J. Sikora, D.D. Macdonald, *Electrochim. Acta*, **41** (1996) 783.
- [128] M. Bojinov, *Electrochim. Acta*, **42** (1997) 3489.
- [129] M. Bojinov, S. Cattarin, M. Musiani, B. Tribollet, *Electrochim. Acta*, **48** (2003).
- [130] K. Shimizu, G.M. Brown, H. Habazaki, K. Kobayashi, P. Skeldon, G.E. Thompson, G.C. Wood, *Corros. Sci.*, **40** (1998) 1238.
- [131] D.D. Macdonald, E. Sikora, J. Sikora, *Electrochim. Acta*, **43** (1998) 2851.
- [132] J. Sikora, E. Sikora, D.D. Macdonald, *Electrochim. Acta*, **45** (2000) 1875.
- [133] M. Anik, K. Osseo-Asare, *J. Electrochem. Soc.*, **149** (2002) B224.
- [134] M. Anik, *Turk. J. Chem.*, **26** (2002) 915.
- [135] M. Metikos-Hukovic, Z. Grubac, *J. Electroanal. Chem.*, **556** (2003) 167.
- [136] M.-G. Vergé C. -O.A. Olsson, D. Landolt, *Corros. Sci.*, **46** (2004) 2583.
- [137] C.O.A. Olsson, M.-G. Vergé D. Landolt, *J. Electrochem. Soc.*, **151** (2004) B652.
- [138] M. Anik, *Corros. Sci.*, **48** (2006) 4158.
- [139] W. L. Chin, S. B. A. Hamid, and S. Sreekantan, *Int. J. Photoenergy*, (2013)
- [140] W. Chen, M. Lai, K. Tsai, C. Liu, Y. Wang, *J. Phys. Chem. C.*, **115** (2011) 18406.
- [141] M. Yang, N. K. Shrestha, P. Schmuki, *Electrochem. Commun.*, **11** (2009) 1908.
- [142] N. R. De Tacconi, C. R. Chenthamarakshan, G. Yogeewaran, A. Watcharenwong, R. S. De Zoysa, N. A. Basit, K. Rajeshwar, *J. Phys. Chem. B*, **110** (2006) 25347.
- [143] A. Kuzmin, J. Purans, *J. Phys., Condens. Matter*, **5** (1993) 2333
- [144] W. Lee, D. Kim, K. Lee, P. Roy, P. Schmuki, *Electrochim. Acta*, **56** (2010)

- [145] P. M. S. Monk, R. J. Mortimer, D. R. Rosseinsky, in *Electrochromism: Fundamentals and Applications*, New York, (1995) 59
- [146] Z. Esra Ozkan, *Sol Energ Mat. Sol C.*, **87** (2005) 695
- [147] Z. C. Wang, X. F. Hu, *Electrochim. Acta.*, **46** (2001) 1951
- [148] R. B. Suvarna and P.S. Patil, *Solid State Ionics.*, **179** (2008) 314
- [149] K. Paipitak, C. Kahattha, W. Techitdheera, S. Porntheeraphat, W. Pecharapa, *Energy Procedia*, **9** (2011) 446
- [150] N. R. de Tacconi, C. R. Chenthamarakshan, K. L. Wouters, F. M. MacDonnell, K. Rajeshwar, *J. Electroanal. Chem.*, **566(2)** (2004) 249
- [151] H. M. Yang, R. R. Shi, K. Zhang, Y. H. Hua, A.D. Tang, X.W. Li, *Appl. Surf. Sci.*, **250** (2005) 117
- [152] A. Karupphasamy, A. Subrahmanyam, *Thin Solid Films*, **516** (2007) 175
- [153] N. N. Dinh, D. H. Ninh, T. T. Thao, T. Vo-Van, *J. Nanomater.*, (2012)
- [154] B. J. Molnar, A.R. Haranahalli, B. D. Dove, *J. Vac. Sci. Technol.*, **15** (1978) 161
- [155] P. K. Shen, J. Syed-Bokhari, A. C .C. Tseung, *J. Electrochem. Soc.*, **138** (1991) 2778.
- [156] P. M. S. Monk ,S. L. Chester, *Electrochim. Acta*, **38** (1993) 1521.
- [157] L. H. Dao, A. Guerfi, M. T. Nguyen. *Proc. Electrochem. Soc.*, **90-2** (1990) 30.
- [158] P. V. Ashrit, G. Bader, F. E. Giround and V. V. Truong, *Proc. Electrochem.Soc.*, **90-2** (1990) 45.
- [159] H. Matsuoka, S. Hashimoto, H. Kagechika, H. Gijutsu, *J. Surface Finish. Soc. Jpn*, **42** (1991) 246
- [160] S. Hashimoto, H. Kagechika, *J. Electrochem. Soc.*, **138** (1991) 2403.
- [161] Chang, Y. L. L.; Seoger, M. G.; Philips, B. S. *Less Common Maters* 1967, 12, 53.
- [162] Miyauchi, M.; Nakajima, A.; Hashimoto, K.; Watanabe, T. *Adv. Mater.* 2000, 12, 1923.
- [163] Kwon, Y. T.; Song, K. Y.; Lee, W. I.; Choi, G. J.; Do, Y. R. *J. Catal.* 2000, 191, 192.
- [164] S. Hashimoto, H. Matsuoka, *J. Electrochem. Soc.* **138** (1991) 2403.
- [165] J. Gottsche, A. Hinsch, V. Wittwer, *Sol Energ Mat. Sol C.*, **31** (1993) 415
- [166] P.S. Patil, S.H. Mujawar, A.I. Inamdar, P.S. Shinde, H.P. Deshmukh, S.B. Sadale, *Appl. Surf. Sci.*, **252** (2005) 1643

[167] G.F. Cai, X.L. Wang, D. Zhou, J.H. Zhang, Q.Q. Xiong, C.D. Guab, J.P. Tu, *RSC Adv.*, **3** (2013) 6896

Chapter 2 Experiments Details

2.1 Preparation of Samples Used for Hydrothermal Method

2.1.1 Substrates cleaning

Fluorine coated tin oxide (FTO) glass substrates of sheet resistance $15 \Omega \cdot \text{sq}^{-1}$ were cut to 24 mm \times 50 mm rectangles and cleaned by sequential ultrasonication in 5% Deconex@90, Milli-Q water (resistivity $\sim 10 \text{ M}\Omega \cdot \text{cm}$), isopropanol, acetone and absolute ethanol, each for 15 minutes. The cleaned FTO glasses were kept in isopropanol solutions to avoid contaminations and ready for use.

2.1.2 Seed layer fabrication

A TiO_2 blocking layer was deposited onto the clean FTO substrate by immersing it in 0.1 M TiCl_4 solution and keeping on a hot plate at 50°C for 1 hour, followed by rinsing with Milli-Q water (resistivity $\sim 10 \text{ M}\Omega \cdot \text{cm}$) and ethanol, after that, the coated FTO substrate was heating at 120°C for 15 min to evaporate any residual water or organic solvent.

A WO_3 seed layer was deposited on to the TiCl_4 processed FTO substrate using a WO_3 precursor solution prepared following a standard procedure.^[1] 1g $\text{Na}_2\text{WO}_4 \cdot 2\text{H}_2\text{O}$ was dissolved in 15ml de-ionized water, and then concentrated HCl solution was added until no more precipitate formed. The precipitate was

washed using de-ionized water at least 5 times in a 1 L beaker placed in an ice bath. Then 2 ml H₂O₂ was added into the precipitate under intense stirring at 50°C to dissolve the precipitate and obtain transparent sol solutions. The excess H₂O₂ in the sol solution was consumed by placing a platinum wire into the solution until the bubbling ceased. The thin seed layer was obtained by casting the prepared sol solution onto TiCl₄ processed FTO substrate via spin-coating at 3000 rpm for 15 s and annealing at 400°C for 30 min.

2.1.3 Hydrothermal deposition

For the hydrothermal deposition, the WO₃ precursor solution consisted of 0.12 M Na₂WO₄ was agitated in an ultrasonic bath and the pH was adjusted to 2.0 with 3 M HCl and 0.26 M (NH₄)₂SO₄ powder. The TiO₂ precursor solution was prepared following the method described by Liao and Wu. In brief, 0.05M Ti(IV) tert-butoxide was dissolved in 6 M HCl, and stirred for 1 hour to obtain TiO₂ precursor solution.^[2]

Once both precursor solutions were prepared, 10 mL of the WO₃ precursor solution and 20 mL of the TiO₂ precursor solution were transferred into a 50 ml polytetrafluoroethylene-lined stainless steel autoclave tub, which gave a nominal molar WO₃ to TiO₂ ratio of 1.2:1. The prepared FTO glass substrate was then placed vertically in the autoclave. The autoclave was sealed and heated at a rate of 1°C min⁻¹ to 180°C and held for 2 hours, after that it left to cool

naturally. The processed WO₃ thin film was rinsed with Milli-Q water and dried at 120°C for 4 hours.

For a comparison, a pure WO₃ film was prepared by the same hydrothermal process except for 20 mL of 0.12M Na₂WO₄, instead of TiO₂ precursor solution, was added to the autoclave. Replicate electrochromic films were made for comparison in this study, the minimum numbers of each type of electrochromic film was three.

2.2 Preparation of Samples Used for Anodic Anodization

2.2.1 Film deposition by magnetron sputtering

Before sputtering, the substrate was cleaned followed the procedures described in section 2.1.1. The clean substrate, with small part (20% of the whole length) covered by aluminum foil for the purpose of exposing conductive surface for electrical connecting with wires, was placed into the chamber of a DC Magnetron Sputter. The targets, bought from AJA International, Inc., were 99.99% W and 99.99% Ti. The distance between each target and the substrate was 8 cm. Before deposition, the sputtering chamber was evacuated to 6.0×10^{-7} Torr after 12 hours at room temperature, after that the sputtering of W and Ti was conducted simultaneously in an inert argon atmosphere (2.0×10^{-6} Torr) on a substrate temperature of 400°C. During sputtering, the flow rate of argon was kept at 27×10^{-3} mmHg/min.

The atomic ratios of titanium over tungsten in W/Ti films were obtained by adjusting the RF power to the titanium target at 10 watt, 15 watt and 20 watt respectively, while keeping the RF power to the tungsten target at 90 watt. During the sputtering process, not all the atoms could be collected by the substrate, hence there was a loss of atoms. The initial atomic ratio was estimated from the sputtering power. Each target (pure tungsten or pure titanium) had its own sputtering rate corresponding to the selected sputtering power. The titanium sputtering rate was 10 nm/min at RF power of 100 W and the tungsten sputtering rate was 6 nm/min at RF power of 90 W. The final atomic ratio was obtained by SEM-EDS result. The temperature kept constant (400 ± 3 °C) during the sputtering process. The thickness of the film was controlled at around 450 nm by optimized sputtering duration.

2.2.2 Anodization of W/Ti thin films in organic solution

After magnetron sputtering deposition, the Ti/W thin film was anodized under a sweep rate of 0.1 V s^{-1} to 10 V and then fixed at 10 V for 40 min (Keithley 236 Source Measuring Unit) against a platinum cathode in 0.3M NH_4F dissolved in ethylene glycol (98% anhydrous, Sigma Aldrich) and 2 vol% deionized water. After anodization, the samples were carefully washed with Milli-Q water (resistivity $\sim 10 \text{ M}\Omega\cdot\text{cm}$) and dried under a stream of nitrogen gas, after that the samples were baked at 450°C for 3 hours to ensure complete

oxidation. The rising rate of the temperature was $2^{\circ}\text{C min}^{-1}$. The pure tungsten thin film was anodized under the same conditions.

2.2.3 Anodization of W/Ti thin films in aqueous solution

Ti/W thin film was anodized under a sweep rate of 1 V s^{-1} to 40 V and fixed at 40 V for 40 min (Keithley 236 Source Measuring Unit) against a platinum cathode in 1 M H_2SO_4 solution with 0.3 wt.% NaF. The heat treatment condition after anodization was the same as described in section 2.2.2.

2.3 Characterization

2.3.1 Morphology, Elemental Distribution and Structure Characterization

The morphologies and elemental distributions of the prepared films were investigated by using a Zeiss Field Emission Scanning Electron Microscopes (FESEM) and a high resolution JEM3010 F transmission electron microscope (HRTEM) equipped with a field emission gun. Sample preparation for the TEM investigations involved scrapping the desired thin film from the FTO substrate, dispersing the nanoparticles in absolute ethanol by ultrasonication, and then coating it onto copper grids. The crystal structure of thin film was probed using a Bragg-Brentato theta two theta diffractometer (Bruker D8 Advance) scanning from 20° to 80° with Cu K- α X-ray source (1.54\AA).

The oxidation state and surface composition of the as-prepared sample was

confirmed by high-resolution X-ray photoelectron spectroscopy with a Kratos Axis Ultra^{DLD} X-ray photoelectron spectrometer equipped with an Al K_α X-ray source (1486.6 eV), with the high resolution HRXPS spectra being analyzed with the aid of Casa-XPS software. The elemental carbon, which exists in ambient environment at constant concentration, was used as an internal standard for calibrating binding energies. Except for this, there were no other discernable impurities in samples.

Raman measurement was performed by Renishaw Raman microscope with an Ar ion laser at 532 nm excitation wavelength. Stretching and bending vibrations of WO₃ were occurred within the ranges 950 cm⁻¹-600 cm⁻¹ and 400 cm⁻¹-200 cm⁻¹, respectively. There were also sub-classifications reported for the short terminal W=O bonds which are not the stable phase and the bridging W-O-W bonds beyond 950 cm⁻¹ (You should rewrite this sentence).

2.3.2 Electrochemistry Characterization

The electrochemical properties of film were investigated by applying thin film as electrode in a conventional three electrode cell containing 1 M LiClO₄ (anhydrous) dissolved in propylene carbonate. The non-aqueous reference electrode was a Ag/Ag⁺ system constructed by immersing a silver wire in 0.01M AgNO₃ plus 0.1M tetrabutylammonium perchlorate dissolved in

acetonitrile. All potentials in this study were this reference system (0.30 V vs SHE). A Pt wire behaves as counter electrode to complete the circuit. Cyclic voltammetry (CV), electrochemical impedance spectroscopy (EIS) and chronoamperometry (CA) measurements were conducted at room temperature and controlled by an Autolab PGSTAT302N potentiostat with Gpes software.

The CV tests were carried out at a scan rate of 50 mV s^{-1} from -1.0 V to $+1.0 \text{ V}$ for hydrothermal produced films and from -2.0 V to $+1.0 \text{ V}$ for films fabricated by anodization method. EIS tests were carried out with a superimposed 5 mV sinusoidal (RMS) perturbation over the frequency range from 100 kHz to 0.01 Hz and analyzed by fitting to an equivalent circuit with the aid of Z-View software (Scribner Associates Inc.). The fit errors were calculated as in the following example: if the best value for a particular resistor is 200Ω , the value is increased from an estimated one until the goodness of fit starts to decrease; if 196Ω and 104Ω produce a very similar goodness of fit, but 195Ω and 105Ω produces a poorer fit, the error is reported as 4Ω and the percentage fitting error is 2%, which is calculated by $(200 \Omega - 196 \Omega) / 200 \Omega$. CA was measured by stepping the potential repeatedly between -2.0 V and 2.0 V holding for 60 s and 100 s at the negative and positive limits respectively for hydrothermal produced films. CA tests on films prepared by anodization method were measured by stepping the potential repeatedly between -1.0 V and 1.0 V holding for 50 s and 150 s at the negative and positive limits, respectively.

2.3.3 Characterization of Electrochromic Feature

The electrochromic properties of the target films were recorded by conducting *in situ* electrochemical experiments in a quartz cuvette using a Shimadzu UV-Vis 1800 spectrometer. The changes in the transmittance of the films were followed simultaneously with their respective CA tests. The reference side of the UV-Vis spectrometer contained a quartz cuvette filled with 1 M LiClO₄ dissolved in propylene carbonate. All solvents and chemicals were of analytical grade and used without further purification.

References

- [1] Z. H. Jiao, X. W. Sun, J. M. Wang, L. Ke, H. V. Demir, *J. Phys. D: Appl. Phys.*, **43** (2010) 285501
- [2] W. P. Liao, J. J. Wu, *J. Mater. Chem.*, **21** (2011) 9255.

Chapter 3 A self-assembled two-layer structured TiO₂ doped WO₃ film with improved electrochromic capacities

In this chapter, a self-assembled two-layer structured TiO₂ doped WO₃ film with improved electrochromic capacities will be introduced.

3.1 Introduction

The electrochromism of WO₃ involves color switch between transparent and an intense blue state, believed to be caused by W⁵⁺ color centers, ^[1] and its absorption in the red and near infrared region has resulted in it becoming the preferred material for “smart window” applications. ^[2] Granqvist estimates that the energy savings from using smart windows for cooling would be equivalent to that which could be generated by replacing the windows with thin film solar cells (assumed 17% efficiency for the solar cells) with the obvious advantage that the windows maintain their primary function of providing unmitigated visual contact. ^[3] This will be especially true in tropical climates where heating of office buildings and factories is largely by the transmission of infrared light through windows, causing 40% of their electrical demand to be used on air-conditioning. ^[4-5] Indeed, it is recently forecast that by 2020 the market for dynamic window technologies will be worth US\$418 million and could grow to more than \$1.4 billion if cost come down quickly. ^[6] Many methods have been used to fabricate WO₃ films on transparent conducting as described in section

1.

In this section, the hydrothermal method has been adopted to fabricate electrochromic films. According to literatures reported on hydrothermally produced pure WO_3 thin films recently, they show relatively lower light modulation range of 40% to 60% at 632.8 nm. ^[7-9] Therefore, in order to obtain films with large transmittance change, morphology of films with spacious channels for intercalation of more charges is the aim of this thesis and the doping of TiO_2 into WO_3 films is an applicable consideration with expectation of changing morphology by TiO_2 incorporations. In this chapter, the synthesis of TiO_2 doped WO_3 films via a simple one step hydrothermal technique is presented, along with pure WO_3 films. All the detailed preparation procedure and characterization methods have been elaborated in chapter 2.

3.2 Result and discussion

3.2.1 Morphology and composition analysis

Figure 3.1 shows surface and cross-sectioned SEM images of WO_3 films with and without TiO_2 dopants. It can be seen that the pure WO_3 films are composed of nano-wire structures, in agreement with the observations of Zhang *et al.* ^[10] However, the TiO_2 doped WO_3 film is composed of two parts, with polygonal nano-pillars of varying lengths (200 to 500 nm) on top of an approximately 250

nm thick compact layer of nano-particles (Figure 3.1c). This contrasts with the work of Liao and Wu who used similar conditions, but without the WO_3 precursor solutions, and observed only TiO_2 nano-rods. ^[11] The appearance of the compact layer is likely due to higher acidity used in the WO_3/TiO_2 reaction vessel ($pH < -0.5$) compared to that of its pure WO_3 counterpart ($pH 2$) accelerating the hydrothermal reactions:

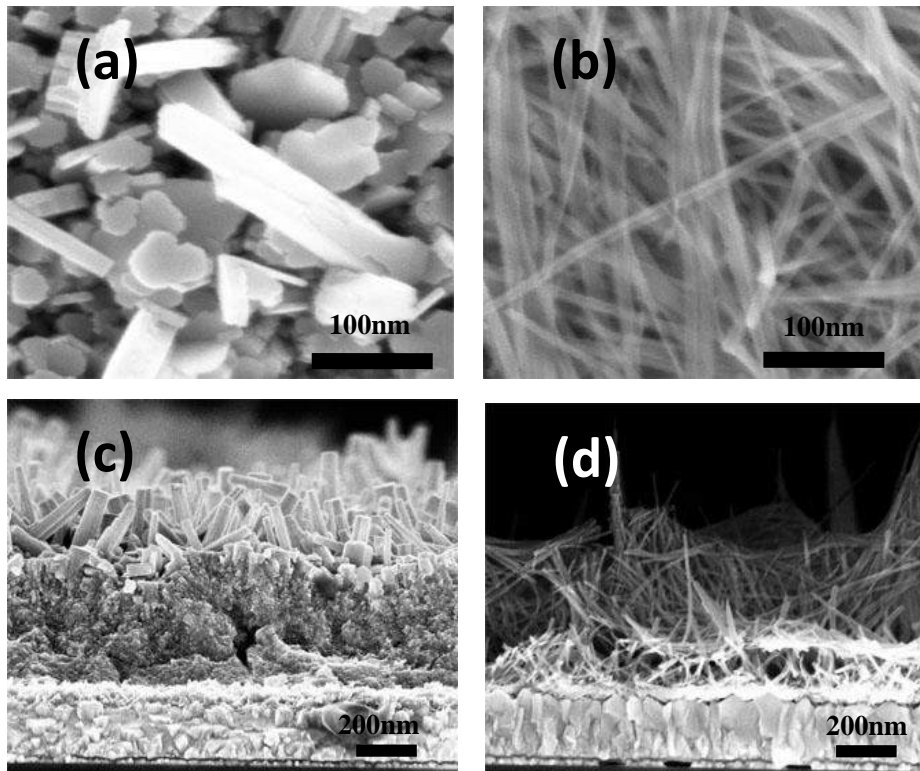
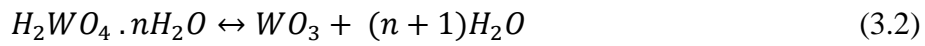
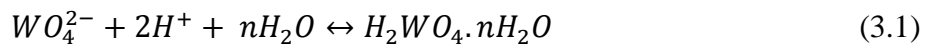


Figure 3.1 SEM images of a plan view of (a) TiO_2 doped WO_3 film, (b) pure WO_3 film, a cross-sectional view of (c) TiO_2 doped WO_3 film and (d) pure WO_3 film.

Nevertheless, EDS analysis, as shown in Figure 3.2, reveals that the atomic

W/Ti ratios in the nano-pillars and the compact layer are identical at approximate 3.8:1 calculated from Table 3.1, about three times the value of 1.2:1 expected from the concentrations of the initial reactants indicating that the WO₃ deposition is more efficient than its TiO₂ counterpart. This is consistent with the more complicated reaction mechanism required to deposit the TiO₂ (Reactions 3.3 to 3.8).^[12] The weights of the uncharged films (including seed layers) per unit area of FTO substrates are determined to be 6.4 x10⁻⁴ and 5.4 x10⁻⁴ g cm⁻² for the TiO₂ doped and pure WO₃ films respectively.

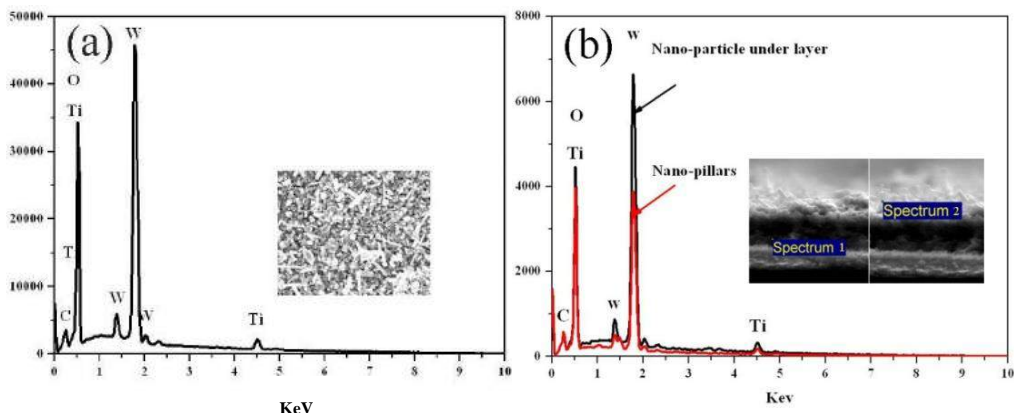
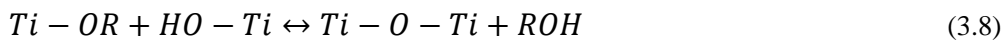
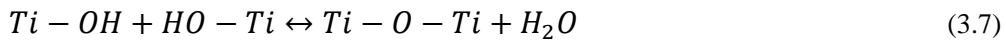
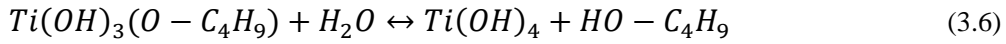
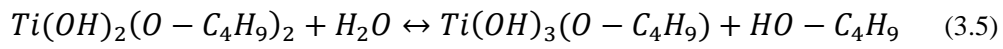
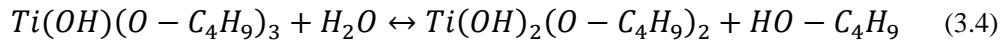
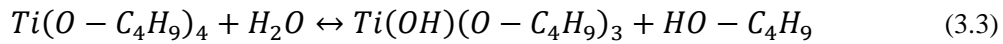


Figure 3.2 SEM-EDS spectrum of TiO₂ doped WO₃ film. (a) Mapping result of a top view and (b) Point distribution of a cross-sectional view of underlayer and nano-pillar respectively. The inset image is the corresponding SEM image.

Table 3.1 Element distribution list corresponding to the SEM-EDS results

| Element | Weight percentage % | | | Atomic percentage % | | |
|---------|---------------------|------------|-------------|---------------------|------------|-------------|
| | Top mapping | underlayer | Nano-pillar | Top mapping | underlayer | Nano-pillar |
| W | 65.4±5.0 | 67.0±5.8 | 58.8±3.6 | 15.0±4.6 | 16.0±2.9 | 11.4±1.6 |
| Ti | 4.4±0.5 | 4.6±0.3 | 4.1±0.2 | 3.9±1.4 | 4.2±0.7 | 3.0±0.4 |
| O | 28.3±5.0 | 26.4±3.1 | 33.0±0.4 | 74.4±4.8 | 72.5±4.2 | 73.4±7.4 |

The error (%) is the standard deviation.

In order to investigate the evolution of the growth of nano-pillars and the compact underlayer, TiO₂ doped WO₃ films grown for shorter hydrothermal time of 30 minutes are fabricated. It is found that the compact underlayer is already formed to 200 nm (compare 250 nm after 2 hours), but the nano-pillars are short at an average length of 100 nm (compared with 350 nm after 2 hours). Furthermore, the total weights of WO₃-TiO₂ oxide deposited film plus powder precipitation, after drying at 450°C for 10 hours, are 0.138 g and 0.287 g after 30 minutes and 2 hours of hydrothermal reaction respectively; this compares to a maximum possible weight of 0.360 g which is calculated after hydrothermal for 4h and also drying at 450°C for 10 hours; i.e. 80% of the reacts have been consumed after 2 hours. This suggests that the switch from predominately compact film growth to the formation of nano-pillars is caused by the film deposition process becoming mass transport limited.

In addition, through comparing the morphology of pure WO₃ film with TiO₂ doped WO₃ film, it can be seen that the pure WO₃ shows higher aspect ratio.

The rod could be recognized as a combination of wires and slower growth rate of the formed crystallite. This variation from wire to rod is believed to be controlled by the different capping agents of sulfate ion (SO_4^{2-}) and (Cl^-) respectively. ^[13-15] In the pure WO_3 precursor solution, the sulfate ions play the dominate role, whereas Cl^- plays a decisive role in morphology control in the solution with mixture of WO_3 and TiO_2 precursor. This is due to the concentration of the Cl^- in TiO_2 precursor solution (20ml) being 6M, so even after mixing with WO_3 precursor solution (10ml) it remains at 4M, which is still much higher than the concentration of sulfate ions (0.09M). However, both of the SO_4^{2-} and Cl^- prefer to take up the faces parallel to c-axis of the WO_3 crystallite and hence lead to growth along preferential directions reflected from both the wire and rod structures. ^[13-17] Additionally, the absorbed Cl^- on the nano-rod can behave as a diffusion barrier for the further growth of the rods and prevent the solute diffusing to surfaces. ^[18-19] Therefore, a relative lower aspect ratio of nano-rod structure is observed in TiO_2 doped WO_3 film where the chloride concentration is high. Besides, a compact underlayer can be found in this TiO_2 doped WO_3 film.

According to Liu and Aydil, ^[20] the optimum ratio between de-ionized water (DI) and concentrated hydrochloric acid (37%, kg HCl/kg) is 1:1 for the growth of TiO_2 nano-rods under the hydrothermal conditions of 180°C for 2h and when the ratio goes beyond one, the hydrolysis of TiO_2 precursor will be accelerated.

This could be one reason responsible for the formation of a compact layer under the rods because of the higher ratio of 2:1 for the mixed precursor solutions. Another reasonable explanation is that the higher acidity (pH -0.6) of the mixed precursor solution, compared with pure WO_3 precursor solutions (pH 2), will also accelerate the precipitate rate of H_2WO_4 which then is decomposed to WO_3 as a relatively compact underlayer at the initial stages. Later on, once the film deposition process becoming mass transport limited, the crystallite starts to grow and form nano-rods structures. A proposed schematic illustration of the formation process of the nanorods is depicted in Figure 3.3.

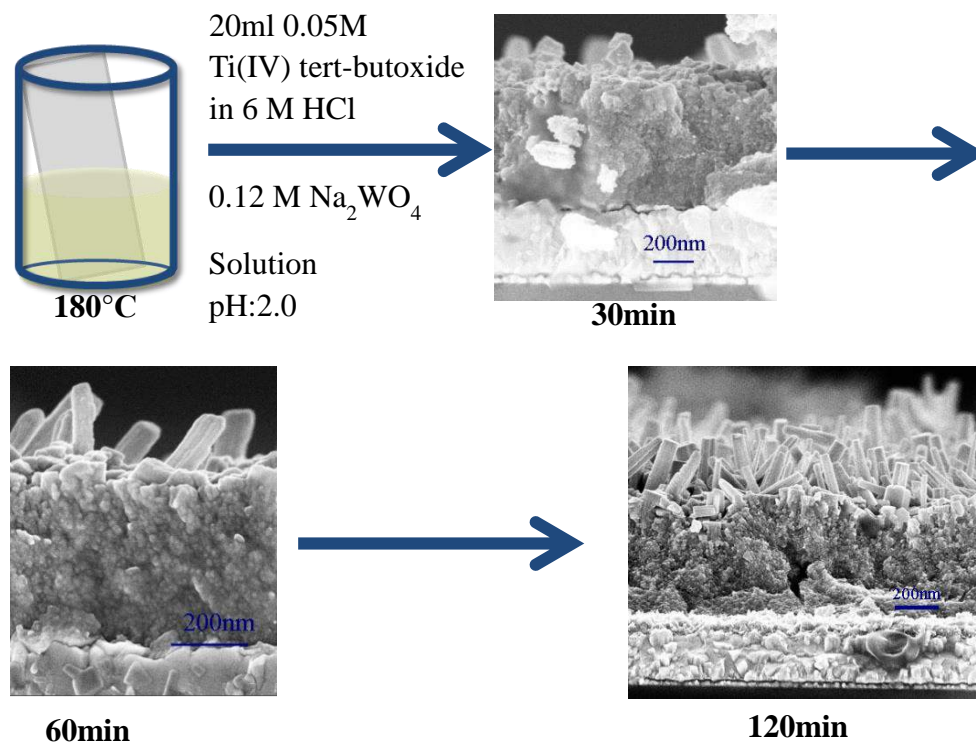


Figure 3.3. Schematic growth development of the double-layer structured TiO_2 mixed WO_3 thin film

3.2.2 Structural analysis

Figure 3.4 shows XRD patterns for pure WO_3 films which conform to the hexagonal structure with preferential growth of the planes (002) compared to the standard powder diffraction pattern. Based on the XRD patterns, the TiO_2 doped WO_3 films still maintain the same crystal structure as pure one.

The lattice parameters, listed in Table 3.2, are obtained by doing Refinement. The software of Topas version 4.2 is used for refinement. The XRD of titanium doped WO_3 is refined by assuming that the substitution of Ti atoms for W in WO_3 lattice does not change its phase and occupancy of Ti/W is assumed to be 4/1 according to the SEM-EDS analysis. From the result of the lattice parameters after refinement, it can be seen that the dope of titanium leads to a decrease of cell volume. Further comparing, it can be seen that this decrease should be attributed to compressive strain along c axis, which also can be determined by the shift of 2θ toward higher angle and shorten of d between two planes which are orthogonal to a direction (0 0 1) relative to pure WO_3 . The right shift of 2θ is possibly due to the substitution of titanium for tungsten introducing distortion in the film owing to the possibility of disturbing WO_6 octahedra by titanium cations.

In addition, it can be seen that the relative peak intensity diffracted from (0 0 1) plane, compared with peak intensities diffracted from other planes of itself, is

decreased relative to the pure WO₃ thin film. This decrease could come from the increased disorder in WO₃ lattice after doping of titanium.

Besides, there is no definite rutile or anatase peaks observed, the intensity of peaks at 27.77 and 25.46 degrees are stronger when TiO₂ is present in the film, which might indicate the presence of some rutile as its strongest peak appears at 27.75 degrees.

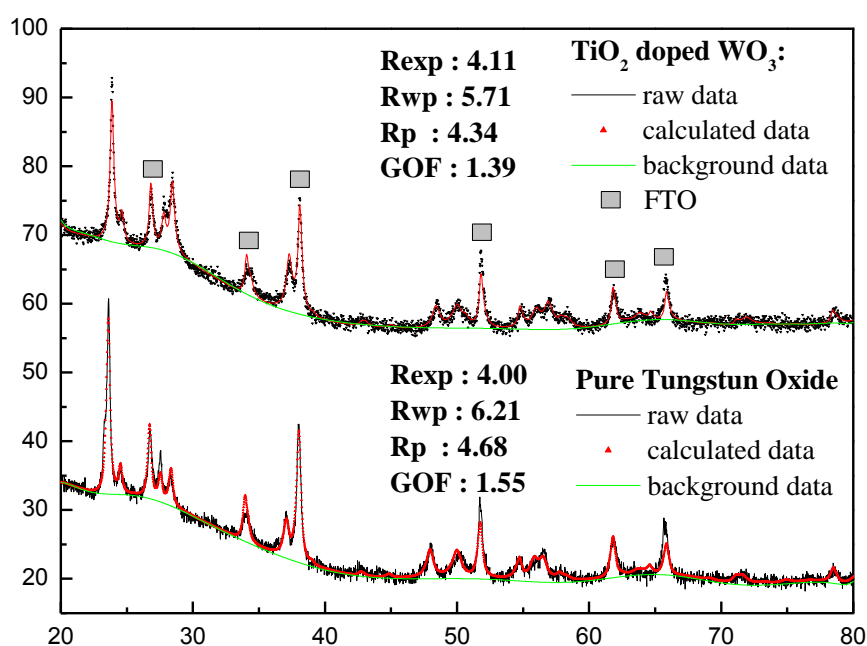


Figure 3.4 XRD patterns of pure WO₃ films and TiO₂ doped WO₃ films on FTO substrates. Peaks of Hexagonal WO₃ recorded by ICDD No. 01-085-245g.^[21]

Table 3.2 Lattice parameters of pure WO₃ and Titanium doped WO₃ thin films after refinement

| Thin film | Space group | Cell Volume (Å ³) | Lattice Parameter (Å) | |
|--------------------------------|-------------|-------------------------------|-----------------------|------|
| | | | a | c |
| Pure WO ₃ | P6/mmm | 176.97 | 7.33 | 3.81 |
| Titanium doped WO ₃ | P6/mmm | 176.81 | 7.34 | 3.78 |

Besides the XRD analysis, Figure 3.5 shows TEM images of TiO₂ doped WO₃ that has been scrapped from the FTO substrate and dispersed on copper grids for a further investigation on its structures. The average diameter of the nano-pillars is about 40 nm, while their length is typically 60 nm, which is much shorter than suggested by the SEM cross section images (Figure 3.1) suggesting that the nano-pillars fractured during the TEM preparation procedure. The insets of Figure 3.5a shows a high-resolution TEM image and a selected area electron diffraction pattern (SAEM). The HRTEM image shows a high degree of crystallinity with lattice spacing of about 0.361nm corresponding to the d-spacing of (002) planes. ^[21] This is consistent with the right shift of the peaks observed in XRD diffraction pattern so supports the idea of some W⁶⁺ being substituted by Ti⁴⁺ ions in the WO₃ lattice structure.

Figure 3.5b shows the elemental distribution in TiO₂ doped WO₃ nano-pillar selected from Figure 3.5a, from which it can be seen that both the titanium and tungsten are evenly distributed throughout the structure. The EDS attachment on the TEM also revealed that the atomic ratio of W: Ti in the nano-pillar is approximately 2.86:1, which is more than two times the value of 1.2:1 expected from the concentrations of the initial reactants but close to that determined by EDS. The proposed reason is the different nucleation rates between the hydrophilic WO₃ precursor and the lipophilic Ti(IV) tert-butoxide solution. In addition, tert-butyl alcohol produced during hydrolysis has been report to act as

a buffer controlling the rate of hydrolyze of the TiO_2 precursor. ^[22] Therefore, the obtained W/Ti ratio is higher than calculated from the initial concentrations of the reactants.

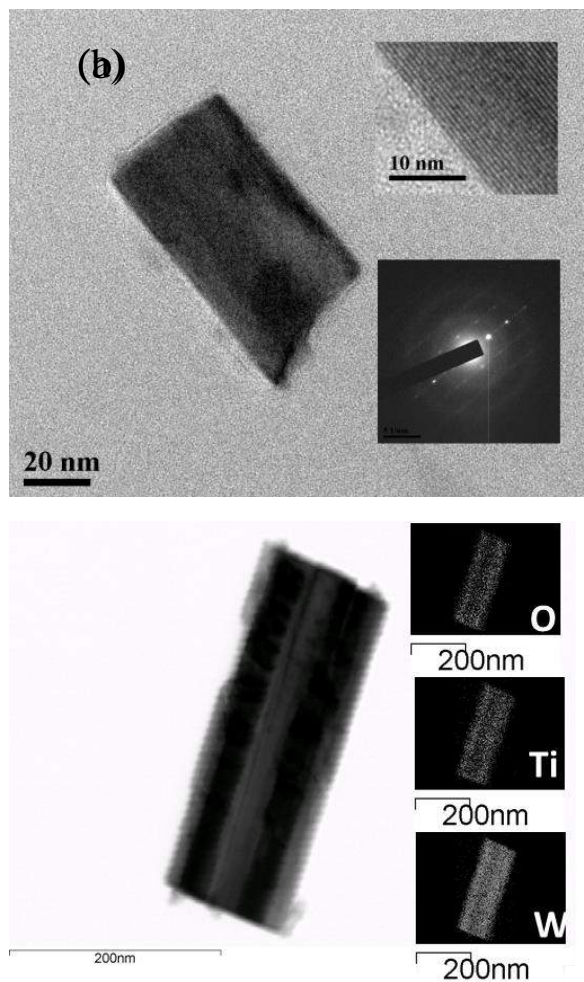
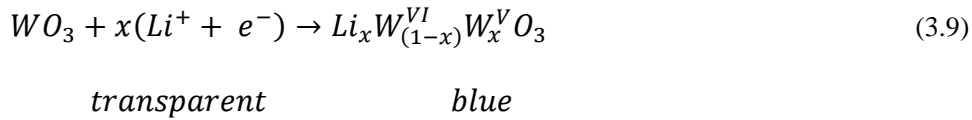


Figure 3.5 (a) HRTEM image of TiO_2 doped WO_3 nano-pillar and (b) corresponding elemental distribution maps.

3.2.3 Electrochemical analysis

After analyzing the structures of the obtained film, in this section, the results of electrochemical analysis will be displayed and discussed. Figure 3.6 shows the

cyclic voltammograms (CV) of the synthesized WO₃ films with and without TiO₂ incorporations. As the potential is swept in the negative direction both films switch from being transparent to a deep blue color due to lithium ion intercalation: [23]



The stability of the electrochromic process can be ascertained from the charge passed during successive cycles, i.e. changes in the area enclosed by the CV curves. Figure 3.6 reveals that the CV curves of TiO₂ doped WO₃ films are much more stable than those of their standard WO₃ counterparts. It can be seen that the intercalation (charge) capacity of the former shows only a small decline after 1000 cycles, whereas the latter declines rapidly after about 300 cycles. This can be ascribed to the more compact structure of the TiO₂ doped WO₃ film (Figure 3.1), since a film's dissolution rate is expected to be directly related to its porosity.

Further inspection of the CV curves of the TiO₂ doped WO₃ film reveals that the anodic deintercalation (bleaching) peak, due to oxidation of the W(IV/V) back to W(VI), [24] slightly narrows and shifts towards more negative potentials following a sequence of 0.037 V, -0.069 V, -0.083 V and -0.118 V corresponding to observations at its 1st, 100th, 500th and 1000th cycle respectively. This slight

variation should be due to the partly distributed charges which are not extracted in time. However, there is no significant change in the magnitude of the peak's current density, which suggests good film stability; i.e. the overall charge under the peak remains almost constant even though its position shifts slightly. Furthermore, the overall cathodic profile CV for the TiO₂ doped WO₃ film shows few variation within 1000 cycles, indicating a stable intercalation process (there is some growth near -0.6V, perhaps indicating evolution of hydrogen absorbing from atmosphere). In contrast, the standard WO₃ film the current densities of both the deintercalation (anodic) and intercalation (cathodic) peaks decreased significantly after about 300 cycles (Figure 3.7).

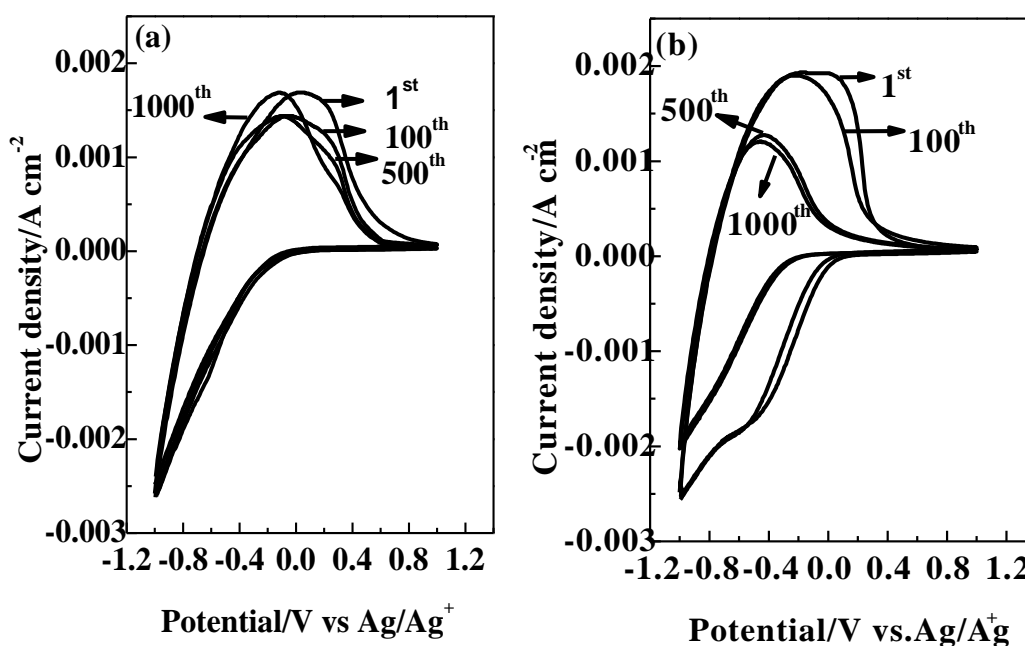


Figure 3.6 Cyclic voltammograms showing the 1st, 100th, 500th and 1000th cycles for (a) TiO₂ doped and (b) pure WO₃ films in 1 M LiClO₄ dissolved in propylene carbonate at a sweep rate of 50 mV s⁻¹.

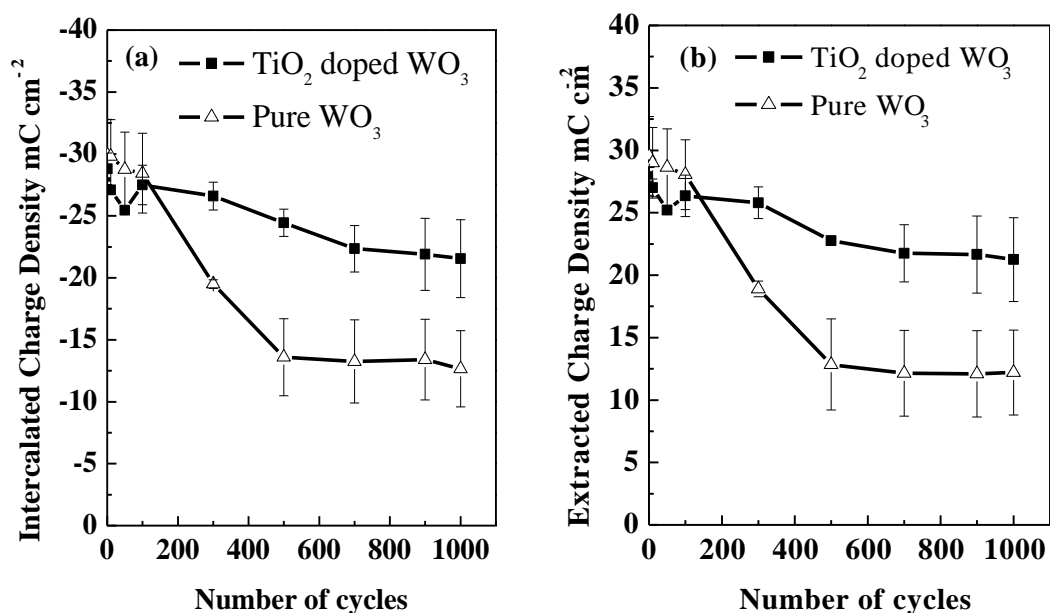


Figure 3.7 Comparison of (a) intercalated charge density against the number of cycles and (b) extracted charge density against the number of cycles corresponding to Figure 3.6. Solid squares with TiO₂ dopants, open triangles without TiO₂ dopants. (The values and the corresponding deviation in the image come from the average of the result based on conducting the test twice.)

3.2.4 Electrochromic results

The main idea of fabricating TiO₂ doped WO₃ film is for the purpose of application on “Smart Windows”, hence, the electrochromic properties are important in this study. The electrochromic features of the two types of WO₃ films were investigated by UV-vis spectroscopy. With freshly prepared samples being subject to either +2 V for 30 s or -2 V vs. Ag/Ag⁺ for 60 s to obtain the bleached and blue colored states respectively. The transmission curves and its corresponding optical images in Figures 3.8 and 3.9 reveal that the presence of TiO₂ leads to a more intense blue color. The transmittance of pure WO₃ thin

film is 33 % at a wavelength of 500 nm after coloration which is 30 % lower than the titanium doped WO₃ thin film. In addition, within infrared range, the transmittance of the titanium doped WO₃ thin film is close to zero at 1100 nm but 17 % for pure WO₃ thin film.

In the bleached state the presence of the TiO₂ leads to increased transmission over the entire visible region, except for the far blue end below 420 nm as the band gap of TiO₂ (3.2 eV; 387 nm) is approached. The transmittance modulation range of TiO₂ doped WO₃ films reaches 67.4% at 632nm, while the pure WO₃ films is only about 30% at the same wavelength. Figure 3.9 shows optical images that confirm the relative electrochromic performance of the two types of WO₃ films, as well as revealing the excellent uniformity of these films produced through the one step hydrothermal method.

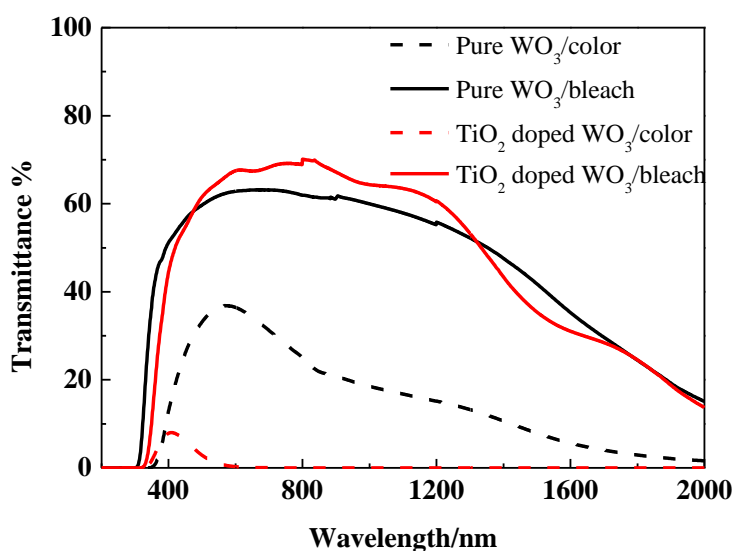


Figure 3.8 UV-vis transmittance spectrum of the TiO₂ doped (red solid lines)

and pure (black dashed lines) WO₃ films in the colored and bleached states.

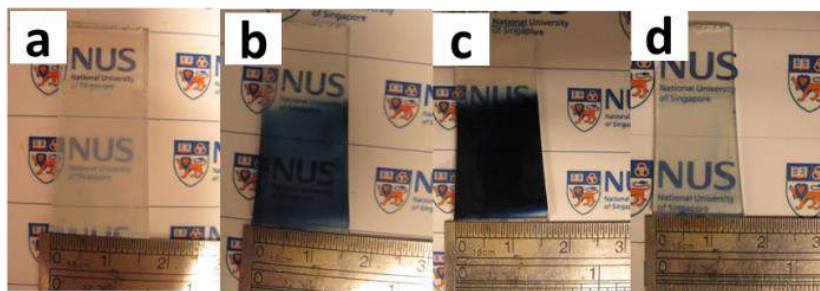


Figure 3.9 Digital photographs of the TiO₂ doped WO₃ films at different stages: (a) as-prepared; (b) colored at -1.0 V for 30 s; (c) colored at -2.0 V for 30 s; (d) bleached at 2.0 V for 60 s.

Figure 3.10 shows the chronoamperometry response of WO₃ films with and without TiO₂ incorporations, along with their corresponding *in situ* transmittance at 632.8nm, in response to a series of potential pulses of -2 V for 60 s and 2V for 100 s. It can be seen that TiO₂ incorporations increase the magnitude of both the anodic and cathodic current densities peaks, which suggest that the dope of TiO₂ has increased the number of coloring centers in the WO₃ film. Likewise it improves the stability of the adhesion of the films to the FTO substrates, with the chronoamperometry response showing only a small decrease after 500 pulse cycles. In contrast, for the pure WO₃ film, a sudden increase in current density and decay time during charge insertion and extraction processes implies that this film is detaching from the FTO substrate due to a weak adhesion.

Inspection of Figure 3.10 (b) shows that in the absence of TiO₂ bleaching occurs at a faster rate than coloration, but this trend is reversed in the TiO₂ doped

samples. Switching times for both the coloration (τ_c) and bleaching (τ_b), are defined as the time required for a 90% change within the full transmittance change range at the selected wavelength. For TiO₂ doped WO₃ thin film, τ_c and τ_b were found to be 21 s and 26 s respectively, while values of 16 s and 12 s were obtained for pure WO₃ thin film. Although the presence of TiO₂ increased the switching times this does not mean it decreased the switching rates as it almost doubled the modulation range of the transmitted light from about 35% to 68%. To illustrate this point the coloration (r_c) and bleaching (r_b) rate is determined 10 seconds after the switch in applied voltage from the gradients of Figure 3.10 (b) and (d) as 4.51% s⁻¹ and 0.77% s⁻¹ for the TiO₂ doped film which are faster than the 2.62% s⁻¹ and 0.25% s⁻¹ for pure WO₃ counterpart. Thus the switching rates of TiO₂ doped WO₃ thin film is twice as fast as the pure WO₃ film. Furthermore, after 500 cycles, the TiO₂ doped WO₃ film still retains a good light modulation ability and high electrochromic switching rate. However, for the same 500 cycles the transmittance in color state of the pure WO₃ film increases to 43%, indicating partial peeling off of film. This result is in agreement with conclusions of the chronoamperometry curves, which are expected to depend on morphologies.

The observed changes in optical transparency with the pure WO₃ film likely arises almost exclusively from near surface intercalation processes, whereas in the presence of TiO₂ bulk intercalation processes dominate giving rise to a

greater modulation range but longer switching times. The impact is the greatest on the deintercalation process, suggesting that it is harder for ions to migrate out of the bulk of the film than into it. This should be attributed to the compact under layer of the obtained TiO₂ doped WO₃ film.

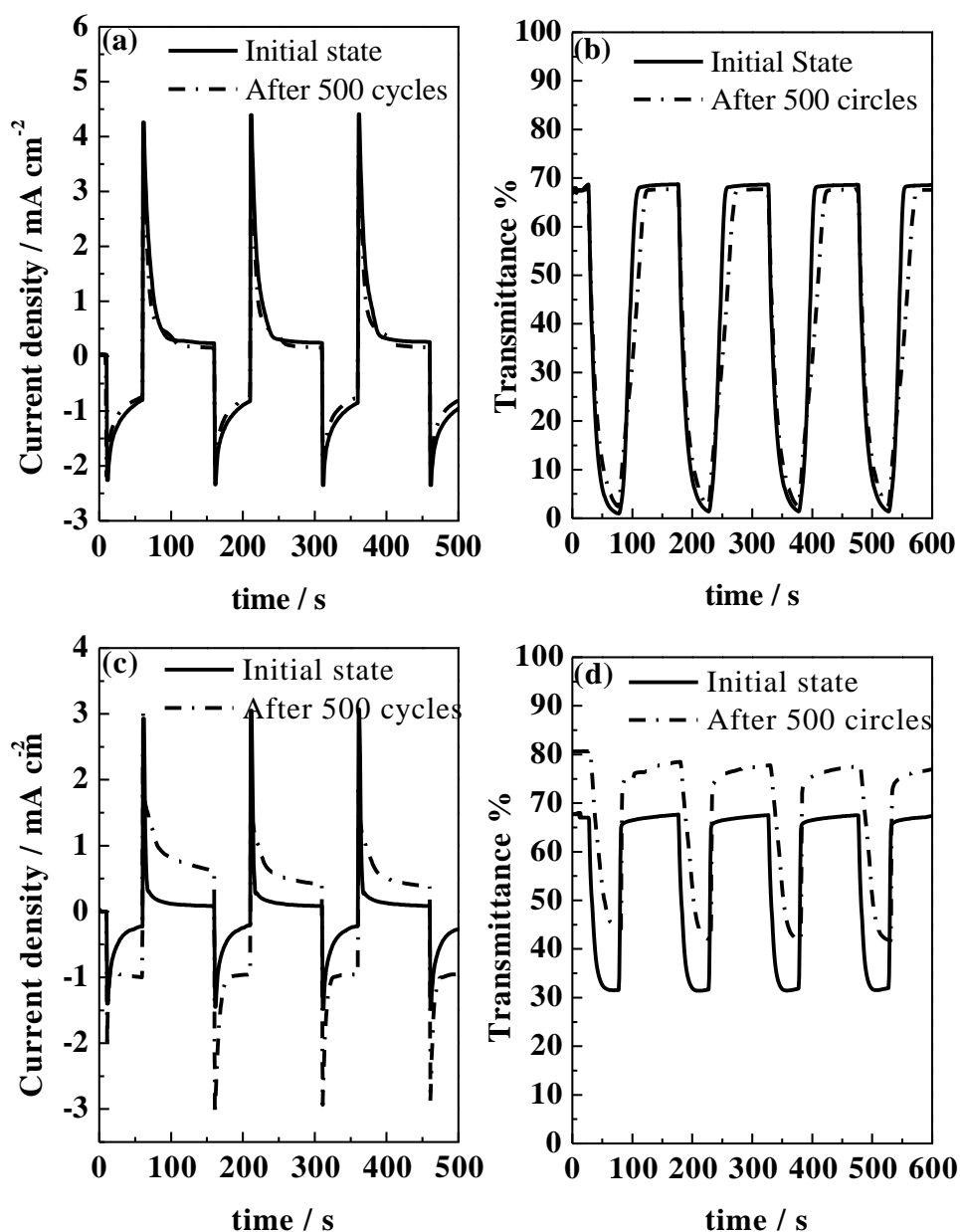


Figure 3.10 Chronoamperometry curves and the corresponding in situ transmittance at 632.8 nm for TiO₂ doped WO₃ films (a), (b) and pure WO₃ films (c), (d). Recorded by switching the applied potential repeatedly between -2.0 V and +2.0V vs Ag/Ag⁺ in 1 M LiClO₄ dissolved in propylene carbonate for 60s and 100s respectively. Solid lines show the initial response, dashed lines

show the response after 500 cycles.

Figure 3.11 depicts the change in optical density at 632.8 nm as a function of the inserted charge density for WO₃ films with and without TiO₂ dopants. From this figure, an important electrochromic parameter can be found and it is defined as coloration efficiency. Coloration Efficiency (CE) is a characteristic parameter used for comparing the electrochromic property of different materials and is defined as:

$$CE(\lambda) = \frac{\Delta OD}{Q} \quad (3.10)$$

$$\Delta OD(\lambda) = \log \frac{T_b}{T_c} \quad (3.11)$$

Where ΔOD is the change in optical density, which is proportional to the amount of created color centers of the film, T_b and T_c are the transmittances before and after coloration at a given wavelength (λ) and Q is the corresponding amount of injected (or ejected) charges per unit area, obtained by integration of the corresponding current density transient curve (Figure 3.10).

According to Equation (3.10~3.11) the coloration efficiency is obtained from the slope of the linear portion of the plots, reflecting the change in optical density per amount of inserted charge and giving rise to values of 39.2 cm² C⁻¹ and 26.5 cm² C⁻¹ for WO₃ films with and without TiO₂ dopants respectively. The higher CE value of TiO₂ doped WO₃ film can be ascribed to its larger

optical modulation range. Analysis of Figure 3.11 also reveals that in the absence of TiO₂ the change in optical density becomes inefficient after the passage of the first 13 mC cm⁻², which is equivalent to 24 C g⁻¹ of WO₃. If it is assumed that all the charge is solely due to insertion of Li⁺ ions this yields an average composition of colored state of Li_{0.06}WO₃, which is half an order of magnitude higher than that reported by Fabregat-Santiago *et al* for films prepared by dip-coating. [25]

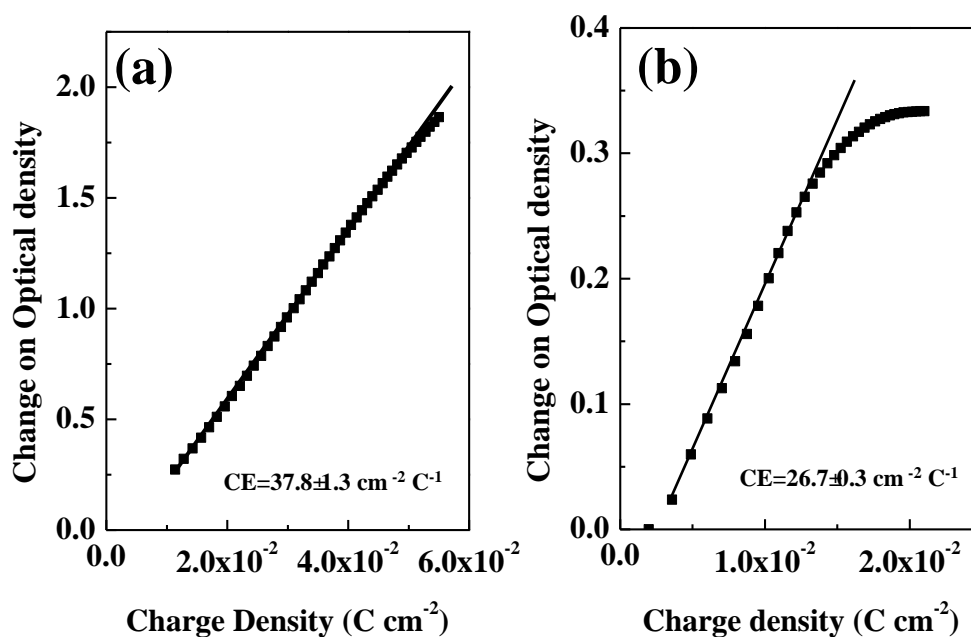


Figure 3.11 The variation of the *in-situ* change in optical density (ΔOD) versus the charge density for the (a) TiO₂ doped WO₃ films and (b) pure WO₃ films. The ΔOD was measured at 632.8 nm at a potential of -2.0 V Ag/Ag⁺. (Note that the deviation of the CE is calculated based on the Figure 3.10(b). In Figure 3.10(b), the transmittance - time curve of TiO₂ doped WO₃ has four cycles, so each cycle gives a value of CE, based on these values an average deviation of the CE of TiO₂ doped WO₃ is obtained and shown in the above image. The value of 23.8 is the average value of the four values of CE. The CE deviation of pure WO₃ is obtained with the same method.)

Until this point the electrochromic investigation focused on a selected

wavelength at 632.8 nm, so in order to study the electrochromic properties in more depth the experiments were repeated at an addition two wavelengths, 500 nm and 1200 nm. Figure 3.12 shows the *in-situ* transmittance change at different wavelengths (500, 632.8 and 1200 nm) under the same electrochemical conditions. It exhibits that overall the TiO₂ doped WO₃ show a better light adjusting capacities reflected from the larger light modulation range at these three wavelengths respectively through comparing with the pure WO₃ thin film. Based on Figure 3.12, the influence of wavelength (500, 632.8 and 1200 nm) on the coloration efficiency was calculated and listed in Table 3.3; also including the coloration and bleaching times and the transmittance modulation range for the two types of film. It can be seen that for the pure WO₃ film the CE decreases at shorter wavelengths, with a >70% decline on going from 1200 nm to 500 nm, largely due to a decrease in ΔT . Although for the TiO₂ doped WO₃ film the CE showed the same trend, the decline is much smaller <15% over the same wavelength range, with the ΔT values also less dependent on wavelength. There is no clear correlation between wavelength and the coloration/bleaching times, however, the magnitude of the variations are unlikely to be significant in a practical smart window.

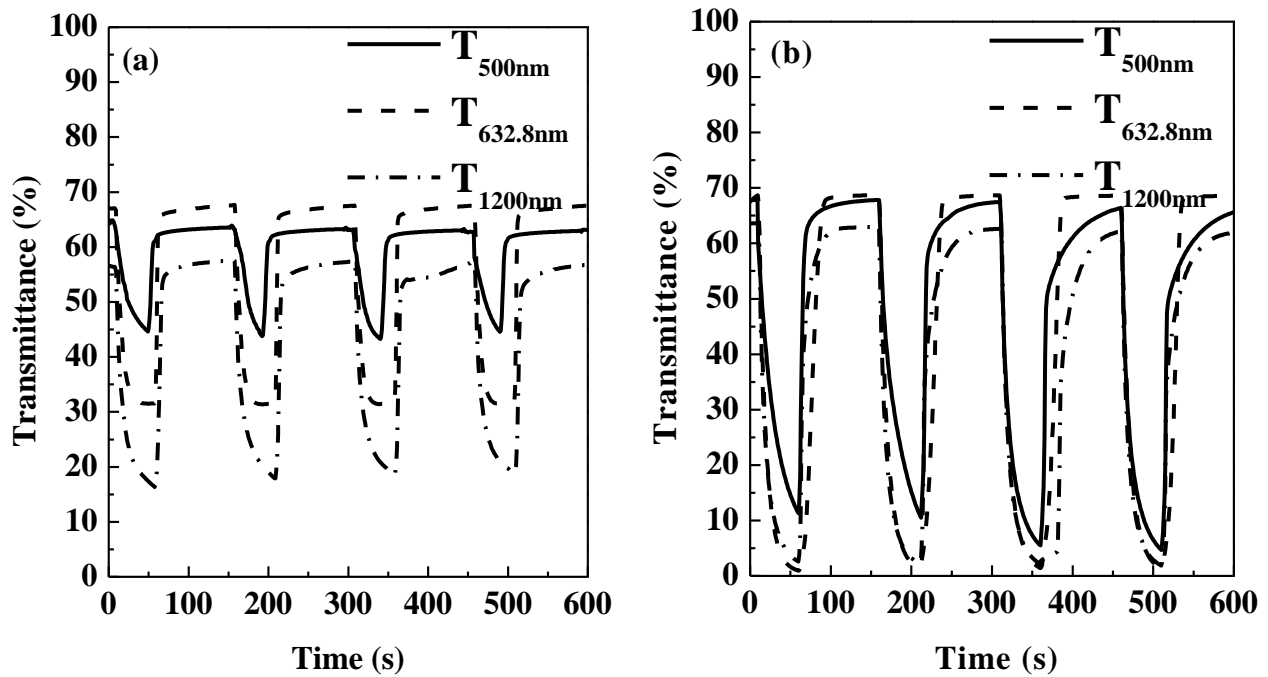


Figure 3.12 in situ transmittance at 500nm (solid line), 632.8 nm (dashed line) and 1200nm (dot-dash line) for pure WO_3 films (a) and TiO_2 doped WO_3 films (b).

Table 3.3 Influence of wavelength on the coloration efficiency, the coloration and bleaching times and the transmittance modulation range for the two types of film.

| | Wavelength nm | CE $\text{Cm}^{-2} \text{C}^{-1}$ | t_c s | t_b s | ΔT % |
|------------------------------------|------------------|--------------------------------------|------------|------------|-----------------|
| Pure WO_3 | 500 | 8.8 ± 0.05 | 30 | 12 | 20 |
| | 632.8 | 26.5 ± 0.53 | 16 | 12 | 35 |
| | 1200 | 34.0 ± 1.12 | 26 | 20 | 41 |
| TiO_2 doped WO_3 | 500 | 36.7 ± 0.06 | 39 | 17 | 58 |
| | 632.8 | 39.2 ± 0.15 | 21 | 26 | 68 |
| | 1200 | 42.4 ± 0.18 | 23 | 22 | 62 |

The error is the standard deviation obtain from linear simulations by Origin 8.0 software.

3.2.5 Electrochemical impedance analysis

In order to obtain more details of the charge transportation on the surface of and

within the discussed films, electrochemical impedance measurements were performed. Figure 3.13 shows impedance spectra in the Nyquist format for WO_3 films with and without TiO_2 dopants measured in their colored state at -0.4 V Ag/Ag^+ , corresponding to the cathodic peak position observed in their cyclic voltammetry curves. The solid lines in the plots are the fitting result related to the experimental data based on the equivalent circuit shown in Figure 3.14, often used to describe Li batteries that are mechanistically very similar to electrochromic windows, ^[26] where: R_s represents contact resistance originating from FTO substrate, electrical wire and solution. Q_{dl} is constant phase element used to describe the double layer capacitance formed between the inhomogeneous inner surfaces and the electrolyte inside the bulk material. R_f is the resistance resulted from the inter valence charge transfer between W^{V} and W^{VI} inside bulk materials. Q_{in} is the double layer capacitance at the contact between the inhomogeneous film surface and the electrolyte solution. R_{in} is the resistance of inter valence charge transfer between W^{V} and W^{VI} on the film surface and W_s is the finite length Warburg impedance, designated by R_w , used for describing the diffusion resistance of the species from electrolyte bulk solution to the film. The same equivalent circuit and meaning of respective symbol is also used in later chapters for EIS simulation and explanation.

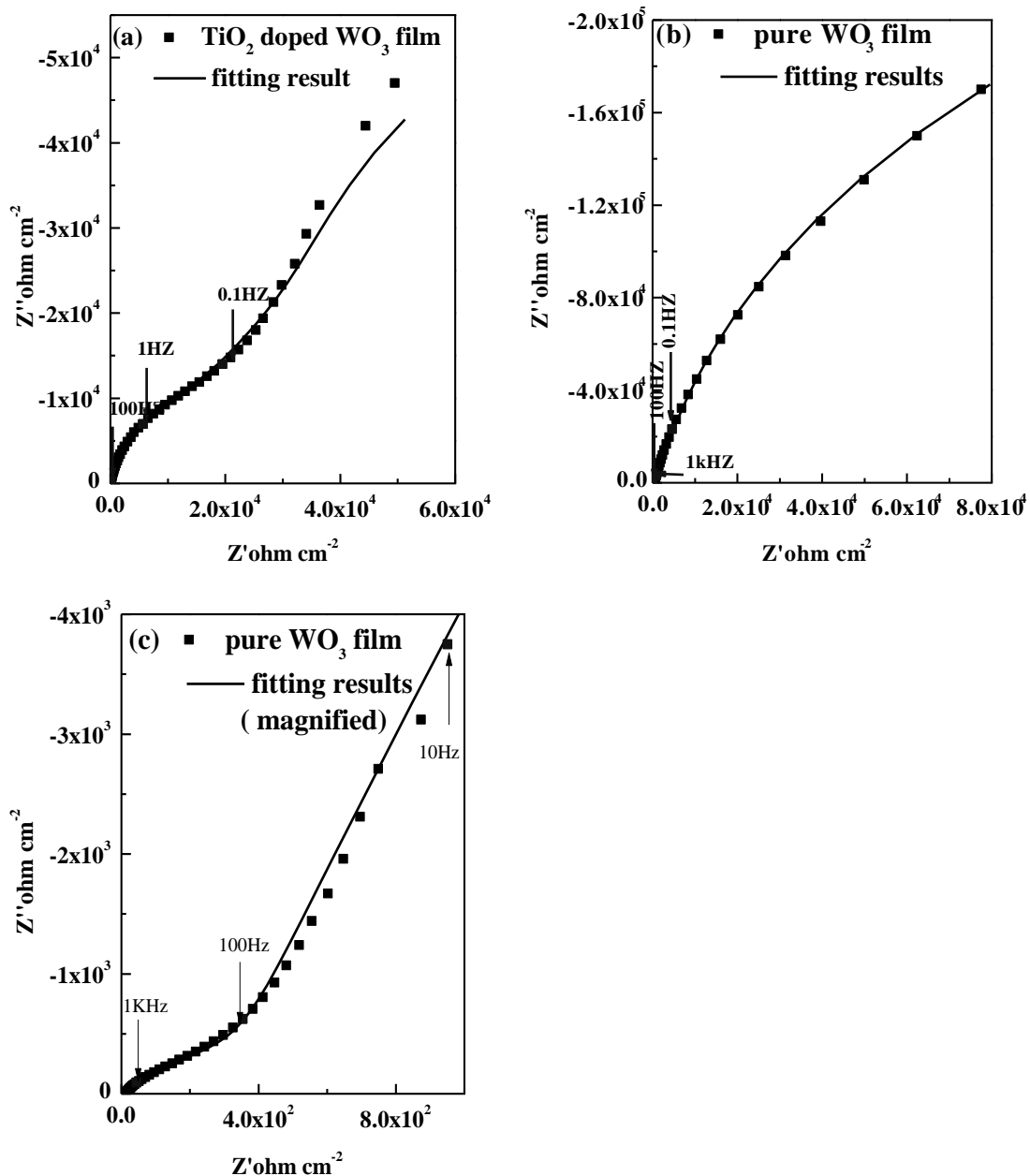


Figure 3.13 Nyquist plots for WO_3 films with (a) and without (b) TiO_2 dopants at -0.4V vs Ag/Ag^+ 1 M LiClO_4 dissolved in propylene carbonate. (c) Magnification of the high frequency region for the pure WO_3 film.

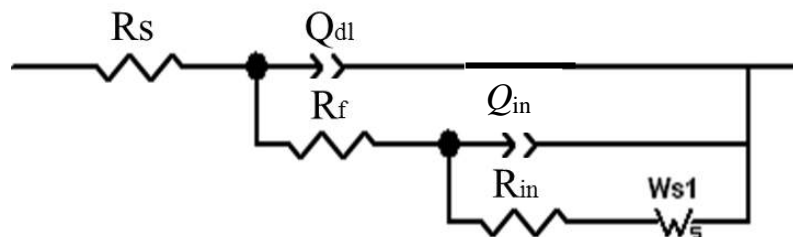


Figure 3.14 Equivalent circuit used to fit the impedance data of WO_3 films both with and without TiO_2 dopants.

$$Z_{CPE} = \frac{1}{(i\omega Q)^n} \quad (3.13)$$

$$Z_{Warburg} = R_w \frac{\tanh(i\omega\tau_w)^{\frac{1}{2}}}{(i\omega\tau_w)^{\frac{1}{2}}} \quad (3.14)$$

$$\tau_w = \frac{L^2}{D} \quad (3.15)$$

where Q and n are the prefactor and index of the constant phase element, ω is the angular frequency of the applied voltage perturbation, R_w is the resistance of the Warburg element at zero Hz, τ_w is a time constant, L is the film average thickness and D is the chemical diffusion coefficient. [22]

Table 3.4 shows the parameters required to fit the equivalent circuit shown in Figure 3.14 to the impedance plots of Figure 3.13. Table 3.4 also shows the variations in the fitting parameters between nominally the same films along with the percentage fit errors that report the quality of the fit to an individual film, which in most cases was very good. The semicircle observed at higher frequencies has been attributed to the diffusion of lithium ions onto the surface of the film (Figure 3.13). The absence of this semicircle for TiO₂ doped WO₃ thin film indicates a faster process of ion diffusion onto the film surface, which is consistent with the faster switch rate observed for the coloration process.

Table 3.4 reveals that the addition of TiO₂ has reduced the resistance of the film (R_f) by almost a factor of 20. The improved conductivity of the film could be due to the substitute of W⁶⁺ with Ti⁴⁺ ions resulting in a higher density of oxygen

vacancies. A further comparison can be found for the Warburg impedance in Table 3.4 where the lower R_w of the TiO₂ doped WO₃ film, compared to its pure WO₃ counterpart, indicates that the presence of TiO₂ allows better diffusion of ions in depth, which is consistent with the observed deeper blue coloration. The higher R_{in} and lower Q_{in} values of the TiO₂ doped WO₃ film, could result from a lower specific surface area making harder to insert Li⁺ ions into the film's surface; the nanowire structure of the pure WO₃ film can be expected to have a large surface area (Figure 3.1). This result is consistent with the cyclic voltammetry curves which show that during the first cycle the amount of charge inserted into TiO₂ doped WO₃ film is less than that into the pure WO₃ thin (Figure 3.6). Therefore the impedance data shows that the TiO₂ improves the electrochromic properties of the WO₃ films by reducing both the film's electrical resistance and resistance to diffusion of ions within the film.

Table 3.4 Parameters determined from fitting the EIS data to the equivalent circuit in Figure 3.14, along with the variation between nominally the same films and the percentage fit errors that give an indication of the quality of the fit to an individual film (see Chapter 2).

| Film | R_s $\Omega \text{ cm}^{-2}$ | R_f $\Omega \text{ cm}^{-2}$ | ${}^aR_{in}$ $\Omega \text{ cm}^{-2}$ | Q_{dl} $(\mu\text{F cm}^{-2})^{1/n}$ | n_{dl} | Q_{in} $(\mu\text{F cm}^{-2})^{1/n}$ | n_{in} | R_w $\Omega \text{ cm}^{-2}$ | τ_w s |
|--|-----------------------------------|-----------------------------------|--|---|----------|---|----------|-----------------------------------|---------------|
| TiO ₂ doped WO ₃ | 19 | 29 | 29000 | 31 | 0.82 | 1.4 | 0.96 | 180000 | 110 |
| Error(+/-) | 3 | 16 | 13000 | 29 | 0.01 | 0.4 | 0.04 | 57000 | 37 |
| Fit error (%) | 2 | 19 | 2 | 2 | 1 | 32 | 2 | 4 | 6 |
| WO ₃ | 14 | 520 | 4500 ^a | 50 | 0.87 | 22 | 0.96 | 63000 | 6 |
| Error(+/-) | 0.1 | 345 | 4500 | 11 | 0.02 | 8 | 0.03 | 32000 | 3 |
| Fit error (%) | <1 | 2 | >200 | 1 | <1 | 1 | <1 | 2 | 6 |

^a R_{in} values for individual pure WO₃ films vary from 0 to 9000 $\Omega \text{ cm}^{-2}$; the large error is due to its small magnitude as compared to R_w .

3.3 Conclusions

The influence on electrochromic properties of TiO₂ doped WO₃ thin film has been investigated by both optical and electrochemical techniques, with both types of films being obtained through a simple one step hydrothermal method. The synthesized TiO₂ doped WO₃ thin films show a two layer structure consisting of nanopillars on top of a compact layer, with both layers having the same Ti/W atomic ratio. It is postulated that the switch from growth of the compact layer to nanopillars is due to hydrothermal reaction becoming mass transport limited at the surface. The obtained TiO₂ doped WO₃ thin film shows a preferential growth of (002) plane and good crystallinity with hexagonal

structure. XRD and TEM investigations on TiO₂ doped WO₃ thin films suggest substitution of W⁶⁺ by Ti⁴⁺ ions in the WO₃ lattice structure, rather than discrete phases of WO₃ and TiO₂.

The TiO₂ doped WO₃ thin film shows improvements on the electrochromic properties as compared to the pure WO₃ films. This includes more than doubling the transmittance modulation at 632.8 nm to 67% and increasing the coloration efficiency by 50% to 39.2 cm² C⁻¹. If it is assumed that all the measured cathodic current is due to insertion of Li⁺ ions, then the presence of the TiO₂ more than doubled the loading to 80 C g⁻¹, which is of the same order as materials designed for use in lithium batteries. Electrochemical impedance measurements suggest that the improvement in the electrochromic properties are due to the presence of the TiO₂ reducing both the film's electrical resistance and resistance to diffusion of ions within the film. Additionally, the stability of the TiO₂ doped WO₃ thin film is also improved, with only limited degradation being observed after 500 coloration/bleaching cycles, compared to significant degradation after 500 cycles in its absence.

In summary, in this chapter the main contribution is the investigation on electrochromic properties of TiO₂ doped WO₃ thin films fabricated by using the hydrothermal method, which is a simple inexpensive way to obtain crystalline thin films with good morphology. Although hydrothermal TiO₂/WO₃ mixed

films have previously been produced these were for photocatalytic applications, with TiO₂ being the major component rather than WO₃. The high reversibility and stability of TiO₂ doped WO₃ thin film appears to be in agreement with the electron-beam deposited mixed films produced by Hashimoto and Matsuoka^[27] as well as films formed by sputtering and sol-gel by Gottsche *et al.*^[28] The coloration/bleaching time of the hydrothermally synthesized TiO₂ doped WO₃ thin films are also very similar to films produced by the other two more expensive methods.

The greater than 68% transmittance modulation range at 632.8 nm of the present TiO₂ doped WO₃ thin film is comparable to the 70% (700 nm) modulation reported by Nguyen *et al.*^[29] for a more complicated two step method of doctor blading TiO₂ followed by electrochemical WO₃ deposition, but superior to the 50% (450 nm~900 nm) and 40% (630 nm) modulations reported for films prepared by spray pyrolysis by Bathe and Patil.^[30] and spin coating by Wang and Hu,^[9] respectively. Furthermore, unlike TiO₂ doped WO₃ thin film produced by spray methods the TiO₂ doped WO₃ thin film reported in this thesis does not show any detriment to the transparency of its bleached state.

References:

- [1] G. A. Niklasson and C. G. Granqvist, *J. Mater. Chem.*, **17** (2007) 127
- [2] A. Bessi`ere, C. Marcel, M. Morcrette, J. M. Tarascon, V. Lucas, B. Viana, and N. Baffier, *J. Appl. Phys.*, **91(3)** (2002) 1589
- [3] C. G. Granqvist, *Sol. Energ Mat. Sol. C.*, **92** (2008) 203

- [4] S. E. Lee and P. Rajagopalan, *Energy Policy*, **36** (2008) 3982
- [5] B.P. Jelle, G. Hagen S. Sunde, R. Ødegård, *Synthetic Metals*, **54(1–3)** (1993) 315
- [6] C. G. Granqvist, *Sol. Energ Mat. Sol. C.*, **92** (2008) 203
- [7] Z. H. Jiao, X. Wang, J. M. Wang, L. Ke, H. V Demir, T. W. Koha, and X. W. Sun, *Chem. Commun.*, **48** (2012) 365
- [8] Z. H. Jiao, X. W. Sun, J. M. Wang, L. Ke, and H. V. Demir, *J. Phys. D: Appl. Phys.*, **43** (2010) 285501
- [9] Z. C. Wang and X. F. Hu, *Electrochimica Acta.*, **46** (2001) 1951
- [10] J. Zhang, J. P. Tu, X. H. Xia, X. L. Wang, and C. D. Gu, *J. Mater. Chem.*, **21**(2011) 5492
- [11] W. P. Liao and J. J. Wu, *J. Mater. Chem.*, **21** (2011) 9255.
- [12] E. A. Barringer and H. K. Bowen, *Langmuir*, **1** (1985) 414.
- [13] J. M. Wang, E. Khoo, P. S. Lee and J. Ma, *J. Phys. Chem. C*, **112** (2008) 14306.
- [14] J. M. Wang, E. Khoo, P. S. Lee and J. Ma, *J. Phys. Chem. C*, **113** (2009) 9655.
- [15] Z. J. Gu, T. Y. Zhai, B. F. Gao, X. H. Sheng, Y. B. Wang, H. B. Fu, Y. Ma and J. N. Yao, *J. Phys. Chem. B*, **110** (2006) 23829.
- [16] A. Phuruangrat, D. J. Ham, S. J. Hong, S. Thongtem and J. S. Lee, *J. Mater. Chem.*, **20** (2010) 1683.
- [17] J. H. Ha, P. Muralidharan and D. K. Kim, *J. Alloys Compd.*, **475** (2009) 446.
- [18] R. Xu, H. C. Zeng, *J. Phys. Chem. B*, **107** (2003) 926–930.
- [19] J. Feng, H. C. Zeng, *Chem. Mater.*, **15** (2003) 2829–2835.
- [20] B. Liu and Eray S. Aydil, *J. Am. Chem. Soc.*, **131** (2009) 3985–3990
- [21] The International Centre for Diffraction Data used. ICDD No. 01-085-245g.
- [22] Q. H. Mu, Y. G. Li, H. Z. Wang, and Q. H. Zhang, *J. Colloid Interface Sci.*, **365** (2012) 308
- [23] D. T. Gillaspie, R. C. Tenent, and A. C. Dillon, *J. Mater. Chem.*, **20** (2010) 9585.
- [24] M. Z. Najdoski and T. Todorovski, *Mater. Chem. Phys.*, **104** (2007) 483.
- [25] F. Fabregat-Santiago, G. Garcia-Belmonte, J. Bisquert, N. S. Ferriols, P. R. Bueno, E. Longo, J. S. Anton, and S. J. Castro-Garcia, *J. Electrochem. Soc.*, **148** (2001) E302.

- [26] Y. M. Choi, S. I. Pyun, S. I. Moon, and Y. E. Hyung, *J. Power Source*, **72** (1998) 83.
- [27] S. Hashimoto and H. Matsuoka, *J. Electrochem. Soc.*, **138** (1991) 2403
- [28] J. Gottsche, A. Hinsch, and V. Wittwer, *Sol. Energ Mat. Sol. C.*, **31**(1993) 415
- [29] N. N. Dinh, D. H. Ninh, T. T. Thao, and V. V. Truong, *J. Nanomater.*, (2012) 781236.
- [30] S. R. Bathe and P. S. Patil, *Solid State Ionics*, **179** (2008) 314

Chapter 4 Comparison of WO₃ and TiO₂ doped WO₃ thin films formed by co-anodizing in organic solutions and their electrochromic properties

Chapter 3 shows that a self-assembled two-layer structured TiO₂ doped WO₃ film has improved electrochromic properties compared to the pure WO₃ fabricated by the same method. However, the compact under-layer produced by the hydrothermal method exhibits negative effect on the aspect ratio. Therefore, in order to further improve the electrochromic properties of WO₃ based thin films an effective way is to further enlarge its specific surfaces area, as this is responsible for accommodating more charges and creating spacious channels for the charge transportation. Based on this consideration, in this chapter, a convenient way of synthesizing oxide thin films with ordered porous structures based on electrochemical anodization in a fluoride containing electrolyte of pre-sputtered mixed Titanium/Tungsten films is introduced. The titanium/tungsten (Ti/W) thin film on FTO substrate is obtained by sputtering pure titanium and pure tungsten target simultaneously in RF the sputtering chamber.

4.1 Introduction

The electrochromic properties of the TiO₂ doped WO₃ system has attracted significant interesting due to its special enhancement in stability and cycle

life.^[1-5] Especially, in Chapter 3, a self-assembled two-layer structured TiO₂ doped WO₃ film prepared by a one-step hydrothermal method shows improved electrochromic capacities of light modulation range. However, an undesirable compact layer is observed in this film, so an alternative method to produce TiO₂ doped WO₃ thin film in liquid phase is, presented in this Chapter, the anodization method.

The anodization of pure tungsten for the purpose of fabricating WO₃ nanostructures has been previously reported in solutions containing HF,^[6] highly concentrated nitric acid^[7-8] and phosphoric acid^[6]. However, in this chapter, an organic anodization solution of ethylene glycol is prepared, as previously used for the growth of titanium nanotubes.^[9] Besides, the addition of HF is replaced by a small amount of NH₄F.

Previous methods used to produce WO₃-TiO₂ composite thin films include electron-beam deposition reported by Satoshi Hashimoto and Hideki Matsuoka^[10] and a sol-gel technique investigated by Götttsche *et al.*^[2] who found a reduction in coloration efficiency of 35% with doping of 30% Ti atoms. However, there is no reports on the study of electrochromic TiO₂ doped WO₃ thin films prepared by anodizing of co-sputtered Ti/W thin film on conductive glass. The methods used to both preparation and characterization of the obtained thin films in this chapter have already been presented in Chapter 2.

4.2 Results and discussion

4.2.1 *The anodization transient curves*

Figure 4.1 shows characteristic anodizing transient current curves of pure tungsten (W) and Ti/W (nominal 13% Ti) thin films. The anodization voltage is determined after a series of experiments of anodizing under different voltages. At first time, as analogues to anodizing in aqueous solution under 40 V, the film is broken quickly and it is difficult to obtain an entire film on the substrate. After that, 20 V and 10 V were tried and it was found that the film anodized under 10 V has the best integrity. The anodization time is determined by observing the change of the film transparency during anodization from opaque with metallic surface to semi-transparency. The point at which the film is broken obviously or the current is increased suddenly is the limit of the anodization time and this phenomenon is usually observed after anodizing for 40-45 min under 10 V. Finally, 40 min is set for the anodization time. From figure 4.1, the initial current decay time starts after 48 s and 36 s for pure W and Ti/W thin film respectively, which is during the potential sweep process from 0 V to 10 V at 0.05 V s^{-1} . Before these decay points, the increased current density is caused by increasing voltage. At a certain point, the fast growth of a high resistance oxide barrier layer leads to the decay of the current density.^[11] Finally, the current density reaches a steady state at the end of the sweep potential with a fixed value at 10 V. This plateau is caused by the competition between the electrical oxidation

rate at metal/oxide interface and chemical dissolution rate at oxide/electrolyte interface.^[12]

Through comparison of the curves shown in Figure 4.1 it can be seen that the addition of titanium atoms leads to decrease of oxide growth energy. This is concluded from the turning potential in Figure 4.1 which is 0.6 V ahead relative to the oxidation of pure W film. Accordingly, a further observation and contrast can be found in that the anodizing current density of Ti/W thin film at the steady state is higher than that of pure W, revealing a faster dissolution/oxidation rate achieved for anodizing Ti/W film. The higher oxidation rate is attributed to the doped titanium atoms.^[13] Otherwise, the faster dissolution rate acts as indirect evidence for the higher porosity observed later in SEM images (Figure 4.4).

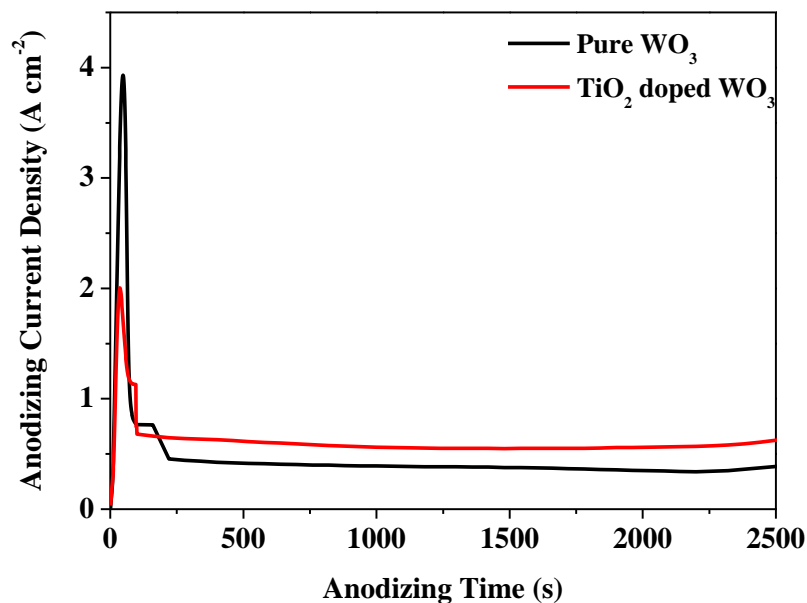


Figure 4.1 Characteristic anodization profiles of pure W and Ti/W thin film in 0.3 M NH₄F solution dissolved in ethylene glycol/DI water solution (volume ratio of 50:2). The anodize potential was increased from 0 V to 10 V at 50 mVs⁻¹ and fixed at 10 V for 40 minutes.

4.2.2 Morphology observation and corresponding elemental distribution

analysis

After anodization the elemental distribution in the film was analyzed by using SEM-EDS which revealed that the atomic proportion of titanium atoms in TiO_2 doped WO_3 thin film is 10 at.% without consideration of oxygen atoms. This atomic ratio of Ti/W is decreased compared with the 13 at. % in the co-sputtered Ti/W film. The reduction can be explained by the higher current density observed during the anodization of Ti/W thin film than its pure W counterpart during the steady state part at the end of the transients (Figure 4.1). This implies that the chemical dissolution rate of TiO_2 is faster than that of WO_3 under the same anodizing conditions, hence leading to the decrease of titanium content in the obtained TiO_2 doped WO_3 thin film. This phenomenon is also observed in the later works by anodizing in aqueous solutions in Chapter 5. In neither case did annealing alter the Ti/W atomic ratio.

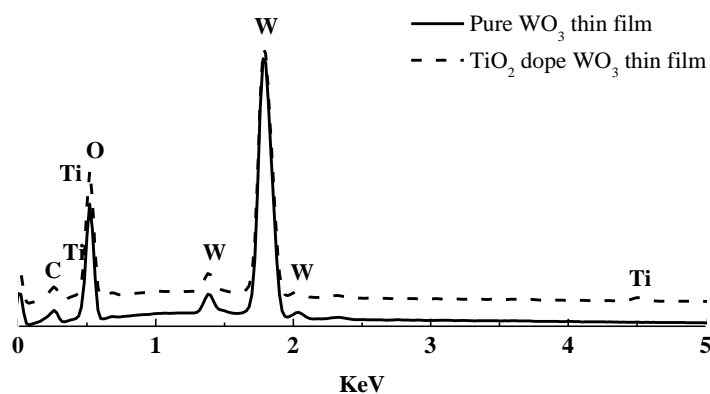
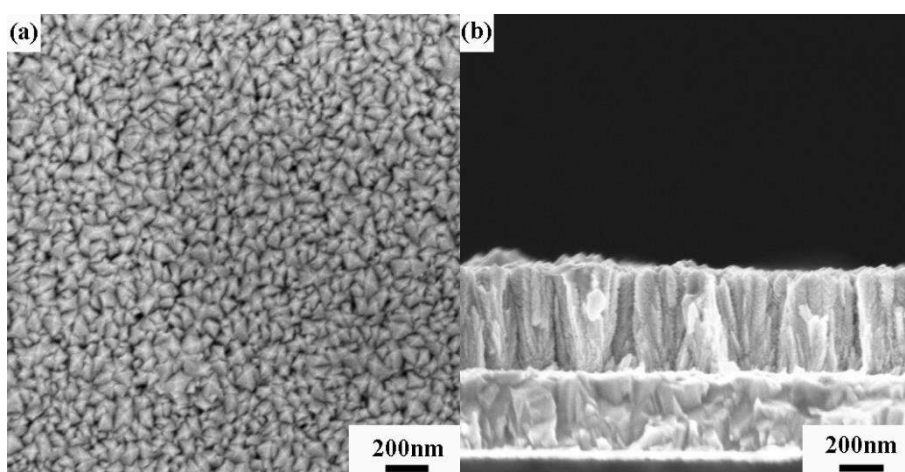


Figure 4.2 elemental distributions of pure WO_3 film and TiO_2 doped WO_3 film detected by SEM-EDS. Accordingly the titanium contributes 10 at.% of the

metallic component.

SEM images were used to compare the morphologies of the two films. Figures 4.3a and 4.3b display the top and cross section views of an as sputtered W thin film. Its top view shows octahedral morphology and its corresponding cross sections appear arrow shape, which are stacked compactly and aligned vertically with good adhesion on the FTO surface. The thickness of the sputtered thin film is around 450nm. The morphology and thickness of sputtered Ti/W thin film was shown in Figure 4.3 (c) and (d). It's found that there is no obvious difference on its octahedral structure observed from its top view. However, those arrows, observed from the cross section of pure W, become indistinct as shown in the cross section of Ti/W thin film. This implies the interruption of titanium on the array of tungsten atoms. The thickness of the Ti/W thin film is around 450 nm as well under the careful control of sputtering conditions.



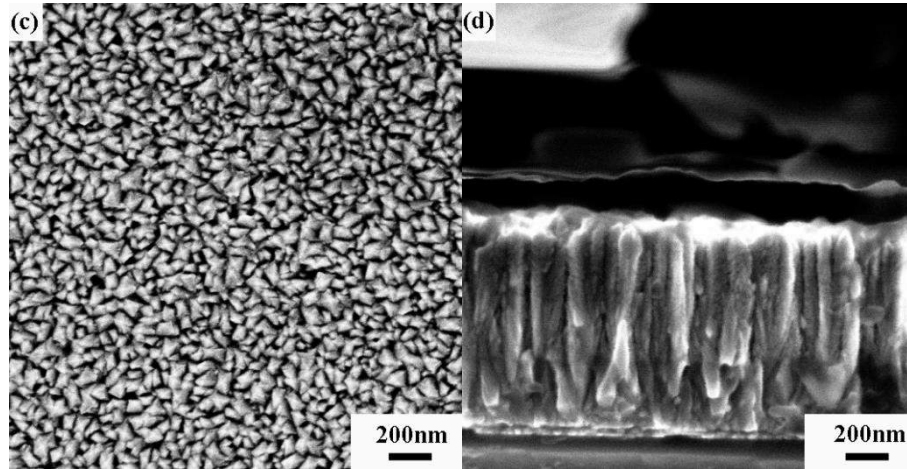


Figure 4.3 SEM images of (a) top and (b) cross section view for sputtered pure W on conductive FTO glass and likewise (c), (d) for the co-sputtered Ti/W.

After anodizing and heat treatment, porous structures are formed for both pure WO_3 and TiO_2 doped WO_3 thin films (Figure 4.4). The statistical average diameters of all pores for both WO_3 and TiO_2 doped WO_3 thin film are around 45nm; based on measuring 100 pores from the respected SEM images. However, the film with TiO_2 exhibits better integrity than the pure WO_3 thin film which contains obvious cracks with average dimensions of approximately 100 nm \times 600 nm. Furthermore, the cross section of pure WO_3 in Figure 4.4c shows randomly stacked short nano-column that are either solid or hollow inside. On the contrary, the film with TiO_2 in Figure 4.4d exhibits honeycombed structure. The pores connected with each other creating spacious channels as shown in Figure 4.4e. The formation of convenient channels in TiO_2 doped WO_3 thin film are expected to be convenient for charges transport and diffusion. Meanwhile, this honeycombed structure also provides large surface areas for ions insertion.

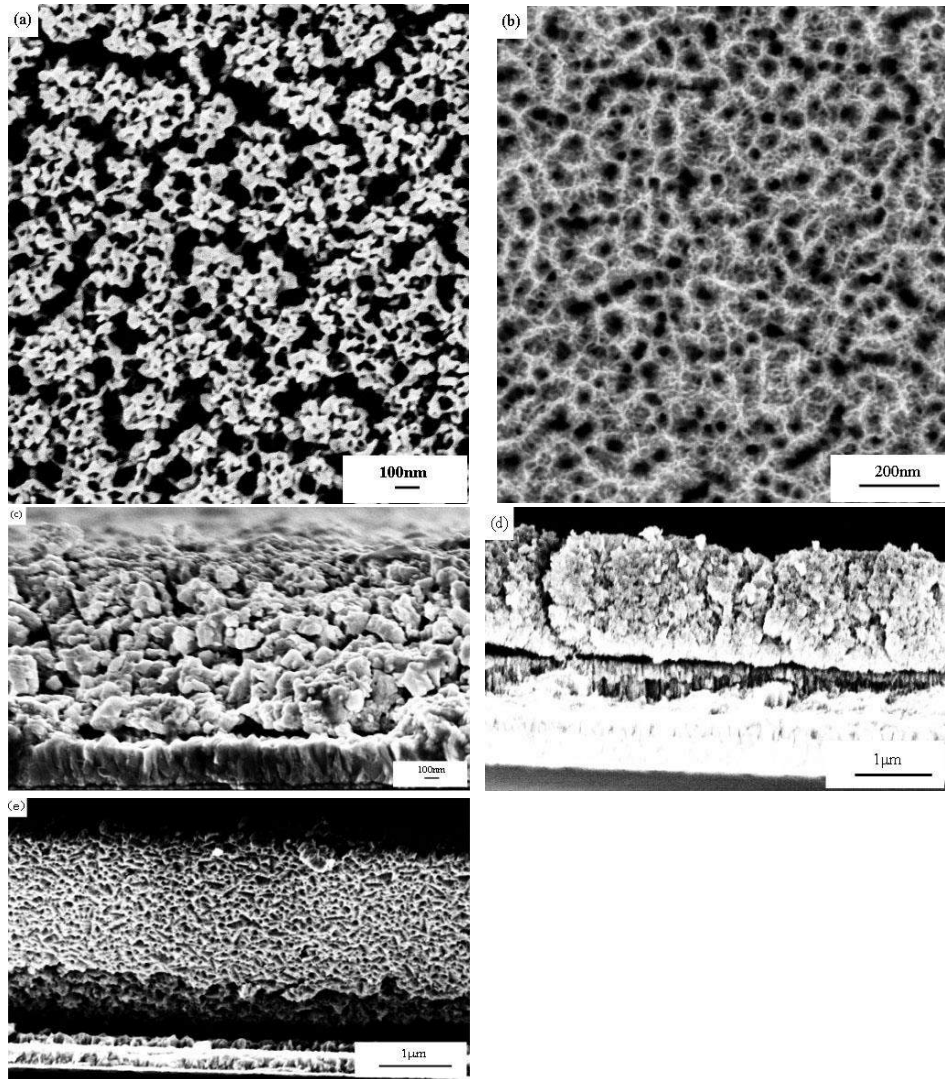
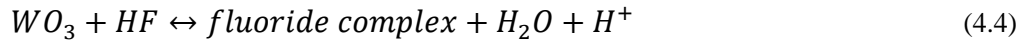
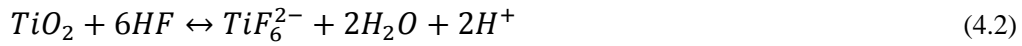


Figure 4.4 SEM images of films formed by anodization (a) Pure WO_3 thin film top view; (b) TiO_2 doped WO_3 (10 at.% Ti) thin film top view; (c) Pure WO_3 thin film top view cross section; (d) TiO_2 doped WO_3 thin film cross section; (e) TiO_2 doped WO_3 thin film bottom view. All these anodized film images were captured after annealing at 450°C for 3 hours.

Based on the literature, under high-field conditions, ethylene glycol can be oxidized in a series of steps to CO_2 :^[14]



In addition, because of the 2% water content of the ethylene glycol solution, a conventional oxidation and dissolution processes will also exist:^[15-17]

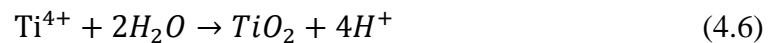
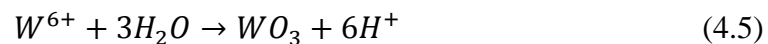


The use of ethylene glycol in this chapter is with expectation of obtaining nanotube structure as reported for growth of nanotube TiO₂. From the literature on anodic growth of TiO₂ nanotubes, it can be found that the viscosity of the electrolyte has a direct impact on diffusion of reactants and products to and from the titania nanotubes surface.^[13] The viscosity of ethylene glycol is 0.016 Pa s at 25 °C which is less viscous compared to glycerol and results in a lower diffusion resistance. Therefore compared with aqueous solutions, ethylene glycol-based electrolytes can slow down the dissolution rate of the formed oxides to form tubes. Furthermore ethylene glycol is a protic solvent which can solvate F⁻ strongly via hydrogen bonding and from the solvent-Berg model it is known that the solvent molecules immediately adjacent to the ion are rigidly bound to it and thus these move together as a kinetic unit. Consequently, the conductivity of HF in the ethylene glycol-water mixture is limited by the solvent molecule mobility, hence the dissolution rate of the formed oxides in this ethylene glycol-water mixture is slower than in aqueous solution. Conversely, relative to other organic solvents with high viscosity, the oxygen produced by water splitting can reach metal/oxide interface quickly to aid oxide formation.^[13]

18-19]

However, instead of separate nanotube, pores with very short tube-like channels are observed from figure 4.4(e). These structure differences between WO_3 and TiO_2 could be ascribed to the different physical and chemical properties between tungsten and titanium. Even though, in general, three stages are involved in the process of either pure titanium or pure tungsten anodization and the respective corresponding chemical reactions at each stage are introduced below:

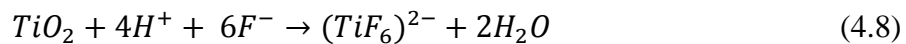
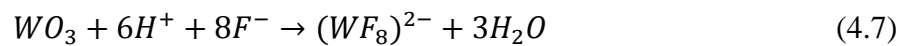
In the first stage of anodization, small oxide pits will start to form randomly on either the titanium or tungsten surface, due to a hydrolysis process from the presence of the water content in the solution. The field-assisted migration of O^{2-} through either the titanium or tungsten surface towards the respective Ti/TiO_2 and W/WO_3 interface results in further growth of the oxide pits under increased voltage until the formation of a compact oxide layer on the surface. The chemical reactions occurring are:^[20-21]



From these equations it can be seen that less O^{2-} is required to migrate to the surface for form 1 mole of TiO_2 than to form 1 mole of WO_3 , therefore under the same anodization condition, i.e. the same electric field strength, the TiO_2 formation rate should be faster than that of the WO_3 and this is can be confirmed by observing the films' color changes during the anodization process. This color change comes from constructive interference between the light reflected from

the surface of the oxide layer and the light reflected from the metal surface. This color change which is observed when anodizing W/Ti thin film is several seconds ahead of that happened when anodizing pure W thin film. In addition, from the anodization current density-time curves in Figure 4.1, it also can be found that when anodizing the Ti/W thin film the current density decreases sooner than is the case for the pure W thin film, implying a faster growth rate of the oxide on the Ti/W than that on pure W.

In the second stage the formation of tungsten fluorocomplex ions that readily dissolve into solution lead to the enlargement and deepen these pores and voids. The formation and dissolution of titanium fluorocomplex ions also occurs once there is the formation of TiO₂ layer. The chemical reactions occurring are:^[22]



At the final stage, a balance between the oxidation of metal and dissolution of oxide rate will be built up as shown in Figure 4.1, with anodization current density adopting an almost constant value. Again during this stage it found that the current density for anodization of Ti/W thin film is higher than that for pure W thin film, implying a higher rate for both the oxidation of Ti/W thin film and dissolution of its oxide.

The end result of the mechanism described above is that the honey comb morphology displayed in Figure 4.4(b), (d) and (e) is likely caused by both

oxidation and dissolution rates being higher at the points where titanium atoms are located within the tungsten matrix. Meanwhile, the local conductivity in electrolyte is also higher at the points where titanium atoms are positioned from tungsten matrix according to their respective equations. It can be seen that firstly, either oxidation of titanium or tungsten will produce H^+ , however, the oxidation rate of titanium is faster than that of tungsten resulting in faster increase of local conductivity at the position where the titanium exists. Secondly, the amount of consumed H^+ for dissolution of titanium oxide is less than that of tungsten oxide indicating a larger magnitude of decrease of local conductivity at the position where the tungsten oxide formed. Therefore, a localized imbalance between oxidation and dissolution rates will be built up that might lead to the connection of adjacent pores instead of the compact wall surface shown by cross section of pure WO_3 thin film. So the observed steady state during the anodization of Ti/W thin film could be an average effect.

4.2.3 Structural analysis

Figure 4.5 shows XRD patterns of the thin films with and without titanium as sputtered, after anodizing and after annealing at $450^\circ C$ for 3h. The structure of pure W and Ti/W thin film are cubic identified from their XRD peaks and there are no traces of titanium characteristic peaks in the XRD result of Ti/W film. After anodizing, the XRD pattern remains the same except a sharp decreased

intensity of the main peaks belonging to pure tungsten, implying that after anodization there is still a small amount of non-oxide tungsten residues left in the matrix. Before the heat treatment, there are no peaks that can be assigned to the oxides, meaning that the as anodized films have an amorphous structure.

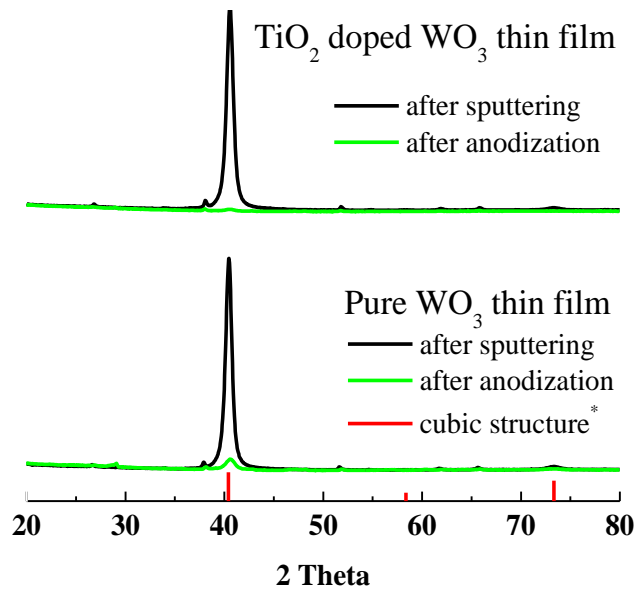


Figure 4.5 Comparison of the XRD results before and after anodization of W thin films with and without titanium. (Cubic structure* is indexed from ICDD 00-001-1204)

However, after annealing the anodized WO_3 and TiO_2 doped WO_3 thin film become crystalline with monoclinic structure that matches the ICDD card 00-005-0364 (Figure 4.6)^[23] and the lattice spacing of (001), (020) and (200) planes are 0.384 nm, 0.375 nm and 0.365 nm respectively for pure WO_3 thin film.

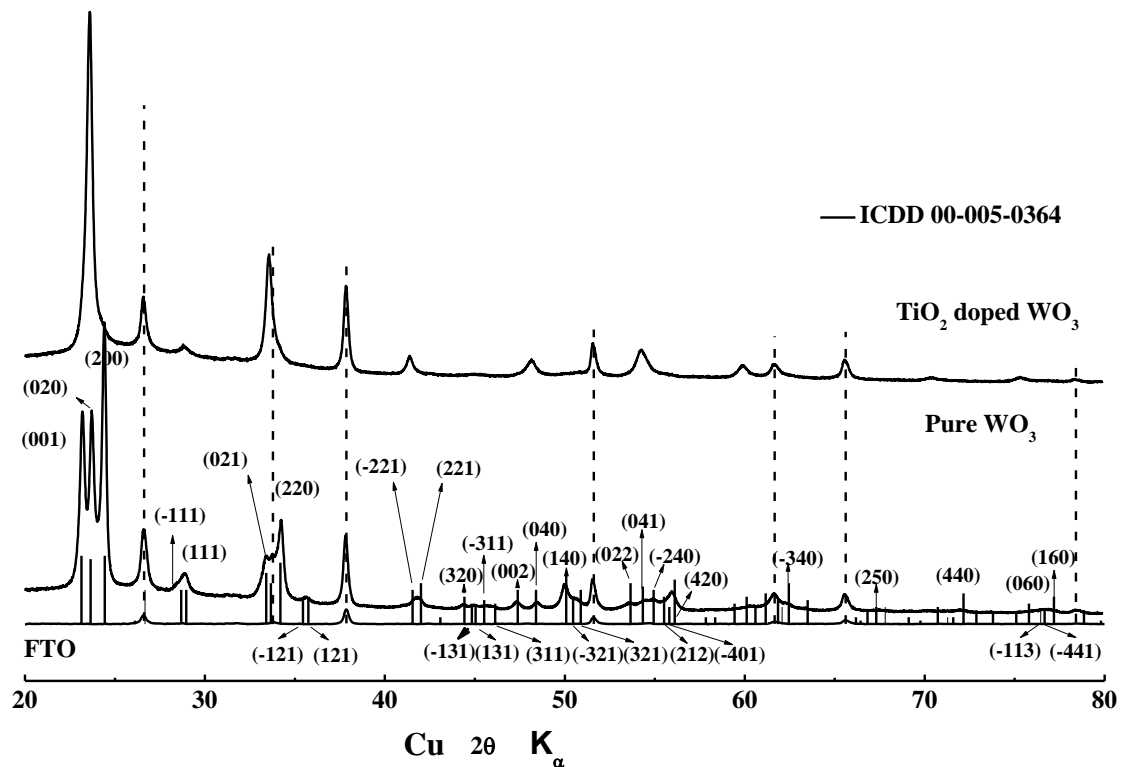


Figure 4.6 Comparison of the XRD results of pure WO_3 and TiO_2 doped WO_3 thin film formed by anodization after annealing at 450°C for 3h. The peaks passed through by dash lines belong to FTO substrate.

As introduced in Section 1.3.2, the structures of the single crystals of pure WO_3 are transformed following a sequence of monoclinic \rightarrow triclinic \rightarrow monoclinic \rightarrow orthorhombic \rightarrow tetragonal with the temperature from -189°C to 900°C ^[24] Therefore, the annealing temperature plays important role in forming WO_3 structures and the monoclinic structure of WO_3 after heat treatment at 450°C seen in the present work is also reported by Sadek *et al.*^[7] and Judeinstein *et al.*^[25] when they studied the influence of annealing on the phase transformations of WO_3 at this temperature.

From comparing the XRD spectrum, it can be seen that, after doping, the peaks at 50.030°, 50.737° and 55.925° in the XRD spectrum of pure WO₃ thin film are disappear, which possibly indicates an increase of symmetry. According to the reported literature, higher symmetry may result from static disorder, which can be ascribed to the presence of clusters of edge-sharing octahedral randomly distributed in the lattice.^[26] Indeed, the tendency to form edge-sharing octahedral is found in oxygen deficient tungsten oxides phase and the titanium substitution for tungsten will induce the same effect of oxygen substoichiometry.^[27]

The peaks shift toward lower angle, observed in the XRD spectrum of titanium doped WO₃ thin film, results in a minor increase of d-values. This minor shift is indicative of mild lattice strain that possibly arises from the differences between ionic radius of Ti⁺⁴ and W⁺⁶, the radius of which is 132 pm and 130 pm respectively.

Table 4.1 List of peak positions for pure WO₃ and TiO₂ doped WO₃ films

| | (001) | (020) | (200) | (111) | (221) | (040) | (-240) | (-222) |
|--|-------|-------|-------|-------|-------|-------|--------|--------|
| Monoclinic | 23.1 | 23.6 | 24.4 | 29.0 | 42.0 | 48.4 | 54.9 | 60.6 |
| Pure WO ₃ | 23.1 | 23.7 | 24.4 | 28.9 | 41.8 | 48.4 | 54.8 | 60.1 |
| TiO ₂ doped WO ₃ | -- | 23.5 | 24.2 | 28.8 | 41.4 | 48.2 | 54.2 | 59.9 |
| $\Delta 2\theta$ | -- | 0.2 | 0.2 | 0.1 | 0.4 | 0.2 | 0.6 | 0.2 |

$$\Delta 2\theta = 2 \theta_{(Pure\ WO_3)} - 2 \theta_{(TiO_2\ doped\ WO_3)}$$

The values of 2θ for Monoclinic in above table are from ICDD card 00-005-0364

A further analyzing on the structure of the annealed WO_3 thin film reveals a lattice spacing of 3.659\AA of (200) planes, a preference perpendicular to the electrode's surface is commonly observed in electrochemistry formed films. However, through comparison, it can be seen that the incorporation of TiO_2 leads to reduce the crystallinity as seen from the decreased intensities of characteristic peaks at (001) and (200) resulting in difficulties in resolving these two into separate peaks from the peak of (020) as observed in pure WO_3 thin film. The disorder induced by the addition of TiO_2 was also found by Patil *et al.* when they studied on TiO_2 doped WO_3 thin film by spray deposition.^[28]

Figure 4.7 shows HRTEM images for pure WO_3 and TiO_2 doped WO_3 thin films analysis of which is agreement with the conclusions summarized from the XRD patterns. From Figure 4.7a, the calculated lattice spacing of pure WO_3 thin film is 0.365 nm , which is exactly the same with the one detected by the XRD, with the corresponding diffraction pattern being observed clearly in Figure 4.7b. Additionally, the HRTEM diffraction patterns showed in Figure 4.7d displays poly-crystalline features and the corresponding lattice spacing cannot be resolved from Figure 4.7c due to the less crystallinity. Thus it is not possible to deduce from the XRD and HRTEM data if the Ti^{4+} ions replace W^{6+} ions in the WO_3 lattice, which is in contrast to the case of the hydrothermally produced

films in Chapter 3 where this conclusion could be drawn. However, as the XRD pattern in Figure 4.6 still does not show any peaks that can be assigned to TiO_2 (e.g. rutile or anatase) but left shifts of peaks, it is likely that lattice substitution still occurs.

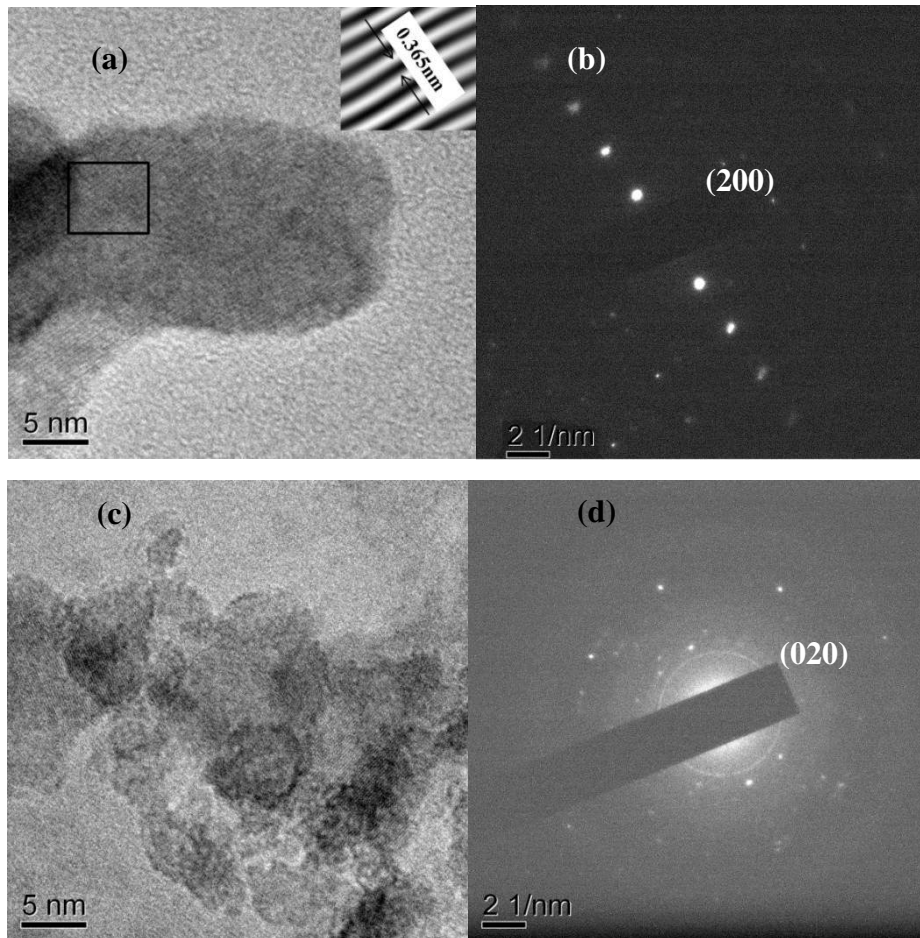


Figure 4.7 High-resolution TEM image of (a) Pure WO_3 thin film formed by anodization after scratching from FTO substrate and being dispersed in ethanol on to a Cu grid. The inset is the region outlined by a square after performing a reversed Fourier transform; (b) diffraction image corresponds to (a); (c) TiO_2 doped WO_3 thin film after the same process as pure WO_3 and (d) diffraction image corresponding to (c).

4.3.4 Raman spectroscopy

In order to probe TiO₂ dopants in the TiO₂ doped WO₃ thin film, the Raman spectroscopy technique was adopted. The Raman spectra in the range of 150cm⁻¹-1050cm⁻¹ at room temperature of WO₃ thin films with and without TiO₂ are presented in Figure 4.8. The broad peak, from 600 cm⁻¹ to 900 cm⁻¹, with two sharp peaks located at 811 cm⁻¹ and 720 cm⁻¹ for the pure film are characteristic Raman peaks of crystalline WO₃ with monoclinic structure for the sample annealed at 450°C, corresponding to its W-O stretching (ν) mode in WO₆ octahedral units.^[23-26] In addition, two peaks located at 276 cm⁻¹ and 332 cm⁻¹ for the annealed film at 450°C are assigned to the O-W-O bending (δ) vibration, which are also signature peaks reflecting a monoclinic structure of this pure WO₃ film.^[29-33] These observations are consistent with the XRD result discussed in Section 4.2.3 which proves the obtained films have monoclinic structures.

Through comparison of the Raman spectrum of TiO₂ doped WO₃ thin film with that of the pure WO₃ thin film (Figure 4.8), it can be seen that the W-O stretching (ν) modes have blue shifted to 799 cm⁻¹ and 702 cm⁻¹. This migration towards lower frequency (lower energy) is consistent with the appearance of oxides with lower oxidation state, i.e. substitution of W⁶⁺ by Ti⁴⁺. In addition, the observed broadening of the characteristic Raman peaks for TiO₂ doped WO₃ thin film reflects increase of structure disorder. This effect, induced by the incorporation of titanium atoms, is also consistent with a transformation from

corner to edge sharing octahedral ascribed to the deficiency of oxygen in the lattice.^[34] This evidence is consistent with the suggestions in the XRD analysis (Section 4.2.3).

Additionally, an obvious peak aligned at around 993 cm^{-1} can be found in the Raman spectra of TiO_2 doped WO_3 thin film, but not observed in pure WO_3 film, which can be assigned to representing stretching modes involving $\text{W}=\text{O}$ terminal oxygen atoms.^[35] The appearance of $\text{W}=\text{O}$ stretching mode suggests a decrease in grain-size since the addition of titanium atoms can inhibit the mobility of grain boundaries.^[36] Finally it should be noted that there are no distinct peaks assigned to TiO_2 observed for TiO_2 doped WO_3 thin film in Figure 4.8.

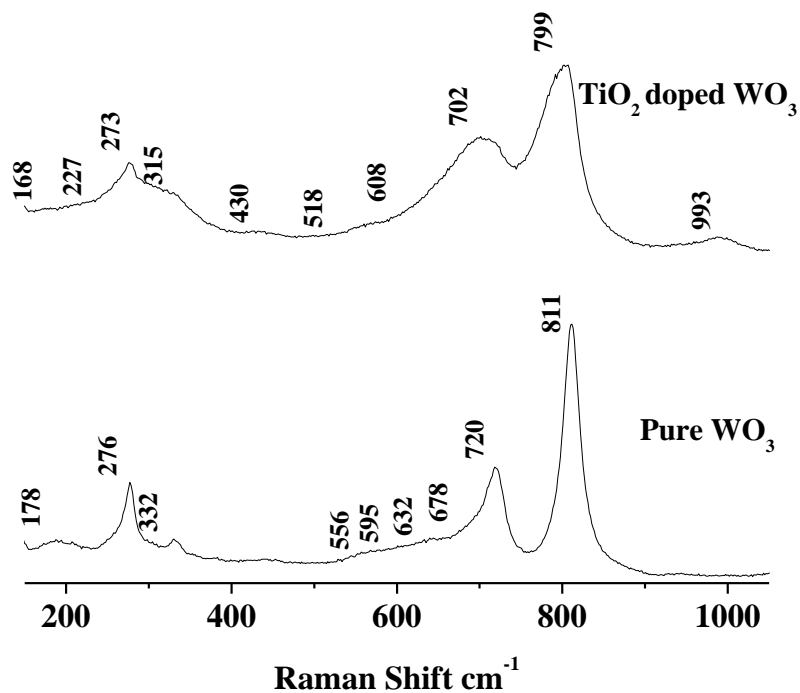


Figure 4.8 Raman spectra of Pure WO_3 thin film and TiO_2 doped WO_3 thin film

4.2.5 XPS investigation

Figure 4.9 depicts the XPS spectra for the pure WO_3 and TiO_2 doped WO_3 thin films. The identified peaks with strong peak intensities displayed in Figure 4.9(a), (b) and (c) are ascribed to W 4f, Ti 2p and O 1s orbits separately. According to the statistical calculation, the quantity of titanium atoms on the surface of this TiO_2 doped WO_3 thin film is around 12 at.%, which is 2% higher than the conclusion from the SEM-EDS, but closer to the 13 at.% expected from the sputtering conditions. By considering that XPS measurement only reflects surface information, the elements distribution analyzed by SEM-EDS technique is closer to bulk situations. From analyzing, it can be seen that the peaks in Figure 4.9(a), located at 35.93 eV and 38.03 eV (with distance of 2.1 eV), are attributed to spin-orbit splitting of W 4f and confirm tungsten with a valence state of six in both of the pure WO_3 and TiO_2 doped WO_3 thin films.^[37] In the meantime, the peak of O1s, positioned at around 530.8 eV in Figure 4.9(b) is contributed by the oxygen bonded with W^{6+} and there is no peak shift within an allowable error range between these two films.^[38]

A further observation finds that the full peak width at half maximum (FWHM) and peak intensity of TiO_2 doped WO_3 thin film are broader and lower respectively than in the pure WO_3 film. This is caused by the appearance of weak Ti 3p peaks found from the de-convoluted components embedded in the peak of W 4f.^[39] Otherwise, the characteristic peak of Ti 2p is captured at the

position of 459.13 eV and 464.93 eV, which is ascribed to O-Ti⁴⁺-O, [40] confirming the presence of Ti⁴⁺ in the-synthesized TiO₂ doped WO₃ thin films.

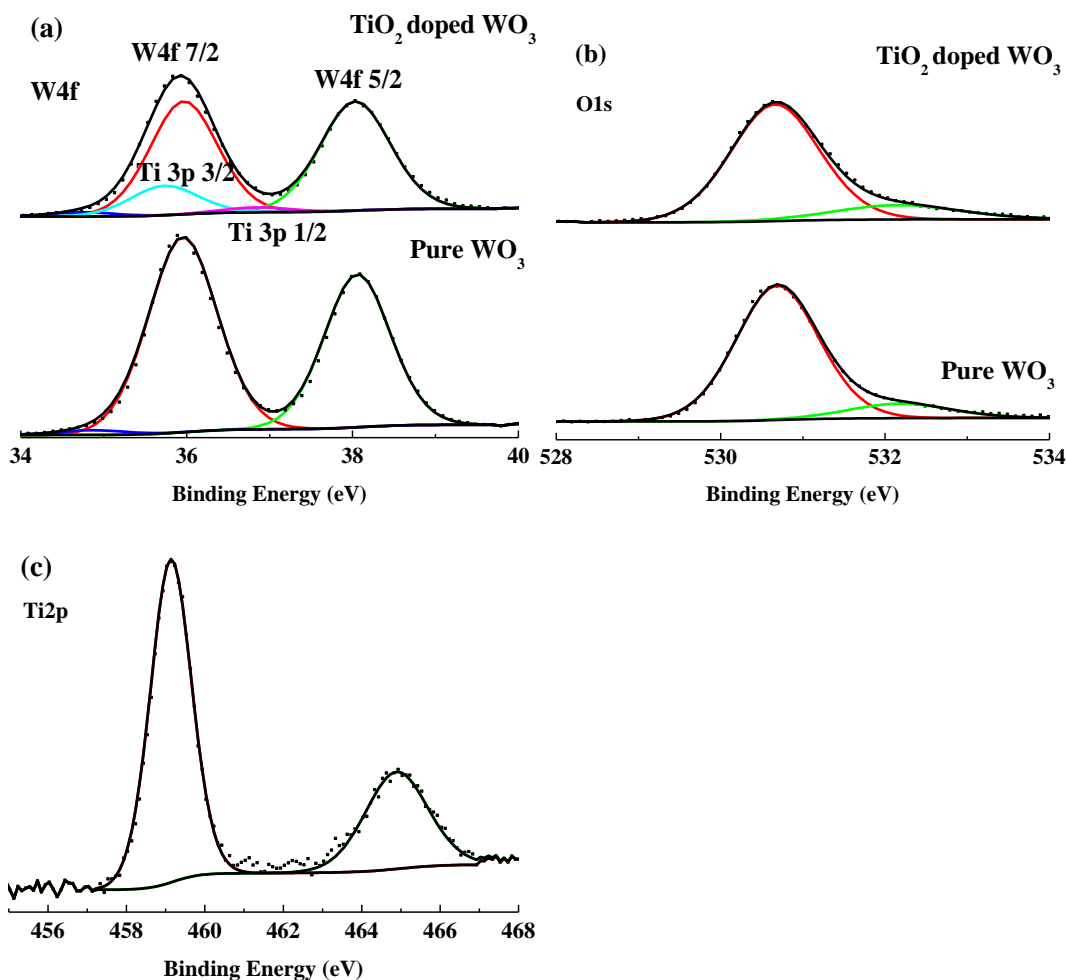


Figure 4.9 XPS spectra of the orbits of (a) W 4f, (b) O 1s and (c) Ti 2p.

4.2.6 Cyclic Voltammetry

Figure 4.10 shows the cyclic voltammograms (CV) of the pure WO₃ and TiO₂ doped WO₃ thin films at their 1st, 500th and 1000th cycle. Integration of the CV current density yields the inserted charge density (q_{in} (mC cm⁻²)) values

displayed in Table 4.2. It can be seen that for the first cycle the q_{in} of TiO₂ doped WO₃ is ca.75mC cm⁻² which is about twice that of the 30mC cm⁻² of the pure WO₃. This indicates that the structure of TiO₂ doped WO₃ thin film exhibits better ion accommodation capacity due to either its more open morphology or lower crystallinity. Besides, the calculated reversibility (q_{in}/q_{out}) of TiO₂ doped WO₃ thin film is 98%, higher than 87% of pure WO₃ thin film. The benefit of improved reversibility of the thin film ascribed to the addition of TiO₂ is in agreement with the reported studies in which titanium oxide was mixed into tungsten trioxide matrix directly.^[41]

Table 4.2 Charge density list of pure WO₃ and TiO₂ doped WO₃ thin films for their first cycle in CV test

| | Pure WO ₃ thin film | WO ₃ /TiO ₂ thin film |
|-------------------------------|--------------------------------|---|
| q_{in} mC cm ⁻² | 30 | 75 |
| q_{out} mC cm ⁻² | 27 | 73 |
| q_{out} / q_{in} | 0.98 | 0.87 |
| $(q_{in} - q_{out}) / q_{in}$ | 13% | 2% |

q_{in} = inserted charge density; q_{out} - extracted charge density; q_{out}/q_{in} = reversibility

In the present case, this higher reversibility likely resulted from the more porous morphology observed in the TiO₂ doped WO₃ mixed film. A comparison between the SEM images in Figures 4.4(c) and (d) yields that the TiO₂ doped WO₃ thin film provides more spacious channels for the charge transport due to

the pores also found at its base. Meanwhile it is also believed that these channels provide larger surface area for more charge occupation leading to a deep blue induced by the reversible redox reaction between W^{5+} and W^{6+} and convenient passages for extraction of charges in time, hence exhibiting a better reversibility. In addition, a further analyze of Figure 4.10 indicates the better cyclic stability of TiO_2 doped WO_3 thin film over that of the pure WO_3 thin film. Although after 500 cycles the profile of the CV curve for TiO_2 doped WO_3 thin film is slightly degraded there is not as significant change in its shape. Whereas, after the same number of cycles, the area enclosed by the CV curve of the pure WO_3 thin film is reduced greatly, implying that the effective places for the charge insertions are blocked, possibly due to narrower channels leading to the accumulation of charges.

However, as compared to the hydrothermally produced TiO_2 doped WO_3 thin film in chapter 3, the degradation of the thin film produced by anodization method is worse. This is possibly due to the disadvantage of using a physical method for the production of the initial metallic thin films rather than chemical deposition; the latter can provide better adhesion between the thin film and substrate.

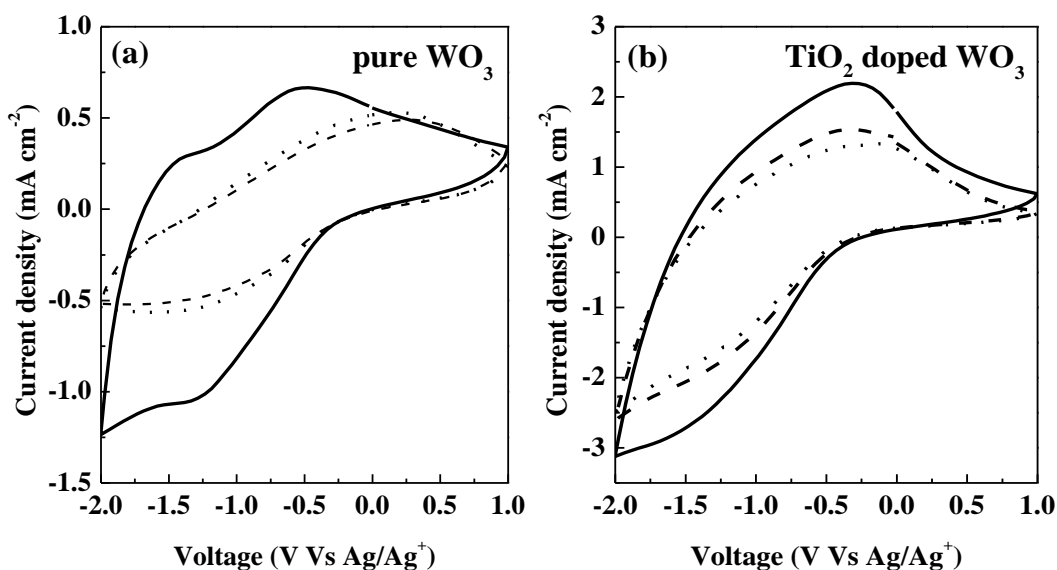


Figure 4.10 Cyclic voltammetry curves of (a) Pure WO_3 thin film and (b) TiO_2 doped WO_3 thin film. The CV is conducted in 1M LiClO_4 dissolved in propylene carbonate solutions with a sweep rate of 50mV s^{-1} from -2V to 1V vs. Ag/Ag^+ . The solid line “—” denotes the first cycle; dash line “-----” denotes the 500th cycle and dotted line “.....”denotes the 1000th cycle.

Figure 4.11 shows the insertion charge densities at selected numbers cycles.

Through comparison, it can be seen that the TiO_2 doped WO_3 thin film exhibits larger capacity than the pure WO_3 film, which is believed to be ascribed to the honey comb morphology of the former. Furthermore, the decrease in the amount of intercalated ions per area from the first to the 500th cycle is 50% for pure WO_3 thin film, which is twice that for the TiO_2 doped WO_3 thin film. This result is agreement with the observed change of the CV profiles in Figure 4.10. However, the degradation phenomenon observed in this TiO_2 doped WO_3 thin film is due to a small amount of detachment of the thin film from FTO substrate. This drawback is believed to originate from the sputtering method which may not have provided good linkage of the W or Ti/W atoms with the FTO substrate.

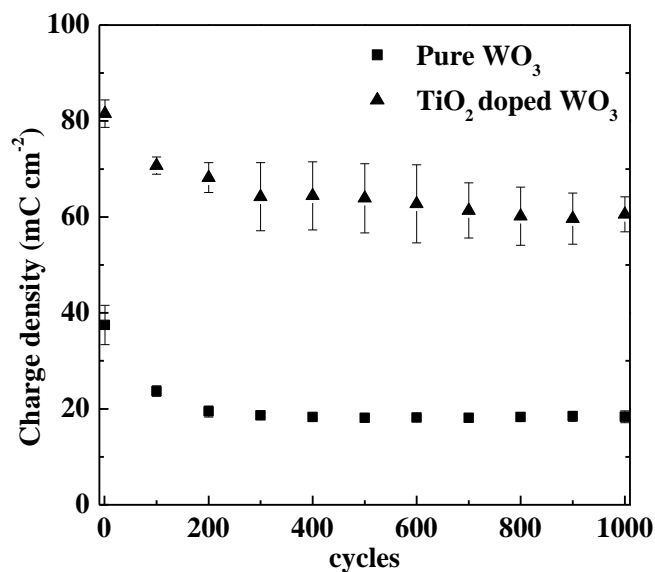


Figure 4.11 Comparison of inserted ion charge density at selected cycle numbers corresponding to the cyclic voltammetry curves of pure WO₃ and TiO₂ doped WO₃ thin film.

4.2.7 Electrochromic properties

Figure 4.12 shows chronoamperometry curves of the pure WO₃ and TiO₂ doped WO₃ thin films being charged and discharged between -1 V and 1 V vs. Ag/Ag⁺ for 50 s and 150 s respectively. The reversibility calculated by q_e/q_i are 77.8% and 95% for pure WO₃ and TiO₂ doped WO₃ thin films respectively (q_e denotes the amounts of extracted ions at 1 V after 150 s; q_i represents the amounts of inserted ions at -1V after 50s). This is in good agreement with the calculation from Figure 4.10, based on the cyclic voltammograms.

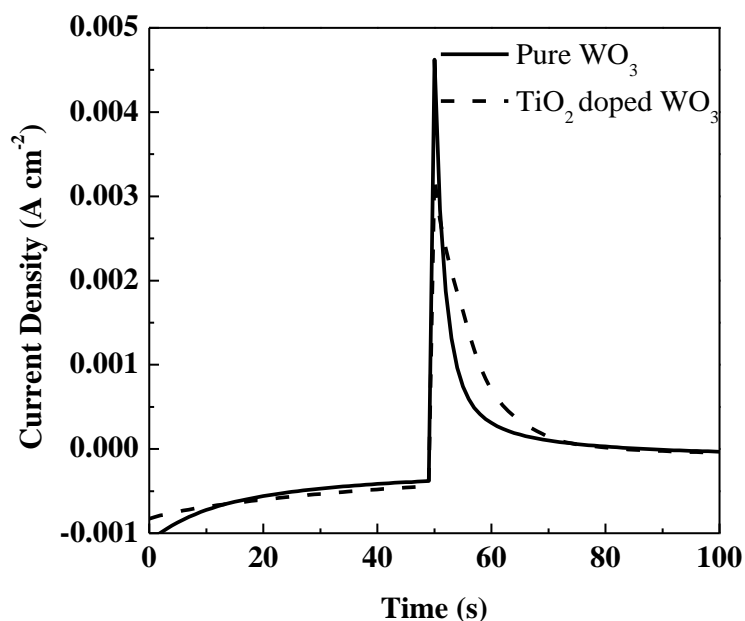


Figure 4.12 Chronoamperometry curves of pure WO_3 and TiO_2 doped WO_3 thin films. The test is conducted by providing alternative potentials between -1 V and 1 V vs. Ag/Ag^+ (0.1M AgNO_3 /0.01M TBPA in acetonitrile) for 50 s and 150 s respectively in 1 M LiClO_4 dissolved in propylene carbonate solutions.

In order to record the corresponding effect on the light absorption by these electrochromic thin films as the applied potential is changing from -1 V to 1 V vs. Ag/Ag^+ *in situ* UV-vis spectroscopy is conducted at the same time with the chronoamperometry measurement. This reveals the electrochromic properties as assessed by the coloration efficiency, which was previously defined in Equations 3.10 and 3.11.

From Figure 4.13, it can be seen that TiO_2 doped WO_3 thin film exhibits a larger light transmittance change (ΔT) of 57.6%/71.5%/68.7% at wavelengths of 550 nm/632.8 nm/800 nm than pure WO_3 which shows only 41.4%/57.3%/40.6% at the same wavelengths. The addition of ca. 10at.% TiO_2 has greatly improved the color contrast over a wide wavelength range, which is consistent with the

study result shown by Patil *et al.* adopting spray pyrolysis method and finding that the optical density was increased from 20% to 63% at 630nm after the doping concentration of TiO₂ varying from 13% to 38%^[28]. Therefore, it can be inferred that the presence of ca.10 at.% titanium atoms relative to tungsten in TiO₂ doped WO₃ thin film can achieve the purpose of improving light transmittance change range, providing a comfortable visual view at its bleach state on the one hand and good heat energy insulation in the colored one. Finally note that the ΔT of this TiO₂ doped WO₃ thin film produced by anodization is higher than that synthesized by hydrothermal method which is 68% at 632.8nm (Section 3.2.4). This comparison further proves the advantages of removing the compact inner layer found in the hydrothermally produced films discussed in Chapter 3.

In order to further assess its performance as a candidate for applications on “Smart Window” the electrochromic durability of the TiO₂ doped WO₃ thin film was characterized by running it through 500 cycles. From Figure 4.13 and 4.14 it can be seen that after 500 cycles the light modulation range of TiO₂ doped WO₃ thin film has a slight increase due to an enhanced transmittance in the bleach state implying the small amount of film detachment. However, this does not affect the coloration of TiO₂ doped WO₃ thin film under this condition. This means that the amount of the ions inserted into the film is still large enough for the film to reduce the light transmittance to almost zero at the wavelength of

800 nm (the import near IR region) even after 500 cycles. This slight detachment of the film can also be seen in the cyclic voltammetry tests (Section 4.2.6). Besides, the coloration efficiency of the film is not changed after running 500 cycles. All the calculated data are listed in Table 4.3

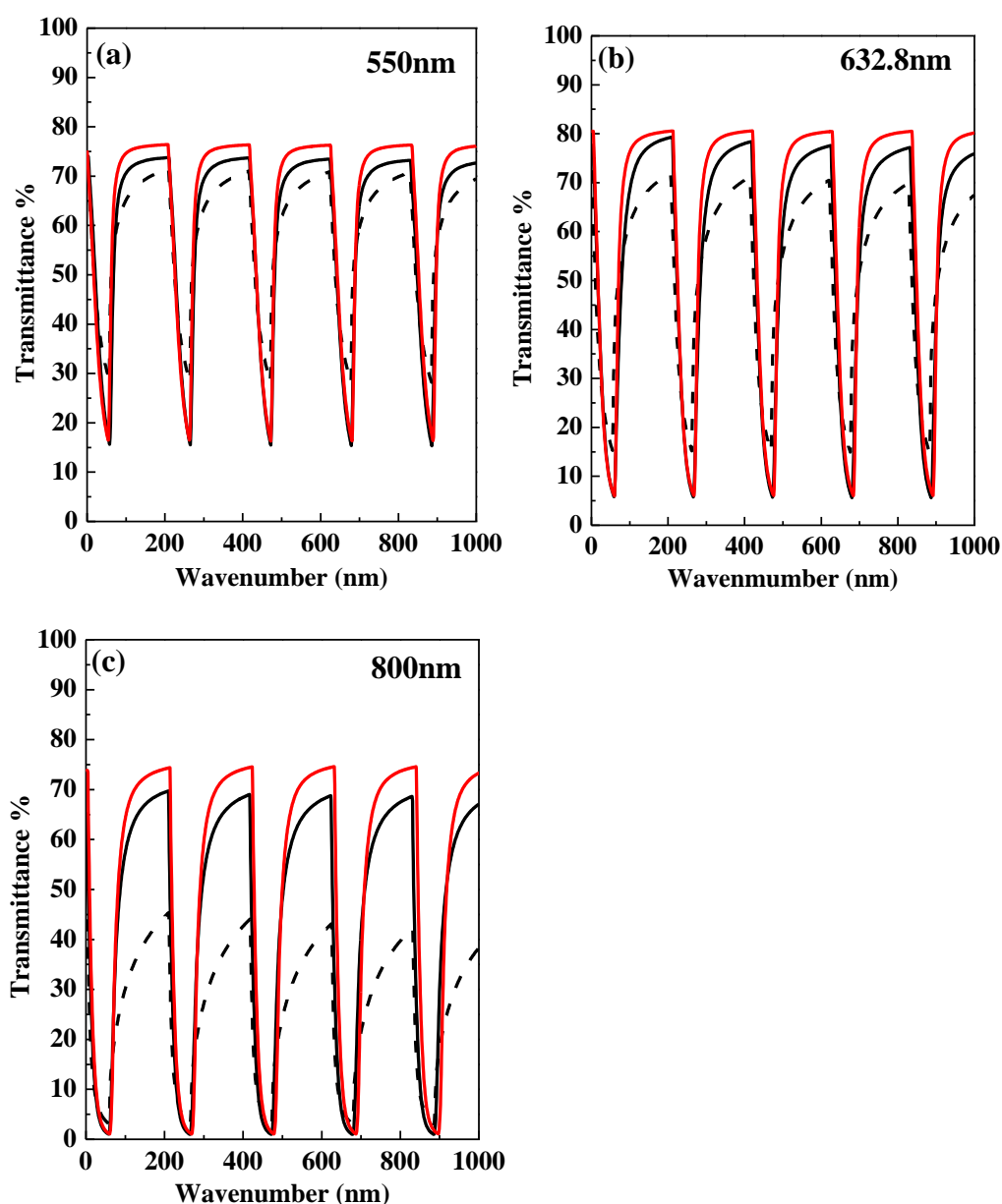


Figure 4.13 (a), (b) and (c) are *in-situ* UV-vis kinetic curves corresponding to Figure 4.12. The black and red solid line “—” represent $\Delta T\% \sim \lambda$ features of the TiO_2 doped WO_3 thin film at the first and the last five cycles of 500 cycles

respectively; the dash line “-----” represents pure WO₃ thin film at its first five cycles.

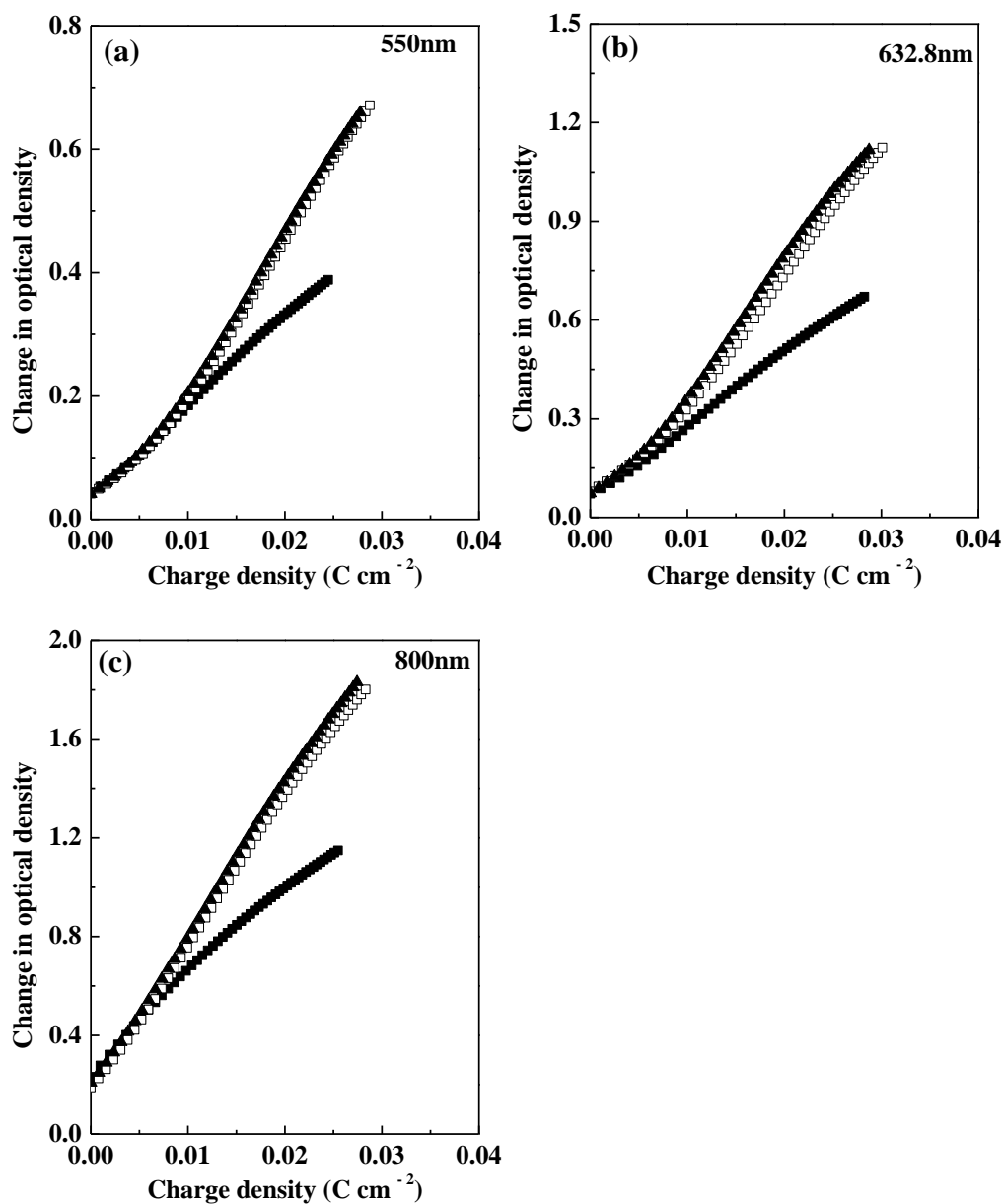


Figure 4.14 (a), (b) and (c) are the related coloration efficiency at different wavelengths. The filled square “■” represents the coloration efficiency of pure WO₃; empty square “□” for TiO₂ doped WO₃ at the 1st cycle and the filled triangular “▲” for TiO₂ doped WO₃ at the 500th cycle.

The coloration/bleaching time is defined as the time consumed to reverse the transmittance while the coloration (γ_c)/bleaching (γ_b) rate is the same as

elaborated in Chapter 4, Section 4.2.4. From Table 4.4, it can be seen that the coloration rate (γ_c) of WO_3/TiO_2 thin film is comparable with that of the pure WO_3 at wavelengths of 550 nm and 632.8 nm, but almost twice as fast in the import near infrared region at 800 nm. The bleaching rates of the WO_3/TiO_2 thin film (γ_b) are faster than the pure WO_3 film at all wavelengths, being more than three times faster at both 550 nm and 800 nm..

Comparing the coloration/bleach rate of the TiO_2 doped WO_3 thin films synthesized by hydrothermal method in Chapter 3 (H- WO_3/TiO_2) and anodization in this chapter (A- WO_3/TiO_2) respectively at 632.8nm, γ_c of H- WO_3/TiO_2 is $4.51\% \text{ s}^{-1}$, two times faster than A- WO_3/TiO_2 thin film. However, γ_b of H- WO_3/TiO_2 is only $0.77\% \text{ s}^{-1}$, comparable with that of the anodized pure WO_3 thin film in this chapter and three times slower than A- WO_3/TiO_2 thin film. These results are as expected, since on the one hand, the faster γ_c of H- WO_3/TiO_2 is caused by its larger top surface area, which can be quickly occupied and lead to faster transmittance change at the beginning. On the other hand, the slower γ_b of both H- WO_3/TiO_2 and anodized pure WO_3 thin film is induced by the compact under layer and non-porous base respectively. The porous channels in A- WO_3/TiO_2 thin film that goes through the whole film provide convenient channels for extraction of charges during the bleaching process and hence, greatly improving its bleach rate as discussed above. Even though, the bleaching is still to be incomplete as shown in figure 4.15. This

incomplete bleach is closely related to their electrochromic reversibility which is not 100% for both pure WO₃ thin film and the TiO₂ doped WO₃ thin film.

Table 4.3 List of optical and kinetic parameters for pure WO₃ and TiO₂ doped WO₃ thin films obtained from Figure 4.13 and 4.14 at wavelengths of 550, 632.8 and 800 nm.

| Wavelength nm | $\Delta T\%$ | | | CE (C cm ⁻²) ⁻¹ | | | Coloration/Bleach Time (s) | | |
|--|--------------|-------|------|---|-------|------|--|---|--|
| | 550 | 632.8 | 800 | 550 | 632.8 | 800 | 550 | 632.8 | 800 |
| pure WO ₃ | 41.4 | 57.3 | 40.6 | 13.1 | 22.7 | 45.3 | 41/ ^{α} 60/ ^{β} 31/ ^{λ} 5 | 38/ ^{α} 72/ ^{β} 41/ ^{λ} 9 | 24/ ^{α} 107/ ^{β} 72/ ^{λ} 24 |
| WO ₃ /TiO ₂ | 57.6 | 71.5 | 68.7 | 21.8 | 35.2 | 63.8 | 41/ ^{α} 28/ ^{β} 17/ ^{λ} 8 | 36/ ^{α} 50/ ^{β} 34/ ^{λ} 16 | 24/ ^{α} 61/ ^{β} 40/ ^{λ} 18 |
| ^a WO ₃ /TiO ₂ | 58.7 | 74.6 | 72.4 | 22.5 | 39.7 | 64.3 | 41/ ^{α} 23/ ^{β} 15/ ^{λ} 8 | 34/ ^{α} 31/ ^{β} 20/ ^{λ} 10 | 23/ ^{α} 50/ ^{β} 33/ ^{λ} 16 |

Note: $\Delta T\%$ denotes transmittance change

^a: same TiO₂ doped WO₃ film after 500 cycles under -1V for 50 s and 1V for 150 s vs Ag/Ag⁺

^{α} : the time required for 90% change within the full transmittance modulation range after bleach at the selected wavelength

^{β} : the time required for 80% change within the full transmittance modulation range after bleach at the selected wavelength

^{λ} : the time required for 50% change within the full transmittance modulation range after bleach at the selected wavelength

Table 4.4 List of electrochromic rate parameters for pure WO₃ and TiO₂ doped WO₃ at wavelengths of 550, 632.8 and 800 nm respectively

| | Pure WO ₃ | | | WO ₃ /TiO ₂ | | |
|------------------------|----------------------|-------------|-----------|-----------------------------------|-------------|-----------|
| | 550 nm | 632.8 nm | 800 nm | 550 nm | 632.8 nm | 800 nm |
| $\gamma_c / \% s^{-1}$ | 1.4 | 2.2 | 1.5 | 1.4 | 2.2 | 2.7 |
| $\gamma_b / \% s^{-1}$ | 0.7 | 1.1 | 0.7 | 2.5 | 2.6 | 2.5 |

γ_b and γ_c were determined 10 seconds after the switch in applied voltage from the gradients of Figure 4.13

4.2.8 UV-vis spectroscopy

Figure 4.15 displays UV-vis spectra of the pure WO_3 and TiO_2 doped WO_3 thin films in their bleached and colored states for wavelengths from 300nm to 1100nm and their related optical images. Through comparison, it can be seen that the addition of ca. 10at.% titanium shows an advantage in adjusting the light transmittance within the range of both visible and NIR light. Besides, a deeper blue observed at the color state of TiO_2 doped WO_3 , seen from its corresponding optical image, confirms its larger ion accommodation ability which is consistent with the cyclic voltammetry conclusion (Section 4.2.6). In addition, after bleaching, the TiO_2 doped WO_3 shows an improved reversibility as the average light transmittance returns to 72%, which is 92% of its original value before coloration.

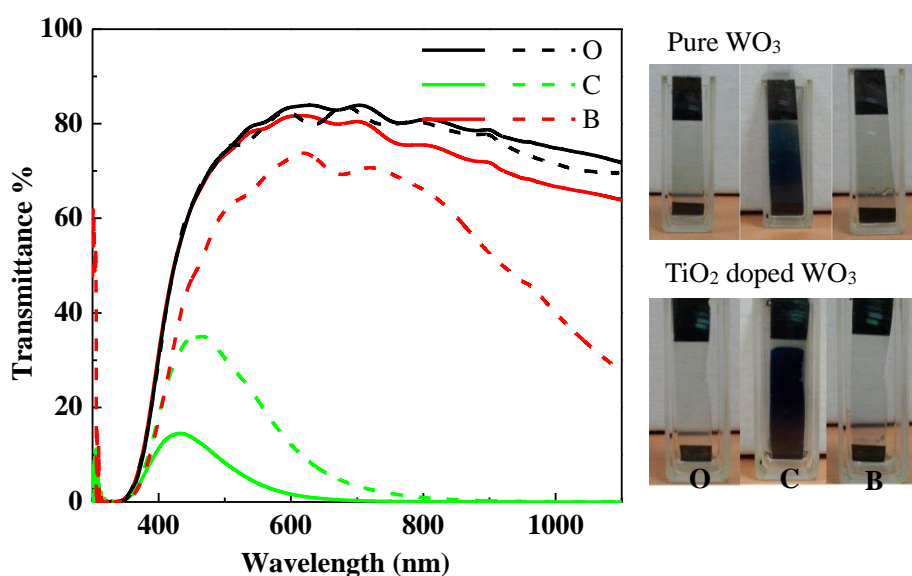


Figure 4.15 UV-vis spectra of pure WO_3 and TiO_2 doped WO_3 thin films in their bleached and colored states and their corresponding optical images. “O” stands

for original state (i.e. before coloration); “C” for color state (after coloring under -1 V for 50 s) and “B” for bleach state (after bleach under 1 V for 150 s”). The solid line “—” denotes TiO₂ doped WO₃ thin film and the dash line “- - -” represents pure WO₃ thin film.”

4.2.9 Electrochemical Impedance Spectroscopy

In order to investigate the kinetic properties of the charges within the films and their related interfaces, the impedance spectra of the pure WO₃ and TiO₂ doped WO₃ thin films in 1M LiClO₄ dissolved in propylene carbonate at a potential of -0.4V Vs Ag/Ag⁺ were recorded and are presented in Nyquist format. The data obtained was analyzed by Z-View software based on the same equivalent circuit as in Chapter 3 Figure 3.14.

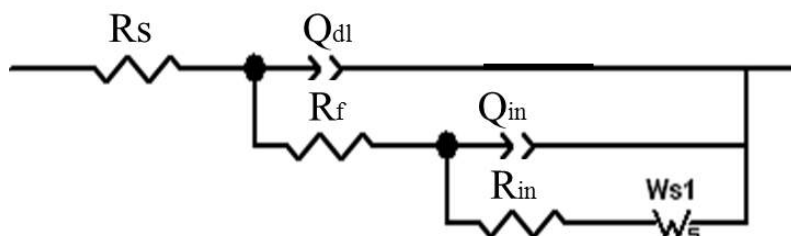


Figure 3.14 Equivalent circuit for impedance fitting; reproduced here for convenience.

Table 4.5 shows the parameters required to fit the EIS data to the equivalent circuit in Figure 3.14. It can be found that both the pure WO₃ and TiO₂ doped WO₃ thin film display a semicircle at the high frequencies and the characteristic Warburg diffusion behavior at low frequencies. The semicircle that appears at the high frequency stands for charge transport process at the FTO/film interface.

From comparing the fitting parameters it can be seen that within the experimental error Q_{dl} , R_w and τ_w are the same for the two films. The latter two parameters imply that the TiO₂ incorporations have no effect on the Li⁺ diffusion in the WO₃ film.

However, the value of R_f is 21 $\Omega \text{ cm}^{-2}$ for pure WO₃ which is three times higher than 7 $\Omega \text{ cm}^{-2}$ for TiO₂ doped WO₃ thin film, indicating a faster charge transfer process for latter film. Additionally, the value of Q_{in} for pure WO₃ thin film is four times higher than that for TiO₂ doped WO₃ thin film revealing a larger accumulation of intercalated Li⁺ on the surface of pure WO₃ films. This can be explained through analyzing the SEM images in figure 4.4. From the top view of the pure WO₃ thin film, the integrated net of larger pore diameters observed in TiO₂ doped WO₃ thin film provides spacious channel for the faster charge transport and diffusion into the film rather than residing on its surfaces. Therefore, the Q_{in} value for TiO₂ doped WO₃ thin films is lower. In contrast, the R_{in} of the TiO₂ doped WO₃ thin film is four times lower than that of the pure WO₃, manifesting a faster charge transfer process on pore surface inside the film.

Table 4.5 List of impedance fitting parameters for the pure WO₃ and TiO₂ doped WO₃ thin films.

| Film | R ₀ | R _f | R _{in} | Q _{dl} | n _{dl} | Q _{in} | n _{in} | R _w | τ _w |
|--|--------------------|--------------------|--------------------|--------------------------------------|-----------------|--------------------------------------|-----------------|--------------------|----------------|
| | Ω cm ⁻² | Ω cm ⁻² | Ω cm ⁻² | (F cm ⁻²) ^{1/n} | | (F cm ⁻²) ^{1/n} | | Ω cm ⁻² | s |
| Pure WO ₃ | 55 | 21 | 1670 | 8 E-4 | 0.82 | 2 E-4 | 0.97 | 6 E+3 | 78 |
| Fit error (%) | 0.1 | 72 | 5.6 | 5.9 | 0.8 | 23 | 3.5 | 4.5 | 7.3 |
| TiO ₂ doped WO ₃ | 73 | 7 | 454 | 5 E-4 | 0.83 | 8 E-4 | 0.82 | 4 E+3 | 93 |
| Fit error (%) | 0.2 | 72 | 5.6 | 114 | 18 | 74 | 9.0 | 2.0 | 3.7 |

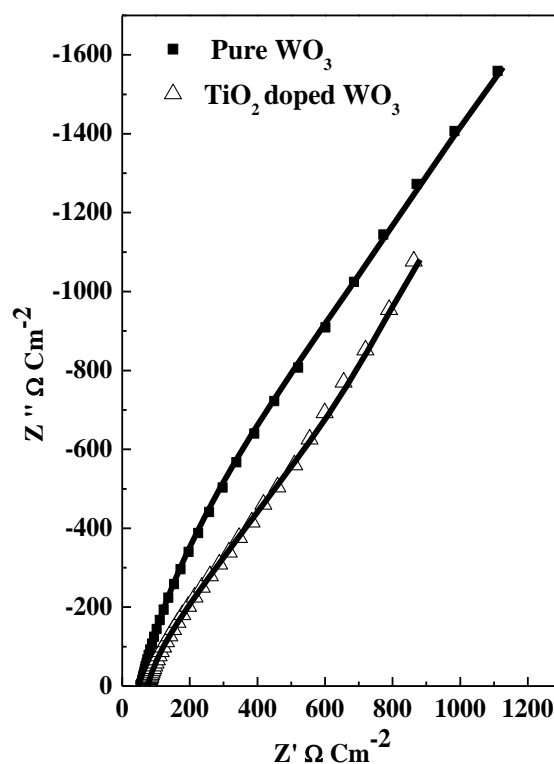


Figure 4.16 Electrochemical impedance spectra of the pure WO₃ and TiO₂ doped WO₃ thin films. The solid line is the fitting results, for the equivalent circuit shown in Figure 3.14.

4.3 Conclusions

In this chapter, the binary transition metal oxides of TiO₂ doped WO₃ thin films

with atomic ratio around 10 at.% of Ti/W were obtained by anodizing co-sputtered Ti/W thin films in fluoride containing ethylene glycol solution. The targeted TiO₂ doped WO₃ thin film exhibits better electrochromic capacities than the pure WO₃ thin film fabricated under the same conditions. Firstly, the honeycomb structure of this TiO₂ doped WO₃ thin film shows good charge accommodation ability of 75mC cm⁻² which is two and a half times larger than the pure WO₃ thin film. In addition, its superior ion storage property results in a larger light modulation range relative to the pure WO₃ thin film. Its average light modulation range is about 65% within the visible light and 70% within the NIR, which is 15% and 30% higher respectively than the pure WO₃ for the same wavelength ranges. Furthermore, the discussed TiO₂ doped WO₃ thin film displays faster electrochromic kinetic processes compared with the pure WO₃ thin film, especially in extraction of charges. This comes from its reduced interface resistance simulated through electrochemical impedance spectroscopy and its honey comb structure that gives more channels for ion transportation. Therefore, based on the above discussion, the TiO₂ doped WO₃ thin film has a promising potential for applications on “Smart Windows”.

References:

- [1] S. Hashimoto, H. Matsuoka, *J. Electrochem. Soc.* **138** (1991) 2403.
- [2] J. Götttsche, A. Hinsch, V. Wittwer, *Sol. Energ Mat. Sol. C.*, **31** (1993) 415.
- [3] J. Livage, G. Guzman, *Solid State Ionics* **84** (1996) 205.
- [4] A.E. Aliev, C. Park, *Jpn. J. Appl. Phys.* **39** (2000) 3572.

- [5] Z. Wang, X. Hu, *Electrochim. Acta* **46** (2001) 1951.
- [6] M. Yang, N. K. Shrestha, P. Schmuki, *Electrochem. Commun.* **11** (2009) 1908.
- [7] A. Z. Sadek, H. Zheng, M. Breedon, V. Bansal, S. K. Bhargava, K. Latham, J. Zhu, L. Yu, Z. Hu, P. G. Spizzirri, W. Wlodarski, K. Kalantar-Zadeh, *Langmuir* **25** (2009) 9545.
- [8] K. Kalantar-Zadeh, A. Z. Sadek, H. Zheng, V. Bansal, S.K. Bhargava, W. Wlodarski, J. Zhu, L. Yu, Z. B. Hu, *Chemical*, **142** (2009) 230.
- [9] J. R. Jennings, A. Ghicov, L. M. Peter, P. Schmuki, and A. B. Walker, *J. Am. Chem. Soc.*, **130(40)** (2008) 13364.
- [10] S. Hashimoto, H. Matsuoka, *J. Electrochem. Soc.*, **138(8)** (1991) 2403.
- [11] D. J. Blackwood, R. Greef and L. M. Peter, *Electrochimica Acta*, **34(6)** (1989) 875
- [12] D. Regonini, C. R. Bowen, A. Jaroenworoluck and R. Stevens, *Materials Science and Engineering: R: Reports*, **74(12)** (2013) 377
- [13] N. R. de Tacconi, C. R. Chenthamarakshan, G. Yogeewaran, A. Watcharenwong, R. S. de Zoysa, N. A. Basit, K. Rajeshwar, *J. Phys. Chem. B*, **110(50)** (2006) 25347.
- [14] B. Wieland, J.P. Lancaster, C.S. Hoaglund, P. Holota, W.J. Tornquist, *Langmuir* **12** (1996) 2594.
- [15] M. L. Wang; Y. N. Liu; H. Yang, *Electrochim. Acta* **62** (2012) 424.
- [16] S. Q. Li; G. M. Zhang; G. D. Guo; L. G. Yu; W. Zhang. *J. Phys. Chem. C* **113** (2009) 12759.
- [17] V. Galstyan, A. Vomiero, E. Comini, G. Faglia, G. Sberveglieri. *RSC Adv* **1** (2011) 1038.
- [18] J. M. Macak, H. Tsuchiya, L. Taveira, S. Aldabergerova and P. Schmuki, *Angew. Chem., Int. Ed.*, **44** (2005) 7463.
- [19] F. Zhang, S. Chen, L. Yang and Y. Yin, *Adv. Mater. Res.*(Zurich, Switzerland), **47-50** (2008) 1209.
- [20] W. Li, J. Li, X. Wang, S. Luo, J. Xiao, and Q. Chen, *Electrochimica Acta*, **56** (2010) 620.
- [21] Y.-C. Nah, A. Ghicov, D. Kim, and P. Schmuki, *Electrochem. Comm.*, **10** (2008) 1777.
- [22] V. Cristino, S. Caramori, R. Argazzi, L. Meda, G. L. Marra, and C. A. Bignozzi, *Langmuir*, **27** (2011) 7276.
- [23] The International Centre for Diffraction Data ICDD card 00-005-0364
- [24] C. G. Granqvist *Handbook of inorganic electrochromic materials*, New

- York, (1995).
- [25] P. Judeinstein, R. Morineau, J. Livage, *Solid State Ionics* **51** (1992) 239.
- [26] L. G. Teoh, I. M. Hung,^a J. Shieh,^b W. H. Lai, and M. H. Hona, *Electrochem. Solid St.*, **6 (8)** (2003) G108.
- [27] L. E. Depero, S. Groppelli, I. Natali-Sora, L. Sangaletti, G. Sberveglieri and E. Tondello, *J. Solid State Chem.*, **121** (1996) 379.
- [22] [28]P. S. Patil, S. H. Mujawar, A. I. Inamdar, S. B. Sadale, *Appl.Surf.Sci.* **250** (2005) 117.
- [23] [29]M. F. Daniel, B. Desbat, J. C. Lassegues, B. Gerand, M. Figlarz, *J. Solid State Chem.* **67** (1987) 235.
- [30] A. G. Souza-Filho, V. N. Freire, J. M. Sasaki, J. Mendes Filho, J. F. Julião, U. U. Gomes, *J. Raman Spectroscopy* **31** (2000) 451.
- [31] H. D. Zheng, Y. Tachibana, K. Kalantar-Zzadeh, *Langmuir*, **26** (2010) 19148.
- [32] A. Raougier, F. Portemer, A. Quede, M. EI Marssi, *Appl Surf Sci.* **153** (1999) 1.
- [33] M. Regragui, M. Addou, A. Outzourhi, J. C. Bernede, E. EI Idrissi, E. Benseddik, A. Kachouane, *Thin Solid Films*, **358** (2000) 40.
- [34] B. D. Cullity, *Elements of X-ray Diffraction*, Addison-Wesley, Reading,1978; G. Gouadec and P. Colomban, *Prog. Cryst. Growth Charact. Mater.* **53** (2007) 1
- [35] C. Y. Kim and R. A. Condrate, *J. Phys. Chem. Solids*, **45(11/12)** (1984) 1213
- [36] S. J. Dillon and M. P. Harmer, *J. Am. Ceram. Soc.* **89** (2006) 3885; L. Vayssieres, *Int. J. Nanotechnol.* **1(1/2)** (2004).
- [37] M. J. Yoder, *J. Quant. Spectrosc. Radiat. Transfer.*, **14** (1974) 1317.
- [38] L. Dixit, S. K. Kapoor, I. D. Singh, P. L. Gupta, *Indian J. Phys., B* **51** (1977) 116.
- [39] S. Komornicke, M. Radecka, P. Sobas, *J. Mat. Sci.: materials in electronics*, **15** (2004) 527.
- [40] B. Vincent Crist, *Handbooks of Monochromatic XPS spectra*, (1999).
- [41] S. R. Bathe, P. S. Patil, *Solid State Ionics*, **179** (2008) 314.

Chapter 5 Studying on influence of different amount of TiO₂ dopants on the electrochromic property of WO₃

5.1 Introduction

In Chapter 4, the thin films, with an atomic Ti/W ratio of approximately 10 at.%, produced by anodization in a fluorinated organic solvent show an equivalent large light transmittance change as those synthesized by the hydrothermal method in chapter 3, but in the former the switch was triggered under a lower voltage. In addition, relative to pure WO₃ thin film fabricated under the same anodization conditions in chapter 4, the titanium doped WO₃ thin film displays enhancements on light transmittance change, bleach time and coloration efficiency. However, it would be much more attractive to industry if the organic solvent could be replaced by an aqueous one, which will be the focus of the present chapter. Furthermore, this chapter will also look at the influence of varying the titanium content in the doped WO₃ thin films.

Previous work in aqueous media include that of Mukherjee *et al.* who in 2003 produced nanoporous tungsten oxide by galvanostatic anodization of tungsten foil in oxalic acid,^[1] as opposed to the non nanoporous structures observed by anodization of tungsten foil in either HNO₃ or H₂SO₄ solutions.^[2-3] However, Mukherjee *et al.*'s porous structures are not entirely regular and they did not explore the respective applications. Later on, in 2005, Tsuchiya *et al.* observed

a self-organized nanoporous morphology with high regularity by anodizing pure tungsten foil at a constant potential in various NaF concentrations.^[4] In their work, they investigated the relationship between pore morphology and the F⁻ concentration and the selected constant voltage. They did a good job on providing preliminary anodization data for obtaining good porous WO₃ thin films and investigated a series of aqueous solutions however, they only focused on tungsten foil.^[5-8]

It was not until 2009 that nanoporous anodic WO₃ thin film grown on conductive glass were synthesized by Zheng *et al.*^[9] who adopted RF magnetron sputtering to deposit a layer of pure tungsten on FTO glass, followed by anodizing in NH₄F dissolved in ethylene glycol. Their work was focused on studying the different pore morphologies obtained different anodization times at 40 V. However, these authors did not work in aqueous electrolytes. Nevertheless, they did briefly compared the photocatalytic activities among these WO₃ films under UV illumination and observed improved photocatalytic activities for thick porous WO₃ thin films which they attributed to its large surface area produced by its rich pore structures. This suggests that the advantages of pore structures for increasing the surface area could also benefit the films electrochromic properties.

Therefore, in this chapter the anodization technique will be extended to the

fabrication of TiO₂ doped WO₃ thin films, which the two preceding chapters suggest have several advantages over their pure counterparts, in an aqueous electrolyte. In addition, the influence of varying the titanium content on the electrochromic properties will also be discussed in this chapter and it will be seen the optimum level is about 10 at.%. The electrolyte used for all anodization was 1 M H₂SO₄ containing 0.3 wt.% NaF, with the anodizing conditions being previously described in Chapter 2, Section 2.2. The choice of this electrolyte is based on the previous work of Tsuchiya *et al.* on tungsten foils.^[4]

5.2 Results and discussions

5.2.1 Morphology and elemental distribution analysis

The amount of titanium mixed into the tungsten matrix through co-sputtering was controlled by adjusting the separate sputtering powers. The sputtering power applies to pure tungsten was fixed at 90 W and the power selected for sputtering titanium simultaneously was set to either 10 watt, 15 watt or 20 watt. The elemental distribution of titanium atoms after the co-sputtering was analyzed by the SEM-EDS. This revealed that the atomic percentages of titanium in the as-sputtered Ti/W thin films were 10 at.%, 13 at.% and 17 at.%, a minor variation of 0.6 at% was found at various locations across a single surface. In addition, by adjusting the electron beam density of SEM-EDS from 10 KV to 20 KV it was possible to analyze the titanium distribution within the

films in further depth, it is found that it is uniform throughout the samples.

However, after anodization the detected atomic percentage of titanium (only considering the metal components W and Ti) decreased to 7 at.%, 10 at.% and 15 at.% respectively, which likely reflects the faster dissolution rate, which can be controlled under different pH value, solvent viscosity and water contents, of the titanium over tungsten as discussed in Chapter 4. This conclusion is confirmed by observing and comparing the change of the thickness from the SEM cross-section images before and after anodization. The films discussed in this chapter are named as WT0, WT7, WT10 and WT15 corresponding to the 0 at.%, 7 at.%, 10 at.% and 15 at.% of titanium in WO_3 matrix respectively.

In order to observe the effect of titanium incorporations on the morphology change of the oxide films after sputtering, SEM images were captured. Figure 5.1(a) demonstrates a typical top view of films after sputtering, the morphology of which is independent of the amount of titanium co-sputtered. It can be seen that the as-sputtered films consist of octahedral particles. Otherwise, cross section images in Figure 5.1(b) show arrow-head shaped particles that stack layer by layer to form column structures. Furthermore, these columns with arrow-head shape appear to adhere on the FTO substrate strongly as no cracks are found at the interface between FTO surface and the bottom of the grown films. Besides, these columns also stick to each other closely, implying a

compact structure which is important for obtaining an oxide film with good qualities during the anodization. From SEM cross section, the thickness of the as-sputtered films are estimated to be around 450 nm.

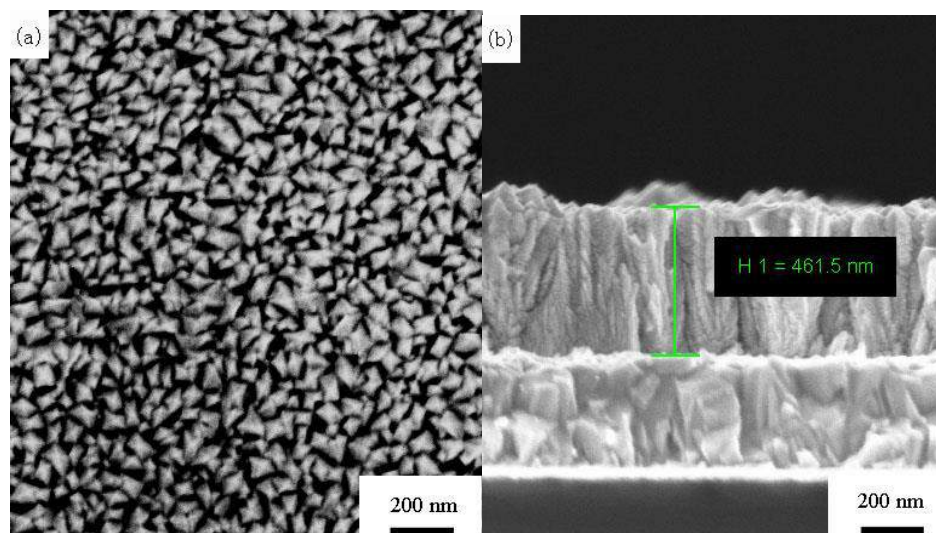


Figure 5.1 SEM images (a) top view and (b) cross section of as-sputtered pure tungsten thin film. The morphologies of the as-sputtered tungsten/titanium thin films with different atomic percentage of titanium do not show significant variations from the pure WO_3 .

SEM images were again collected after the films have been anodized in the 1 M H_2SO_4 contain 0.3 wt% NaF. Figures 5.2 and 5.3 shows series of morphology changes as the amount of titanium incorporated in the film increases: from nanoporous, observed in WT0 and WT7; undergoing nano-flakes in WT10; to nanoblock inter-weaved porous structures of WT15. The formation of the nanoporous structure of pure WO_3 films anodized in fluoride ion (F^-) aqueous solutions are the commonly formed morphologies reported by many other groups and as described above in Section 4.1. As described in Chapter 4 the pore formation is ascribed to the built-in balance between electrochemical oxidation and chemical dissolution,^[10] the ratio of which can be deduced from

the steady state region (long times) of the characteristic anodic transient current density curves. It can be clearly seen in Figure 5.4 that the long-term current density increases with increasing titanium content, implying both faster electrochemical oxidation and chemical dissolution, thus a lower degree of order in the formed nanoporous morphologies.

The average pore size of WT0 is 80 nm which is much larger than that of 20 nm of the pure WO_3 anodized in ethylene glycol solutions. Furthermore, the WT0 has good integrity without any of the cracks appearing in pure WO_3 thin film in Chapter 4. This implies that the aqueous system is advantageous in anodizing films with uniform surface. The similarity in the porous structures of WT7 as WT0 indicates that 7 at% titanium has only a very limited effect on film morphology. However, WT10 consists of nano-flakes instead of completely pores. These nano-flakes are perpendicular to the substrate and disorderly arranged, forming spacious channels and large wall surface. This is not observed in TiO_2 doped WO_3 thin films produced by anodizing in fluorinated ethylene glycol in Chapter 4, even though it contains ca. 10 at. % titanium. By increasing the atomic percentage of titanium to 15% continuously, the pores collapse and become pores with scattered nano-blocks seen in WT15 (Figure 5.3d).

Additionally, the cross section SEM images of the final anodized and annealed specimens reveal that the thickness of all the films has been reduced from 450

nm to 350 nm for WT0 and to 300 nm for WT7, WT10 and WT15 (Figure 5.3). This is in contrast with observations of the films formed in ethylene glycol in Chapter 4 where the thickness of both pure WO_3 and TiO_2 doped WO_3 thin films is increased after anodization. The reduction of films thickness in the aqueous solution implies that the dissolution rate of the oxide film in aqueous solution (or direct corrosion of the metals) is faster than that in organic solution. Because NaF has a much higher solubility in water solution than in any organic system, it enhances the dissolution reactions displayed previously in Equations 4.2 and 4.4.

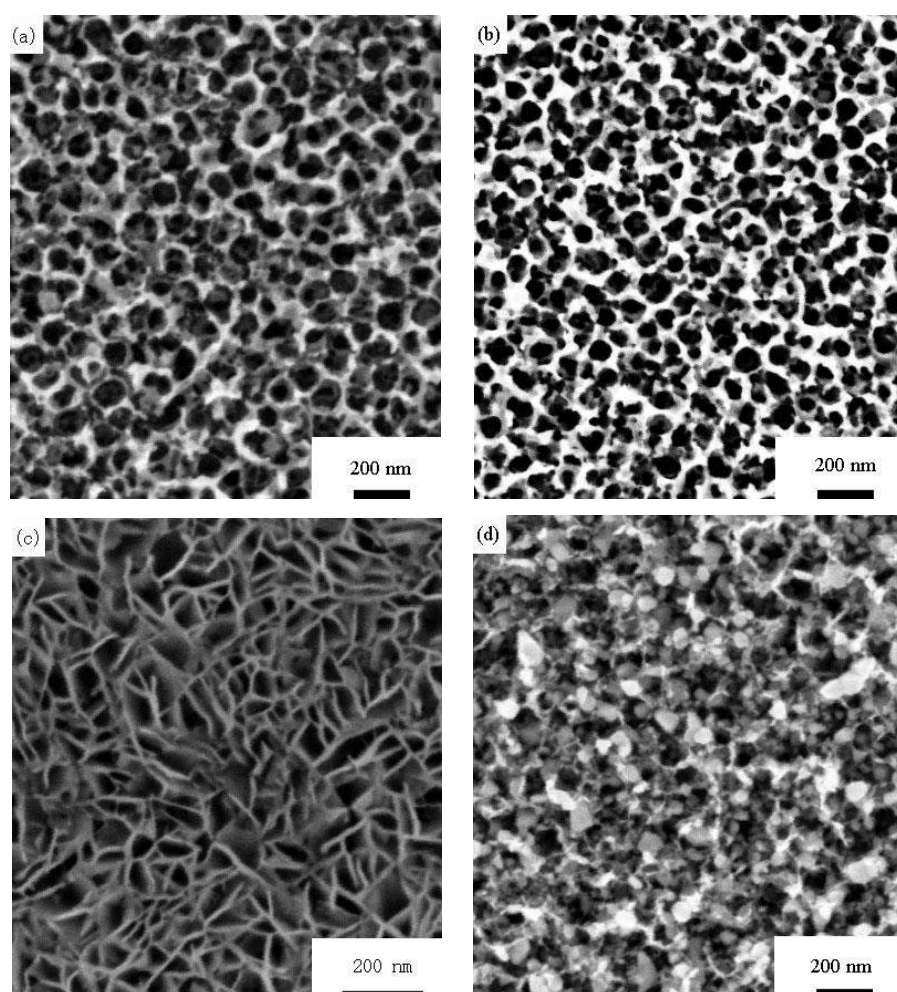


Figure 5.2 SEM top images of (a) WT0, (b) WT7, (c) WT10 and (d) WT15 films. All these films were anodized in 0.3 wt% NaF dissolved in 1 M H_2SO_4 under 40

V for 40 mins and annealed at 450°C for 3 h.

From the cross section SEM images in Figure 5.3 it can also be seen that the pores are arranged orderly in WT0 and WT7, but there no pores are observable close to the oxide / substrate interface. In WT10 vertically aligned plates are found, which are agreement with its nano-flake structures viewed in the top image. A less porous structure is observed for WT15 due to coverage of interweaved nano-blocks, so again the top and cross section views are consistent.

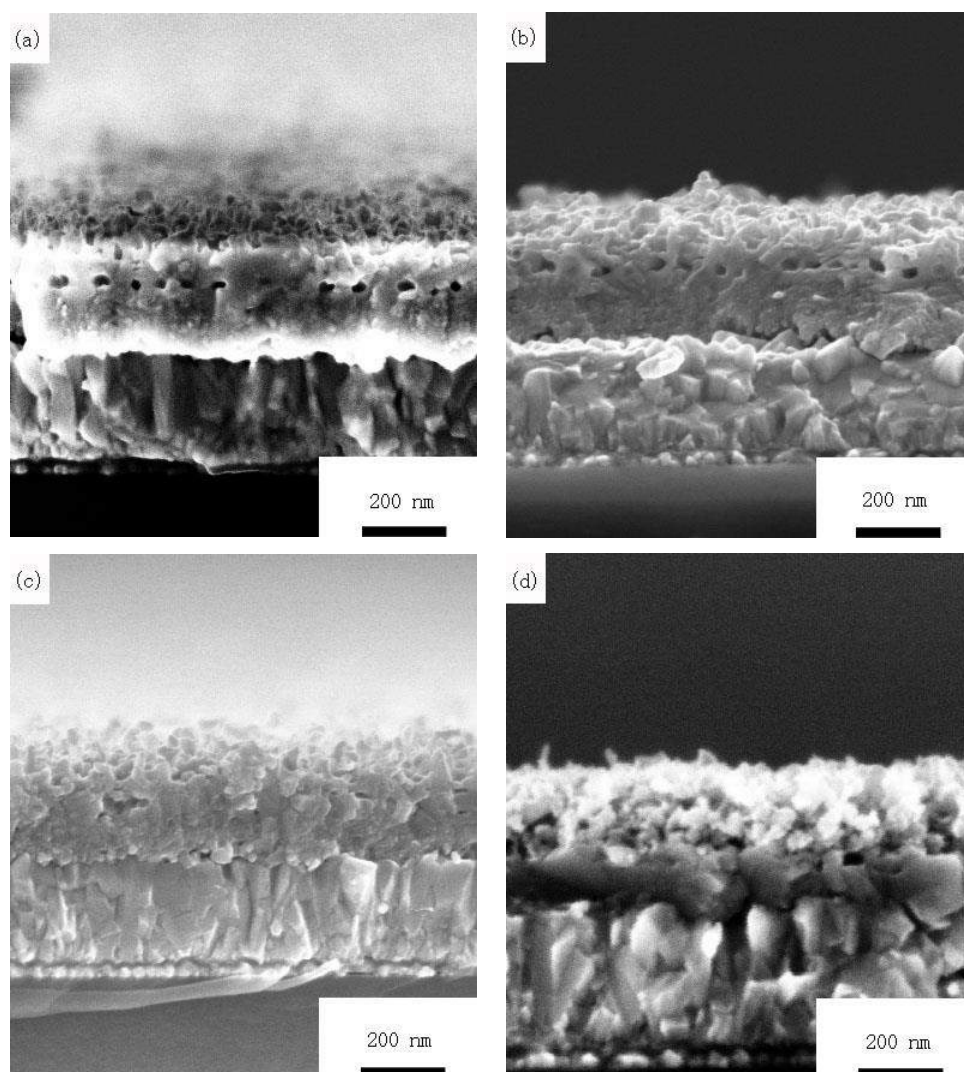
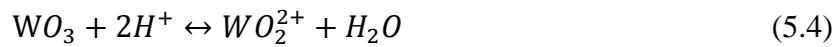
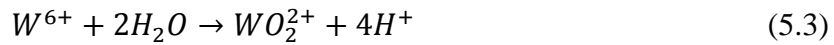
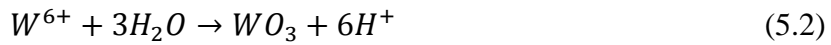
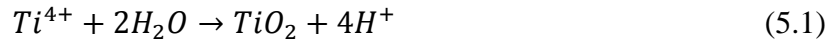


Figure 5.3 SEM cross section images of (a) WT0, (b) WT7, (c) WT10 and (d)

WT15 films. All these films were anodized in 0.3 wt% NaF dissolved in 1 M H₂SO₄ under 40 V for 40 mins and annealed at 450°C for 3 h.

Although the details of the morphological evolution of WO₃ films are not fully understood, it is clear that complex reactions involved during anodization of Ti/W thin films play important roles. Inspection of the steady-state current densities in Figure 5.4 indicates that under the same anodization conditions the film's oxidation rate increases with increasing titanium content. The possible anodic chemical reactions could be occurred:



The thicken of the walls observed in Figure 5.2(c) and the blocks scattered in porous structure in Figure 6.2(d) is possibly induced by the precipitation of primary particle nuclei induced by the supersaturation condition and crystal growth of the soluble products on the film surface.^[11] Based on above equations, WO₂²⁺ could have the role of the soluble product since the dissolution rate of titanium oxide to form (TiF₆)²⁻ is faster than that of tungsten trioxide. This means that the local acidity in the titanium doped WO₃ is higher. Therefore, the produced H⁺ may lead to increased dissolution of the WO₃ thin film.^[12]



The soluble species WO₂²⁺ near the surface of the formed oxide layer will be attacked by water to form W₂O₅ intermediately, followed by the formation of

WO₃ causing thickening of the WO₃ nanostructured film.^[11,13] However, the full mechanism model for the morphology change during anodization of titanium doped tungsten oxide with different titanium contents still needs further and detailed investigations.

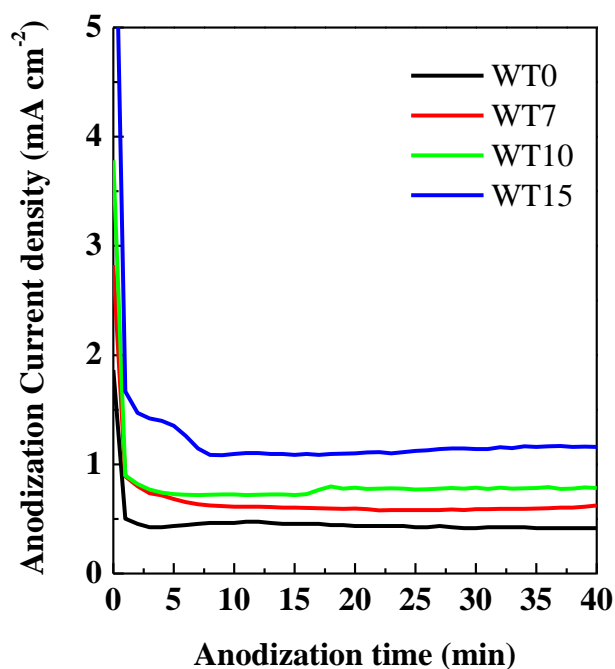


Figure 5.4 Anodic current density transients for Ti/W films in 0.3 wt% NaF Dissolved in 1 M H₂SO₄ under a sweep potential rate of 1 V s⁻¹ for 40 s to a fixed potential of 40 V for 40 min.

5.2.2 Structural analysis

Figure 5.5 shows XRD patterns for WT0, WT7, WT10 and WT15 thin films, along with indicated positions of the peaks belonging to the FTO substrate. All the remaining peaks in the diffraction patterns can be indexed to the ICDD data file for WO₃ with monoclinic structures and all the films display polycrystalline

features. The easily identified (001), (020) and (200) peaks in the diffraction patterns for pure WO_3 thin film are assigned to the typical monoclinic structures.^[14]

It can be seen from Figure 5.5 that the titanium dopants cause sharp decrease on the relative intensity of (001) and (200) peak so that it is no longer resolved as separate peaks. The details of peaks' positions are listed in Table 5.1, there is no obvious peak shift for these TiO_2 doped WO_3 thin films with an atomic percentage of titanium from 0 to 15, except (200) peak of WT7 and WT10, shifting -0.2° and -0.4° respectively compared with pure WO_3 thin film. These phenomena reflect that firstly the titanium is likely to prefer occupying (020) plane inducing lattice constant variations and secondly the titanium interrupts orderly arranged atoms on other planes. These two factors result in peak shift and decrease on peak intensities. A similar small angular displacement was also observed in Chapter 4 for ca. 10 at% TiO_2 doped WO_3 thin films anodized in ethylene glycol solutions, for which an average peak shift toward smaller two theta angles is found.

Table 5.1 List of XRD peak positions for WT0, WT7, WT10 and WT15

| | (001) | (020) | (200) | (-111) | (-221) | (022) | (041) | (-401) | (-222) |
|---|-------|-------|-------|--------|--------|-------|-------|--------|--------|
| Monoclinic | 23.1 | 23.6 | 24.4 | 28.7 | 41.5 | 53.6 | 54.3 | 55.8 | 59.4 |
| WT0 | 23.2 | 23.6 | 24.3 | 28.7 | 41.4 | 53.6 | 54.5 | 55.9 | -- |
| ^a Pure WO ₃ | 23.1 | 23.7 | 24.3 | 28.8 | 41.6 | 53.4 | 54.7 | 55.8 | -- |
| WT7 | 23.2 | 23.6 | 24.1 | 28.9 | 41.4 | -- | 54.5 | -- | -- |
| WT10 | 23.2 | 23.6 | 23.9 | 28.6 | 41.6 | -- | 54.2 | -- | -- |
| ^a TiO ₂ doped WO ₃ | -- | 23.5 | 24.2 | 28.8 | 41.3 | -- | 54.0 | -- | 59.7 |
| WT15 | 23.3 | 23.6 | 24.1 | -- | -- | -- | 54.6 | -- | -- |

a denotes the corresponding films discussed in Chapter 4 where anodization was in an organic solvent

For WT15 thin film, it can be seen that entire intensity of XRD peaks dropped greatly; despite the same detectable surface area as the other films. These alterations indicate less crystallinity in the TiO₂ doped WO₃ thin films than the pure WO₃ film and that the degree of the disorder is enhanced with the increasing percentage of titanium in pure WO₃ matrix. This conclusion is consistent with the SEM images in which the pure WO₃ thin film shows self-ordered porous structures, WT10 exhibited randomly arranged nano-flakes vertically sticking on the FTO substrate and WT15 totally disorder structures with scattered nano-blocks within the formed network of the nano-pores (Figure 5.5). Additionally, the same phenomenon is also observed by Lethy *et al.* who used a pulsed laser deposition technique to produce WO₃/TiO₂ films on quartz

substrates.^[15] Finally, no traces of TiO₂ can be found in any of the XRD patterns suggesting that the titanium is incorporated into the WO₃ lattice rather than forming a separate phase, although the lack of TiO₂ peaks could also be due to the low content of titania or this could remain amorphous even after annealing.

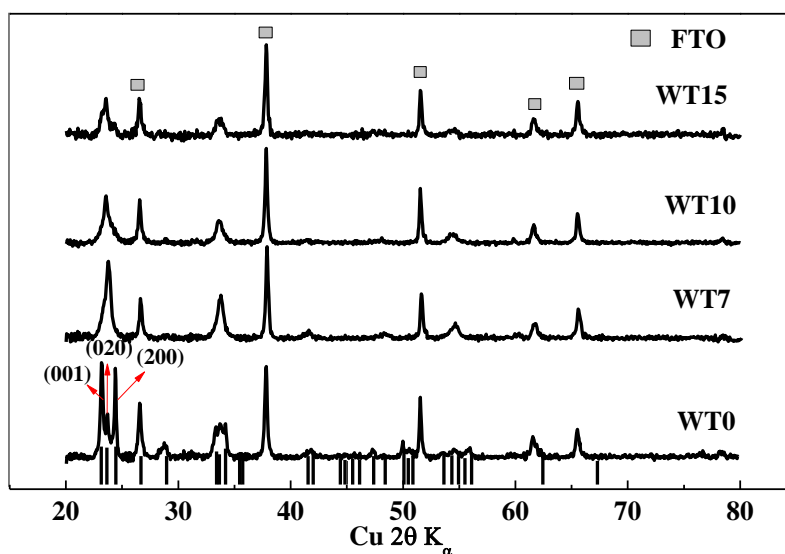


Figure 5.5 XRD patterns for WT0, WT7, WT10 and WT15.

Figure 5.6 shows the room temperature Raman spectra of the electrochromic films, in which the previously reported O–W⁶⁺–O stretching and bending modes expected for monoclinic WO₃ can be found, although the two bending modes cannot be resolved for the TiO₂ doped WO₃ thin films (Chapter 4, Section 4.3.2). Nevertheless, it can be seen that on incorporation of titanium atoms into the WO₃ films the O–W⁶⁺–O stretching band at 719 cm⁻¹ in pure WO₃ (WT0) red-shifts by about 20 wavenumbers and broadens considerably. Shigesato *et al.*^[16] pointed out that the width of the Raman peak at about 800 cm⁻¹ is related to structural disorder aspects of W–O–W bonding angle and length. According to

Lethy *et al.*,^[15] the same phenomenon is also observed when titanium oxide is incorporated into tungsten oxide thin films via a pulsed laser deposition technique and these authors explained the broadening of stretching mode in terms of neighboring geometric disorientation based on the molecular theory of vibration.^[17] This explanation is consistent with the XRD observations. The broadening of the main peaks with increasing titanium contents implied an interruption on the atoms alignment. Alternatively, the red-shift of the Raman peaks at 719 cm^{-1} could be attributed to increased tensile strain as proposed by Liao *et al.*^[18] and Portinha *et al.*^[19] when studying on ZrO_2 and IrO_2 . Otherwise, the same phenomenon is also observed in figure 4.8 for the films anodized in an organic electrolyte presented in Chapter 4.

In addition, figure 5.6 reveals that the frequencies of the two low frequency bending modes are broadened and weakened with the increasing of titanium contents to the extent that they are almost undetectable at the highest titanium incorporations (WT15). In the light of the molecular theory of vibration, it is likely that the substitution of W^{6+} by Ti^{4+} ions caused local geometric disorientation in WO_3 thin film.^[17,20] Besides, the TiO_2 dopants also lead to the appearance of a new Raman band near 983 cm^{-1} , which is also detected in TiO_2 doped WO_3 thin films anodized in ethylene glycol solutions (Figure 4.5). This band, which has been reported at 996 cm^{-1} for WO_3 /transition metal oxide catalysts, including WO_3/TiO_2 , has been assigned to a $\text{W}=\text{O}$ symmetrical

stretching mode characteristic of the WO_3 monolayer dispersion,^[21] Furthermore, this additional band proves a change of structures due to the titanium dopants as well.

Meanwhile, there is no evidence of any separate TiO_2 phases, for which the A_{1g} mode at 612 cm^{-1} / 512 cm^{-1} is the strongest followed closely by the E_g mode at 447 cm^{-1} / 634 cm^{-1} for rutile / anatase TiO_2 .^[22-23] This also supports the discussions from XRD results that the TiO_2 in WO_3 matrix does not form a separate phase. In addition, this phenomenon is observed in all WO_3/TiO_2 thin films regardless of whether anodized in ethylene glycol solution discussed in chapter 4 or aqueous solution in this chapter.

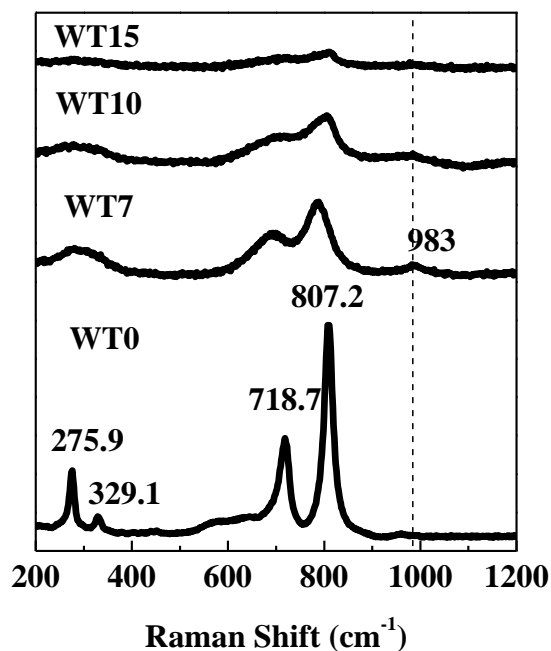


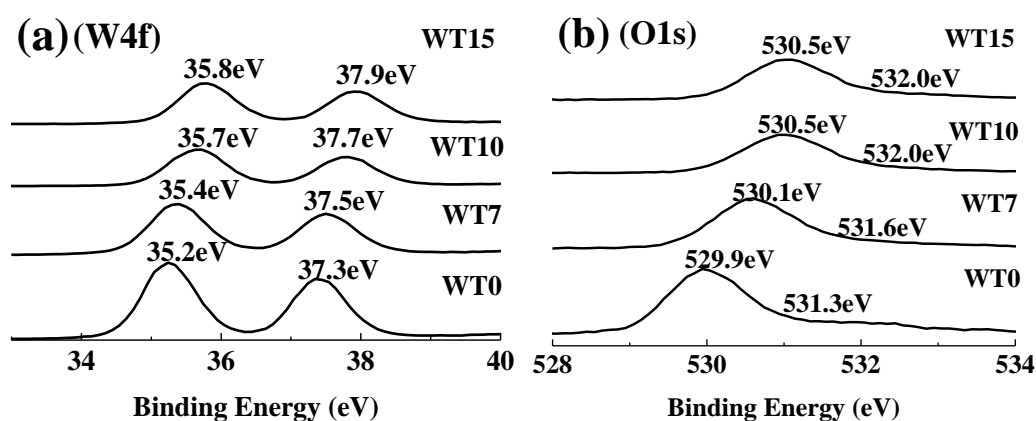
Figure 5.6 Raman spectra of WT0, WT7, WT10 and WT15.

In order to ascertain the surface chemical composition and their chemical state, XPS scans of as-prepared thin films of WT0, WT7, WT10 and WT15 were obtained and are shown in Figure 5.7. As expected all the films contain tungsten and oxygen elements, with titanium element also detected in WT7, WT10 and WT15 with atom ratio of Ti/W 7 at.%, 12 at.% and 18 at.% separately. This is an average difference of 2% from the SEM-EDS. Furthermore, through investigating peak positions, the W4f_{7/2} and W4f_{5/2} peaks are found to be well resolved in the spectra of all films as listed in Table 6.2, being located at 35.2 eV~35.8 eV and 37.3 eV~38.9eV belonging to W⁶⁺ without other oxidation states being present.^[24-27] Otherwise, the binding energies of Ti 2p_{3/2} and Ti 2p_{1/2} located at 458.4 eV~459.0 eV and 464.2 eV~464.8 eV are attributed to Ti⁴⁺.^[28-29] Additionally, The O1s binding energy of 529.9 eV~ 530.5 eV are identified and classified to the oxygen in the WO₃ structure.^[30]

Table 5.2 Binding energy list of atoms orbits of W4f, Ti2p and O1s for film WT0, WT10, WT10 and WT15

| | | WT 0 | WT7 | WT1 0 | WT15 | |
|------------------------|-----|---------|-------|----------|-------|-------|
| Binding Energy (eV) | W4f | (5/2) | 37.3 | 37.5 | 37.7 | 38.9 |
| | | (7/2) | 35.2 | 35.4 | 35.7 | 35.8 |
| | Ti2 | (1/2) | | 464.1 | 464.6 | 464.9 |
| | P | (3/2) | | 458.6 | 458.9 | 459.2 |
| | O1s | | 530.5 | 530.4 | 530.6 | 530.7 |
| | | 532.1 | 531.9 | 532.5 | 532.4 | |

From Table 5.2, it can be seen that all the XPS peaks exhibit a trend toward higher binding energies with an increase of titanium content. This shift of binding energy implies a contraction of the WO_3 unit cell. However, information from XPS only reflects surface information which is mostly influenced by the ambient such as absorption of water molecules resulting a positive pressure on surfaces.^[31] Nevertheless, through observing the XRD data, it can be seen that all the peaks do not shift to the same side, maybe implying different internal stresses. According to the Raman spectra in this chapter, the peaks shift toward lower wavenumber and this has been reported due to the increase of tensile strain by Liao *et al.* and Portinha *et al.*^[18-19] Therefore, a compressive stress should also be provided to balance stress at grain boundaries. These two kinds of strain will result in changes in the dimensions of the unit cell, i.e. lattice constants.



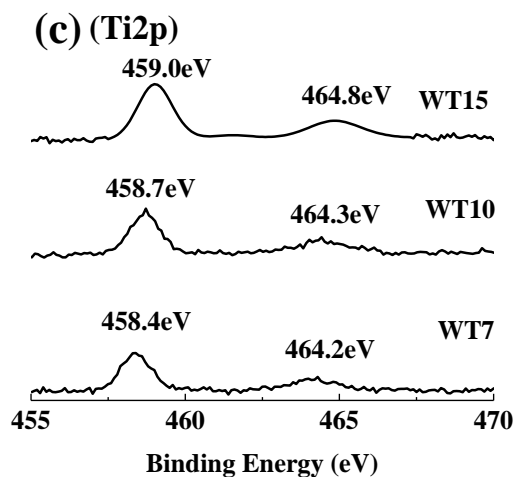


Figure 5.7 Comparison of XPS spectrum of thin film WT0, WT7, WT10 and WT15 (a) W4f orbit, (b) O1s orbit and (c) Ti2p orbit

5.2.3 Cyclic voltammetry

Figure 5.8 shows cyclic voltammograms for each of the four thin films at their first, 500th and 1000th cycle at a sweep rate of 50 mV s⁻¹. Besides that Figures 5.9 compares the cyclic voltammetric features of these four thin films at their respective first and 1000th cycle respectively. Figure 5.10 shows the amounts of charge inserted into WT0, WT7, WT10 and WT15 calculated by integration of the current density recorded in Figure 5.8. (i.e. the area enclosed by the CV curves).

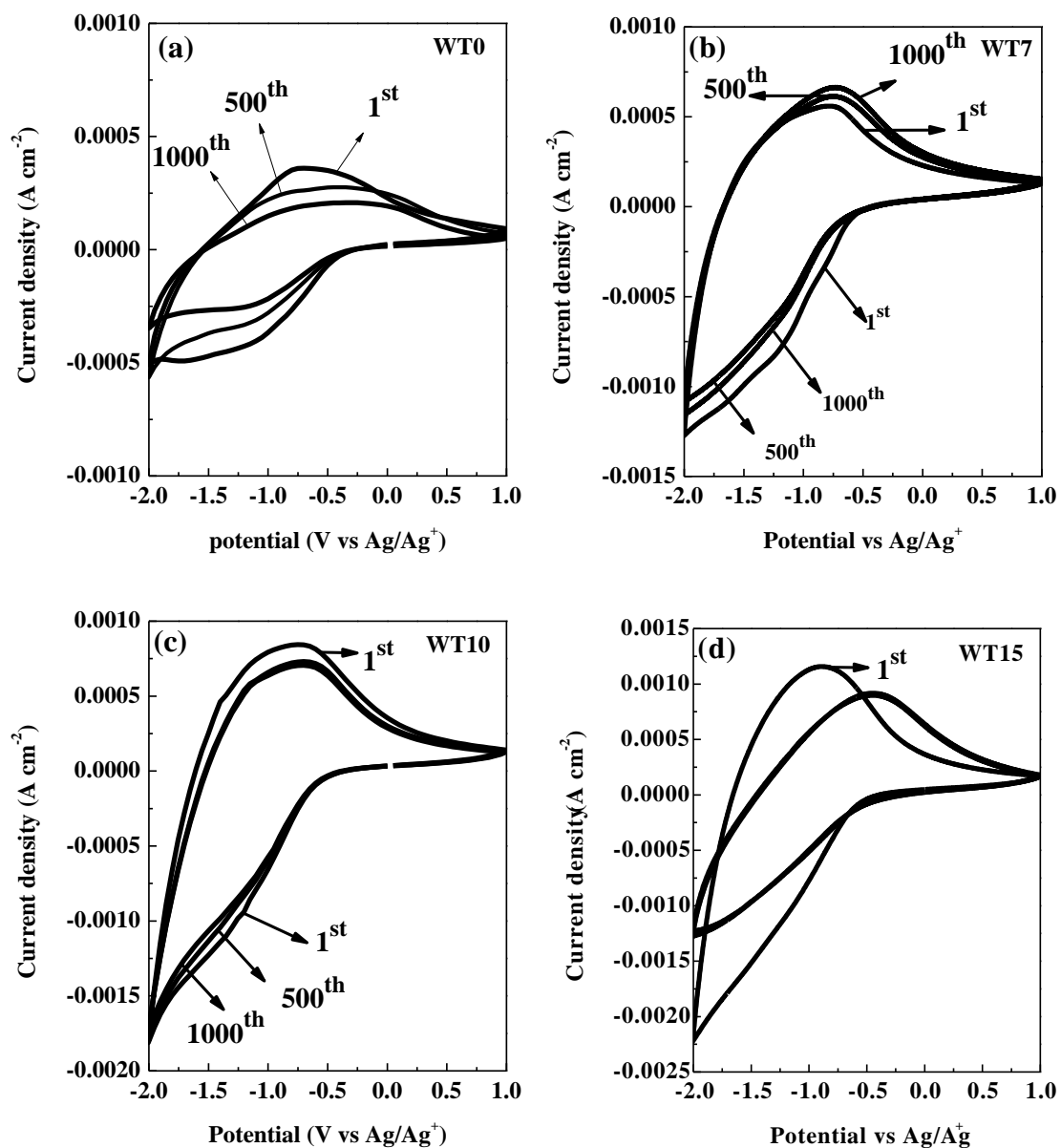


Figure 5.8 Cyclic voltammograms collected on their 1st, 500th and 1000th cycle in 1M LiClO₄ dissolved in propylene carbonate at a sweep rate of 50 mV s⁻¹ from -2V to 1V vs. Ag/Ag⁺ for (a) WT0, (b) WT7, (c) WT10, (d) WT15.

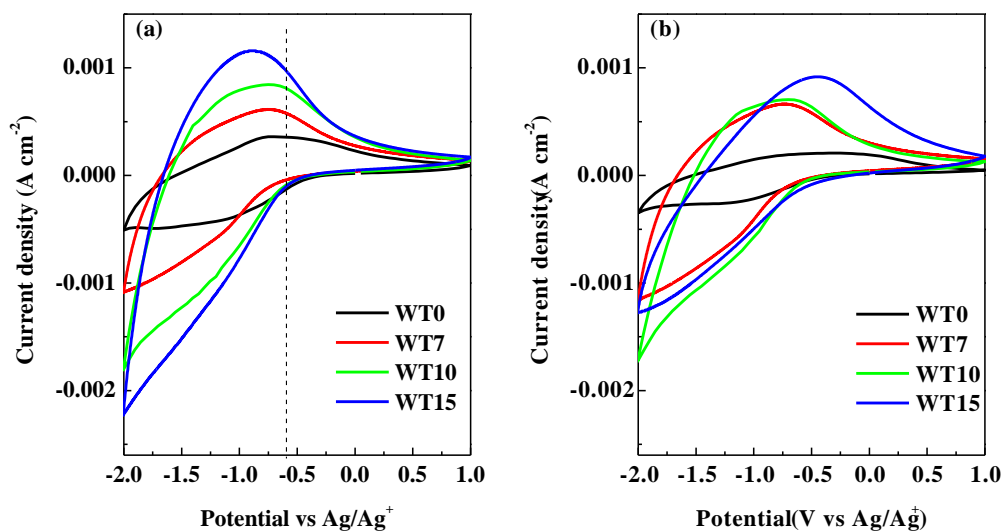


Figure 5.9 Comparison of cyclic voltammograms corresponding to figure 5.8 at their respective (a) first cycle and (b) the 1000th cycle.

From Figure 5.10 and Table 5.3 it can be seen that the amount of inserted Li⁺ increases with increasing titanium content which also can be determined by comparing the current densities of WT0, WT7, WT10 and WT15 shown in Fig. 5.8. Meanwhile the charge insertion rate, defined as the total amount of Li⁺ intercalated into the thin film within 40 seconds, also increased with the same trend. This increasing trend with increased titanium quantity in the WO₃ matrix is believed to be due to the more disordered structure induced by incorporating the titanium.

After 1000 cycles the capacitance loss of WT0, WT7, WT10 and WT15 reaches 40%, 15%, 5% and 32% respectively, corresponding with the change of in the CV profiles seen in Figure 5.8. The capacitance loss is caused by losing effective places for ion intercalation again. It seems that up to 10 at.% titanium greatly decreased the capacitance loss rate, but a further addition of titanium to

15 at.% was detrimental. The possible reason is ascribed to morphology of WT15, in which the randomly distributed nano-blocks may impede the transport of charges. (Figure 5.2d) The morphology of WT10 is more convenient for ions insertion/extraction to avoid retention of ions during de-intercalation process which will prevent the intercalation of ions in the following cycles.

Comparing the charge capacitance of films obtained in the present chapter, via anodizing in an aqueous media, with those formed in ethylene glycol presented in Chapter 4, Table 4.2 reveals that the q_{in} of films formed in the organic electrolyte are more than twice that of their aqueous counterparts; this also applies to the pure WO_3 films. This is likely resulted from two aspects. Firstly, the thin films from ethylene glycol solution are approximate 2.5 times thicker than these obtained from the aqueous electrolyte. Secondly, the morphology differences could be largely responsible for these charge capacitance variations, as it can be seen from their respective SEM images in chapter 4 that the TiO_2 doped WO_3 thin film has more volume for charge insertion due to its denser honey-comb structure.

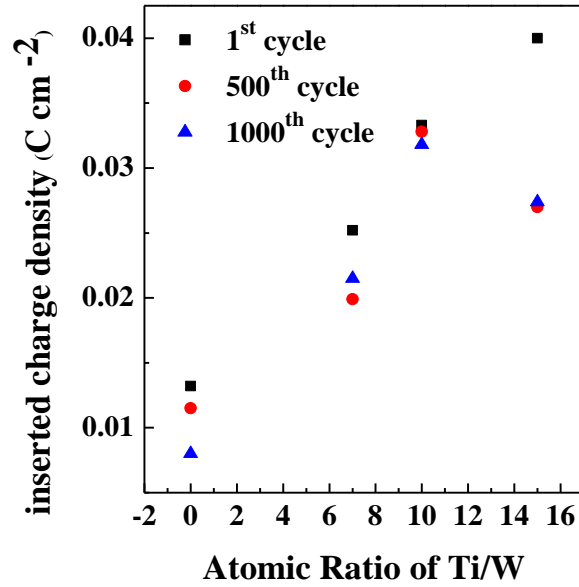


Figure 5.10 Charge accommodation capacities of WT0, WT7, WT10 and WT15 at their 1st, 500th and 1000th cycle respectively calculated from the result of Fig.5.8.

Table 5.3 List of charge densities and charge/discharge rate of all films corresponding to curves in Figure 5.8

| | 1 st | | 500 th | | 1000 th | |
|------|---------------------------------|--|---------------------------------|-------------------|---------------------------------|-------------------|
| | q_{in} mA cm ⁻² | | q_{in} mA cm ⁻² | $\Delta q_{in}\%$ | q_{in} mA cm ⁻² | $\Delta q_{in}\%$ |
| WT0 | 13.2 | | 11.5 | -13 | 8 | -39 |
| WT7 | 25.2 | | 19.9 | -21 | 21.5 | -15 |
| WT10 | 33.3 | | 32.8 | -2 | 31.8 | -5 |
| WT15 | 40.0 | | 27 | -33 | 27.4 | -32 |

| | 1 st | | 500 th | | 1000 th | |
|------|---|-------------------|---|-------------------|---|-------------------|
| | r_{in} mA cm ⁻² s ⁻¹ | $\Delta r_{in}\%$ | r_{in} mA cm ⁻² s ⁻¹ | $\Delta r_{in}\%$ | r_{in} mA cm ⁻² s ⁻¹ | $\Delta r_{in}\%$ |
| WT0 | 0.3 | | 0.3 | -- | 0.2 | -- |
| WT7 | 0.6 | 2 | 0.5 | 2 | 0.5 | 3 |
| WT10 | 0.8 | 3 | 0.8 | 3 | 0.8 | 4 |
| WT15 | 1.0 | 3 | 0.7 | 2 | 0.7 | 3 |

q_{in} denotes the intercalated charge densities related to the CV curve in Figure 5.8;

$\Delta q_{in}\%$ is the difference between the inserted charges at the 500th cycle or 1000th cycle and that at the first cycle;

r_{in} equals to the amount of charges inserted into thin films per second. The

measured

charge insertion and extraction period was 40 seconds and 70 seconds respectively;

$\Delta r_{in}\%$ is the charge rate ratio between the films with titanium and pure WO_3 thin film.

A further inspection of the first cycle of CV in Figure 5.9(a), it shows that the anodic peak position is shifted negative and the peak current density increases as the amount of titanium in the film increases, suggesting an energetically more favorable and faster de-intercalation process with optimized atomic ratio of Ti/W.^[32] Based on the CV test, the estimated chemical diffusion coefficient (D) of these films can be calculated by using the Randles-Sevcik equation:

$$I_{pc} = 0.4463nFCA \cdot \sqrt{\frac{nFvD}{RT}} \quad (5.2)$$

where I_{pc} is the cathodic peak current density estimated from Figure 5.8(e); n : the number of inserted Li^+ ions involved in reducing 1 mol WO_3 (i.e. $n = 1$); F is Faraday constant, ¹; C is the concentration of Li^+ ions in the solution. (i.e. $C = 1 \text{ mol dm}^{-3}$); A is the area of the working electrode, making an assumption of a condensed surface; v is the scan rate during the cyclic voltammetry test (i.e. $v = 50 \text{ mV s}^{-1}$); R is the universal gas constant and; T is the absolute temperature.

Figure 5.11 reveals that WT10 has the largest chemical diffusion efficiency of the five films and this is agreement with its superior ion storage capacity discussed above.

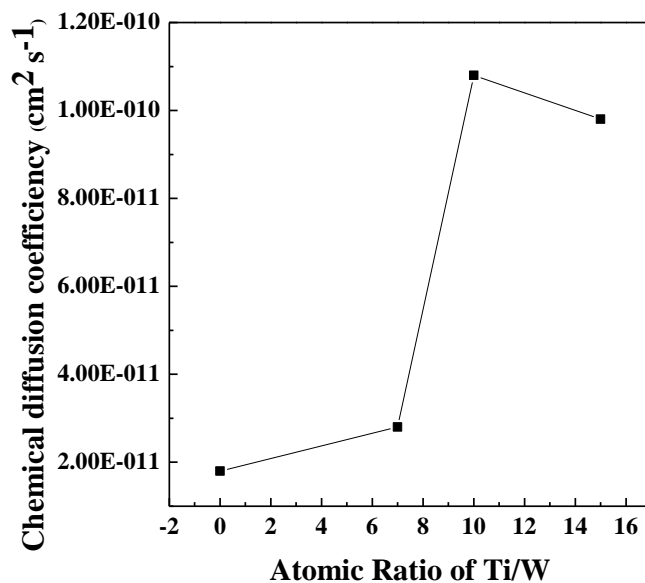


Figure 5.11 Comparison of chemical diffusion coefficient calculated from the respective cyclic voltammograms at their first cycle based on the Randles-Sevcik equation. ^[49]

5.2.4 Electrochromic properties

Figure 5.12 shows chronoamperometric curves obtained by applying potential pulses of -1V or 1V vs. Ag/Ag⁺ in 1M LiClO₄ dissolved in propylene carbonate for 50 s or 150 s respectively. Based on their respective first cycle chronoamperometric curve the reversibility of the electrochromic process in the WT0, WT7, WT10 and WT15 films is calculated to be 94%, 88%, 100% and 86% respectively, implying that the optimized ratio Ti/W is ca.10%. For the WT10 film, it seems that virtually all inserted Li⁺ can be extracted during the reversed electrochemical process. In the work reported by Patil *et al.*,^[33] they found that the reversibility of films produced by spray deposition was increased dramatically from 69% to 96% with an increase of titanium content from 13% to 38% (volume ratio of titanium precursor over tungsten precursor). In the

present case, an optimum reversibility is found in the WT10 film, for which a possible reason is its nano-flake morphology that exhibits large pore diameters providing more convenient channels for charge transport.

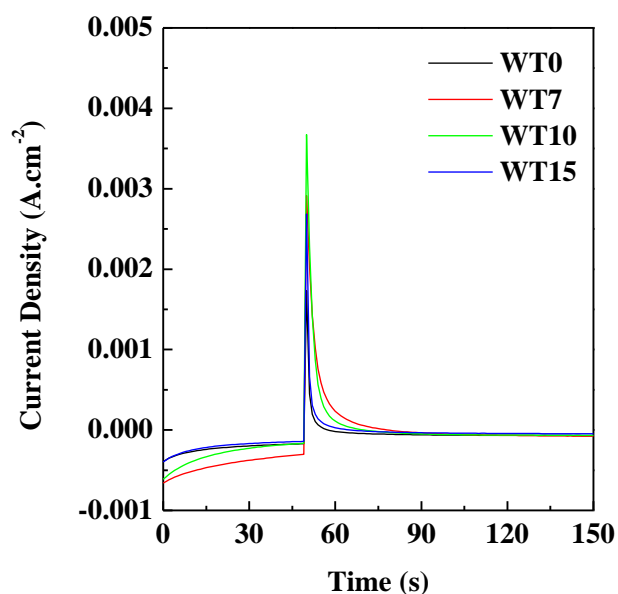


Figure 5.12 Chronoamperometric measurements performed by applying alternative potentials of -1 V for 50 s followed by 1 V for 150 s, i.e. coloration and bleaching respectively, in 1M LiClO₄ dissolved in propylene carbonate.

Figures 5.13 and 5.14 displays the corresponding optical images and related kinetic transmittance changes at 550 nm, 632.8 nm and 800 nm respectively.

From the optical image, the color of deep blue comes from the charge injection and fading of color is caused by extraction of charges. Through visual observation, WT10 performs the highest color contrast indicating superior electrochromic properties.

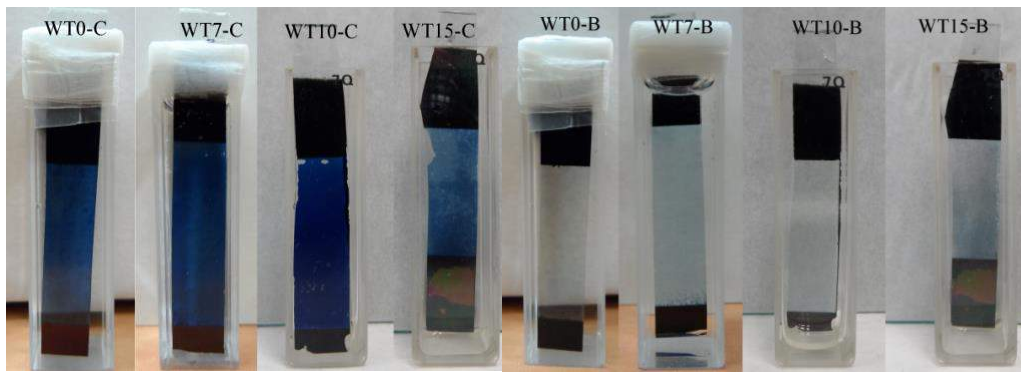
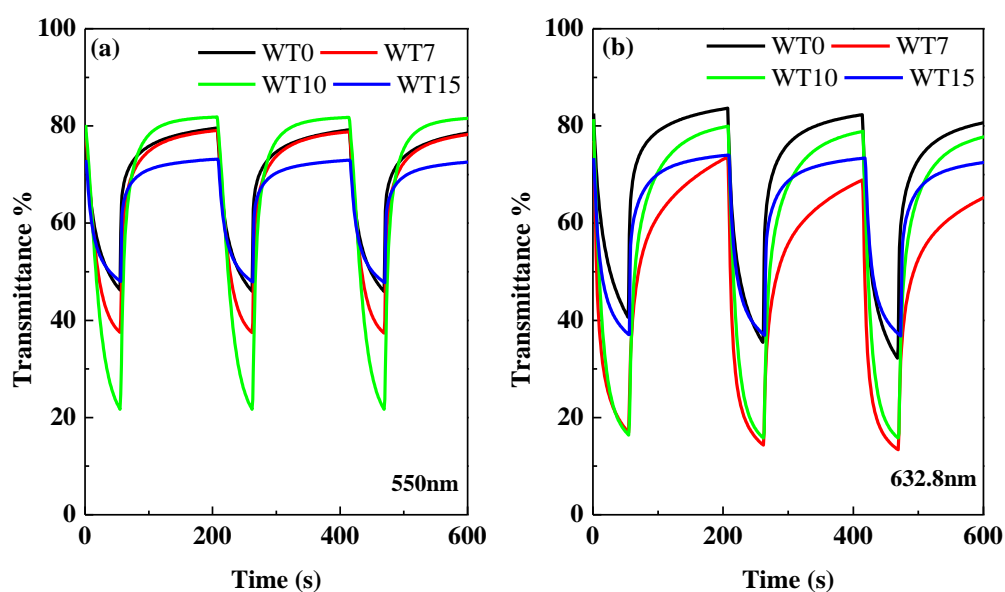


Figure 5.13 Photo images of the films at their colored (left) and bleached (right) states. The films are placed in traditional three electrode cell containing 1M LiClO₄ dissolved in propylene carbonate and supplied negative potential of -1 V for 50 s, followed by positive potential of 1 V for 150 s. The suffix character of C or B in the figure denotes color and bleach state respectively.

Figure 5.14 reflects the change of the transmittance at selected wavelengths related to color/bleach process. Through comparison, it can be seen that the addition of titanium is advantageous in producing a deeper blue color compared with the pristine WO₃ thin film. This agrees with CV tests in which the capacitance of the thin film increases with the increasing titanium contents. In addition, the transmittance of WT7 and WT10 is close to zero after coloration at the wavelength of 800nm, indicating an improvement in light absorption near the NIR range, which is vital for efficient cooling of buildings. This could be caused by a defect energy level formed within the forbidden band gap of TiO₂ doped WO₃ thin films resulting in a decrease of the band gap during the calcination process^[34-35] Furthermore, for all three wavelengths investigated WT10 exhibits the largest transmittance change range of 58.5%, 72% and 77.7% at the wavelength of 550 nm, 632.8 nm and 800nm respectively, which are 1.8, 1.7 and 2.1 times higher than the pure WO₃ thin film at the corresponding

wavelength.

Comparing with films presented in Chapter 4, Section 4.2.7, WT0 (anodized in aqueous solution) shows a larger transmittance change range than the pure WO_3 thin film anodized from ethylene glycol solution. Likewise a comparison between the aqueous WT10 with the TiO_2 doped WO_3 thin film in Chapter 4 (also contain ca. 10 at.% Ti) shows that the two exhibit equivalent abilities to regulate visible light but the former (WT10) is better within the NIR range.



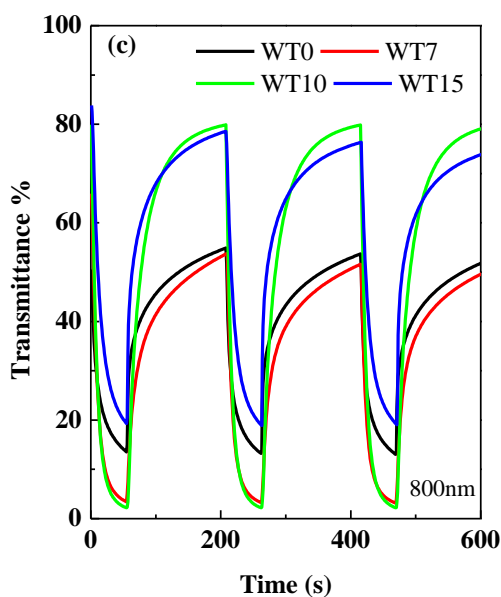


Figure 5.14 *In situ* transmittance corresponding to Figure 5.10 recorded at a wavelength of (a) 550nm, (b) 632.8nm and (c) 800nm.

The transmittance change range of each thin film at selected wavelength and respective dynamic electrochromic process parameters have been calculated and are listed in Table 5.4. By analyzing the kinetic features of each film through calculating their respective coloration/bleach time (defined as the time required for a 90% change within the full transmittance change range), it can be seen that the average coloration time for the pure WO_3 is ca. 35 s regardless of the wavelength. The addition of titanium has few impacts at 550 nm, but at longer wavelengths the coloration time of WT10 is reduced to 10 s at a wavelength of 800nm. However, if too much titanium is added this advantage is lost, since the coloration time of WT15 is the same as WT0 at 800 nm. In addition, WT10 also displays a shorter coloration time than the TiO_2 doped WO_3 thin film, anodized in ethylene glycol solution in chapter 4, at all the wavelengths investigated.

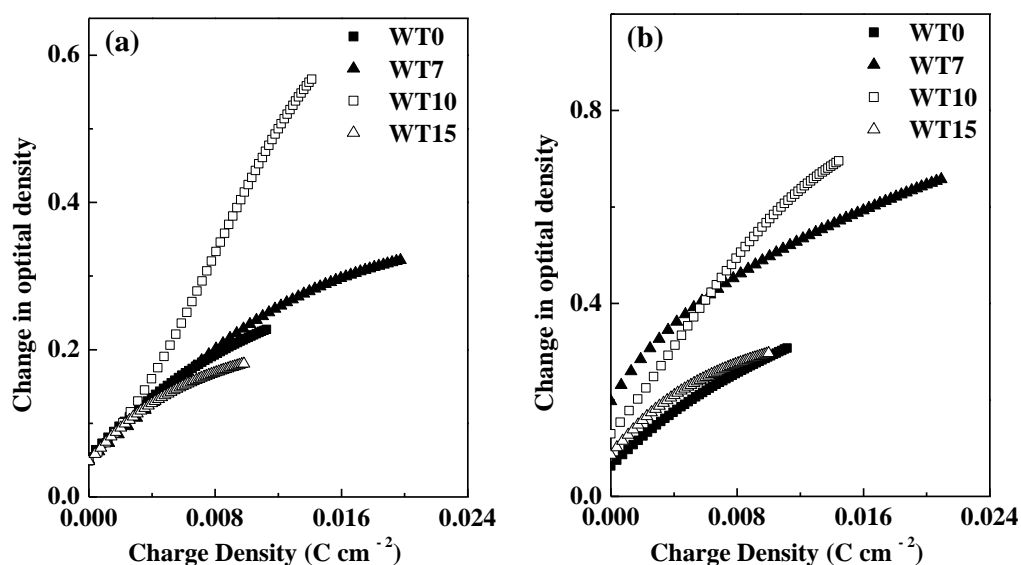
The improvement in the coloration rate of WT7 and WT10 films over the pure WT0 film possibly comes from morphology differences. Firstly, the morphology of WT10 provides more channels for charge transport which is an important determinant of coloration time. Secondly, the nano-flake structures of WT10, takes advantages in both of the larger intercalation capacitances as discussed with the CV (Section 5.2.3) and convenient channels due to its larger pore diameter (Figure 5.2) than either WT0 or the TiO₂ doped WO₃ thin film anodized in ethylene glycol in Chapter 4. The same conclusion can be made for the bleaching time.

Table 5.4 List of optical and kinetic parameters for WT0, WT7, WT10 and WT15 obtained from Figure 5.12 at wavelengths of 550, 632.8 and 800 nm

| Wavelength nm | Transmittance Change (%) | | | CE cm ² C ⁻¹ | | | Coloration/Bleaching Time (s) | | |
|------------------|-----------------------------|-------|------|---------------------------------------|-------|-------|----------------------------------|-------|-------|
| | 550 | 632.8 | 800 | 550 | 632.8 | 800 | 550 | 632.8 | 800 |
| WT0 | 31.9 | 41.9 | 37.0 | 18.8 | 31.1 | 49.1 | 39/52 | 39/50 | 32/90 |
| WT7 | 41.1 | 59.3 | 49.7 | 19.2 | 36.5 | 75.4 | 35/32 | 28/85 | 21/90 |
| WT10 | 58.5 | 72.0 | 77.7 | 43.2 | 46.8 | 105.8 | 38/34 | 33/60 | 10/64 |
| WT15 | 25.0 | 36.4 | 64.5 | 23.5 | 33.4 | 62.8 | 35/38 | 32/48 | 32/72 |

Continuing the discussion of the electrochromic properties of the films, the coloration efficiency, as defined in Equations 3.10 and 3.11 of Chapter 3 is calculated and depicted in Figure 5.15. The calculated value of CE for each film increased with increasing wavelength. Furthermore, the extent of the increase in CE is larger for TiO₂ doped WO₃ thin films relative to the pure one at all

wavelengths, WT10 showing the largest values. This is ascribed to it having the largest transmittance change range. In addition, within the visible light range, the CE of WT7, WT10 and WT15 are 0.4/5.4 cm² C⁻¹, 24.4/15.7 cm² C⁻¹ and 4.7/2.3 cm² C⁻¹ higher than WT0 at the wavelengths of 550nm/632.8nm respectively. While, at 800 nm, CE is improved 1.5, 2 and 1.3 times for WT7, WT10 and WT15 as compared with WT0. Therefore, it can be seen that the value of CE is very sensitive to the light modulation range and the WT10 film has the best electrochromic coloration efficiency across the whole of the spectrum investigated.



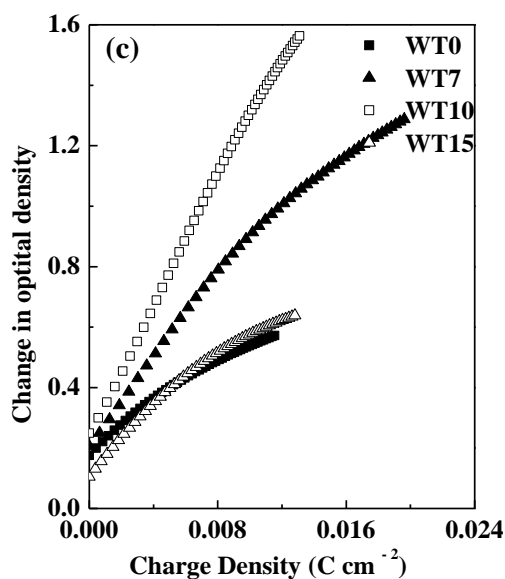


Figure 5.15 Plots of the variation of the *in situ* optical density vs. the charge density corresponding to the *in situ* transmittance in Figure 5.12 at wavelengths of (a) 550 nm, (b) 632.8 nm and (c) 800 nm.

5.2.5 Electrochemical Impedance Spectrum

Figure 5.16 depicts impedance spectra in the Nyquist format measured in 1 M LiClO₄ dissolved in propylene carbonate solution at a potential of -0.4V vs. Ag/Ag⁺. The potential is chosen according to the cyclic voltammetry tests in which the onset potential of reduction is around -0.4 volts. The equivalent circuit model is the same as depicted in Figure 3.14 of Chapter 3 Section 3.2.5.

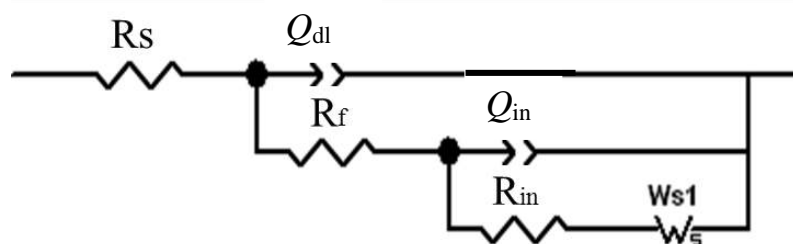


Figure 3.14 Equivalent circuits for impedance fitting, reproduced here for the convenience of the reader. The equivalent circuit model was based on the impedance data of the characterized film WT0, WT7, WT10 and WT15.

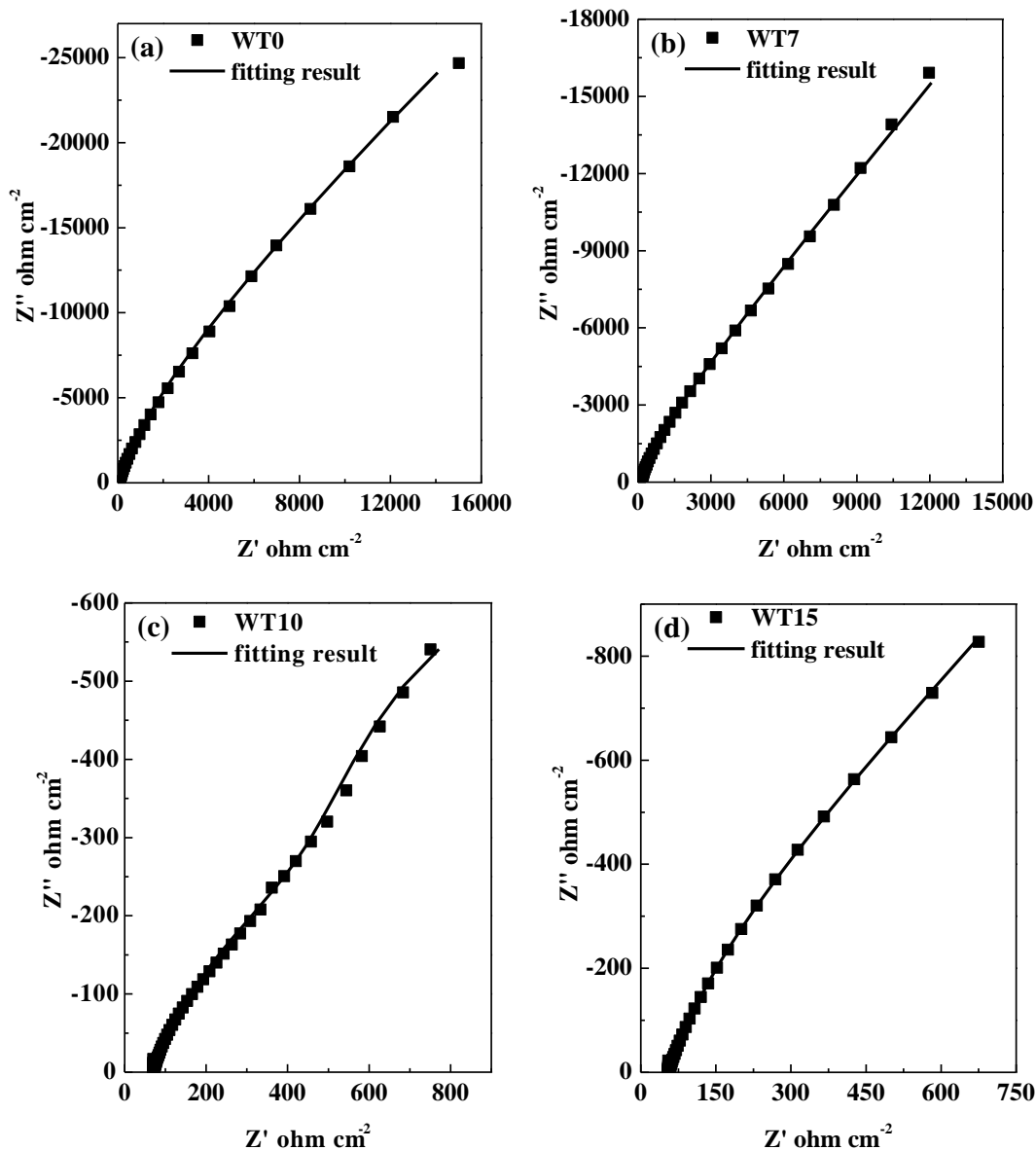


Figure 5.16 Impedance spectra of WT0, WT7, WT10 and WT15. The squares are the raw data collected and the solid lines are the fitting results.

On the basis of the fitting results in Table 5.5 it can be concluded that the incorporation of certain titanium content can reduce the charge transfer resistance symbolized by R_f effectively. This phenomenon was also observed by Park *et al* who studied TiO_2 mixed WO_3 film electrodes formed by a doctor-blading method.^[36] This is also consistent with the CV test in which a larger current density is observed with an increase in titanium content. Meanwhile, the

double layer capacity (Q_{dl}) of the samples exhibits a slightly increasing trend for the sequence WT0, WT7 and WT10, but WT15 shows a very low value. This can be attributed to the morphology of W15 with less specific area. Table 5.5 also reveals that WT10 has the lowest charge transfer and diffusion resistance, represented by R_{in} and R_w respectively, as well as the highest capacitance symbolized by Q_{in} , indicating that this sample has the optimized quantity of titanium in the film and the best morphology. These lower R_{in} and R_w values help to explain why WT10 has the fastest intercalation rate and its high Q_{in} explains why it has the largest transmittance change range (Figure 5.12). Furthermore, the diffusion coefficients calculated from τ_w which is stated in equation 3.15 shows same trend as that determined in the CV experiments and shown in Figure 5.10, assuming the differences among the thicknesses of the samples can be ignored.

Table 5.5 List of impedance fitting parameters of film WT0, WT7, WT10 and WT15

| Film | WT0 | Er% | WT7 | Er% | WT10 | Er% | WT15 | Er% |
|--|---------|------|---------|------|---------|-----|---------|------|
| R_s / $\Omega \text{ cm}^{-2}$ | 58.9 | 0.2 | 116 | 0.1 | 71.3 | 0.2 | 38.7 | 6.8 |
| R_f / $\Omega \text{ cm}^{-2}$ | 212 | 16.4 | 203 | 15.1 | 163 | 1.0 | 16.5 | 15.9 |
| R_{in} / $\Omega \text{ cm}^{-2}$ | 1.6 E+4 | 6.5 | 5.3 E+3 | 3.0 | 1.8 E+2 | 4.3 | 1.1 E+3 | 0.4 |
| Q_{dl} / $(F \text{ m}^{-2})^{1/n}$ | 1.2 E-4 | 1.0 | 1.9 E-4 | 0.8 | 9.6 E-4 | 0.9 | 8.7 E-7 | 31.7 |
| n_{dl} | 0.9 | 0.2 | 0.8 | 0.2 | 0.8 | 0.3 | 0.8 | 30.7 |
| Q_{in} / $(F \text{ m}^{-2})^{1/n}$ | 5.7 E-6 | 11.8 | 6.0 E-6 | 16.1 | 1.4 E-3 | 3.7 | 3.2 E-4 | 1.9 |
| n_{in} | 1 | 0.9 | 1 | 0.8 | 0.9 | 1.0 | 0.8 | 0.2 |
| R_w / $\Omega \text{ cm}^{-2}$ | 2.5 E+5 | 1.4 | 1.1 E+5 | 0.4 | 1.3 E+3 | 3.5 | 2.0 E+4 | 0.8 |
| τ_w /s | 447 | 2.0 | 289 | 0.7 | 52.2 | 5.8 | 302 | 0.4 |

The method of Er% calculation is stated in section 2.3 in chapter 2

5.3 Conclusions

In this chapter TiO₂ doped WO₃ thin films have been produced by anodization of co-sputtered Ti/W containing 0 – 15 at. % titanium in a fluorinated aqueous electrolyte. After annealing the tungsten and titanium element in all films are totally oxidized with valence of +6 and +4 respectively. SEM images revealed that the films exhibit a morphology evolution from nano-porous structure, undergoing nano-flake, to nano-block decorated porous structure as a sequence of WT0, WT7, WT10 to WT15. Both XRD and Raman spectrum results reveal that the higher the quantity of incorporated titanium the lower the crystallinity.

Through comparing the electrochromic property of these films, WT10 displays the best durability and superior capacity in adjusting the transmittance within the visual light, especially near the NIR range. Besides, WT10 shows shorter coloration/bleach time and the highest coloration efficiency. Furthermore, analysis by electrochemical impedance spectroscopy implies that the TiO₂ dopants reduce the charge transfer and diffusion resistances with minima being found for 10 at.% Ti, which explains the fast dynamic behavior on electrochromic applications of the WT10 sample.

References:

- [1] N. Mukherjee, M. Paulose, OK Varghese, G. K. Mor, C. A. Grimes, *J. Mater. Res.*, **18** (2003) 2296.
- [2] F. Di Quarto, A. Di Paola, and C. Sunseri, *Electrochim. Acta*, **26** (1981) 1177.
- [3] J. L. Ord, D. J. De Smet, *J. Electrochem. Soc.* **139** (1992) 359.
- [4] H. Tsuchiya, J. M. Macak, I. Sieber, L. Taveira, A. Ghicov, K. Sirotna, P. Schmuki, *Electrochem. Commun.* **7** (2005) 295.
- [5] M. Yang, N. K. Shrestha, P. Schmuki, *Electrochem. Commun.* **11** (2009) 1908.
- [6] A. Z. Sadek, H. Zheng, M. Breedon, V. Bansal, S. K. Bhargava, K. Latham, J. Zhu, L. Yu, Z. Hu, P. G. Spizzirri, W. Wlodarski, K. Kalantar-Zadeh, *Langmuir* **25** (2009) 9545.
- [7] C. Ng, C. Ye, Y.H. Ng, R. Amal, *Cryst. Growth Des.* **10** (2010) 3794.
- [8] Y. Chai, C. W. Tam, K. P. Beh, F. K. Yam, Z. Hassan, *J Porous Mater*, **20** (2013) 997.
- [9] H. D. Zheng, Abu Z. Sadek, K. Latham, K. Kalantar-Zadeh, *Electrochem. Commun.* **11** (2009) 768.
- [10] S. Caramori, V. Cristino, L. Meda, A. Tacca, R. Argazzi and C.A. Bignozzi, *Energy Procedia* **22** (2012) 127.
- [11] R. S. Lillard, G. S. Kanner, D. P. Butt, *J. Electrochem. Soc.* **145**

(1998) 2718

- [12] A. D. Paola, F. D. Quarto, C. Sunseri, *Corros. Sci.* **20** (1980) 1067.
- [13] *Pourbaix Diagrams*
- [14] International Centre for Diffraction Data (ICDD) Card No. 00-005-0364.
- [15] K. J. Lethy, D. Beena, V. P. Mahadevan Pillai, V. Ganesan, V., *J. Appl. Phys.* **104** (2008) 033515.
- [16] Y. Shigesato, *Jpn. J. Appl. Phys.*, Part 1 **30** (1991) 1457
- [17] G. Gouadec, P. Colombari, *Prog. Cryst. Growth Charact. Mater.* **53** (2007) 1.
- [18] P. C. Liao, C. S. Chen, W. S. Ho, Y. S. Huang, K. K. Tiong, *Thin Solid Films*, **301** (1997) 7.
- [19] A. Portinha, V. Teixeira, J. Carneiro, M. F. Costa, N. P. Barradas, A.D. Sequeira, *Surf. Coat. Technol.* **107** (2004) 188
- [20] B. D. Cullity, *Elements of X-ray Diffraction*, Addison-Wesley, Reading, 1978.
- [21] L. Dikit, D. L. Gerad, H. J. Bowley, *Appl. Spectrosc. Rev.* **22** (1986) 189.
- [22] S. P. S. Porto, P. A. Fleury, T. C. Damen, *Phys. Rev.* **154** (1967) 522.
- [23] X. H. Yang, Z. Li, G. Liu, J. Xing, C. H. Sun, H. G. Yang and C. Z. Li, *Cryst. Eng. Comm.*, **(13)** 2011 1378.¹
- [24] M. Hepel, S. Hazelton, *Electrochim. Acta*, **50** (2005) 5278.
- [25] H. L. Zhang, D. Z. Wang, N. K. Huang, *Appl. Surf. Sci.*, **34** (1999) 150.
- [26] R.G. Palgrave, I.P. Parkin, *J. Mater. Chem.* **14** (2004) 2864.
- [27] F.J. Himpsel, J.F. Morar, F.R. McFeely, R. Pollak, G. Hollinger, *Phys. Rev. B* **30** (1984) 7236.
- [28] J. H. Pan, W. I. Lee, *Chem. Mater.* **18** (2006) 847.
- [29] C.W. Lai, S. Sreekantan, P.S.E.W. Krenghvirat, *Electrochim. Acta* **77** (2012) 128..
- [30] F. S. Manciu, Y. Yun, W. G. Durrer, J. Howard, U. Schmidt, C. V. Ramana, *J. Mater. Sci.*, **47 (18)** (2012) 6593.
- [31] Md. Imteyaz Ahmad and S. S. Bhattacharya, *Appl. Phys. Lett.* **(95)** 2009 191901
- [32] J. Z. Ou, S. Balendhran, M. R. Field, D. G. M. Culloch, A. S.

- Zoolfakar, R. A. Rani, S. Zhuiykov, A. P. O'Mullane, K. Kalantar-Zadeh, *Nanoscale*, **4** (2012) 5980.
- [33] P. S. Patil, S. H. Mujawar, A. I. Inamdar, S. B. Sadale, *Appl. Surf. Sci.* **250** (2005) 117.
- [34] C. S. Fu, C. Lei, G. Shen, C. G. Yu, *Powder Technol.* **160** (2005) 198.
- [35] Y. P. He, Z. Y. Wu, L. M. Fu, C. R. Li, Y. M. Miao, L. Cao, H. M. Fan, B. S. Zou *Chem. Mater.*, **15** (2003) 4039.
- [36] H. Park, A. Bak, T. H. Jeon, S. Kim, W. Choi, *Appl. Catal. B: Environ.*, **115-116** (2012) 74.

Chapter 6 Conclusions

Tungsten trioxide (WO_3) has been intensely investigated since the first discovery of its electrochromic properties in 1815. Many methods have been used for the fabrication of WO_3 films with different morphologies. Among all these methods, the hydrothermal treatment is attractive due to its facile and cost effective features. Although many researchers have made significant contributions on synthesizing pure WO_3 powder or films by adopting hydrothermal method for the electrochromic application, there are some drawbacks, such as relative low light modulation range, that need to be improved for its applications on smart windows. Therefore, the mixing or doping of a second transition metal oxide having electrochromic functions is adopted in this thesis. According to the reported studies, TiO_2 is a favorable candidate for doping with WO_3 based on its positive effect on increasing film reversibility and stability.^[1-2] However, to obtain the TiO_2 doped WO_3 thin film on conductive glass substrates with one step hydrothermal method for investigating the related electrochromic properties has not been previously reported. Therefore, in Chapter 3, the morphology, structure and corresponding electrochromic properties of TiO_2 doped WO_3 thin film on FTO glass synthesized by hydrothermal method was discussed and can be summarized from three aspects.

1. The synthesized TiO_2 doped WO_3 thin film by using hydrothermal

method in this work showed a two layer structure consisting of nanopillars on top of a compact layer, with both layers having the same Ti/W atomic ratio of 4:1. It was postulated that the switch from growth of the compact layer to nanopillars was due to hydrothermal reaction becoming mass transport limited at the oxide / electrolyte interface.

2. In chapter 3, XRD investigations revealed that the TiO₂ doped WO₃ thin film, obtained by hydrothermal method, kept the same structure as pure WO₃ thin film after comparing the XRD patterns between each other, showing a preferential growth of (002) plane and good crystallinity with hexagonal crystallographic structure. XRD and TEM investigations suggested that the TiO₂ doped WO₃ thin film was achieved by replacement of W⁶⁺ by Ti⁴⁺ ions in the WO₃ lattice structure, rather than discrete phases of WO₃ and TiO₂.
3. The TiO₂ dopant was found to improve the electrochromic properties as compared to the pure WO₃ films. This included more than doubling the transmittance change range at 632.8 nm to 67%, increasing the coloration efficiency by 50% to 39.2 cm² C⁻¹ and approximately doubling the coloration and bleaching rate relative to pure WO₃ thin film. The electrochemical impedance measurements suggested that the improvement in the electrochromic properties were due to the presence of the TiO₂ reducing both the film's electrical resistance and resistance to diffusion of charges within the film. Additionally, the stability of the TiO₂ doped WO₃ thin film was improved, with only limited degradation being observed after 1000 cycles of coloration/bleaching circulation, compared to significant degradation in pure WO₃ thin film only after 500 cycles.

Under the enlightenment of the advantages on the TiO₂ doped WO₃ thin film

from the results of Chapter 3, a continued investigation was developed through using electrochemical anodization, which is easier to scale-up for industrial applications than the hydrothermal method. Chapters 4 and 5 demonstrated the electrochromic properties of anodized co-sputtered Ti/W thin films which were produced from organic and aqueous electrolyte solutions respectively. From the results exhibited in these two chapters an overall conclusions can be stated as follows.

1. Through comparing the morphology of pure WO_3 and TiO_2 doped WO_3 thin film obtained from organic and aqueous solution respectively, it was found that changes were more drastic in the latter where the morphology evolved from nano-porous, to nano-flake and finally nano-block interweaved porous network as the titanium content increased. In both Chapters 4 and 5 the preferential growth orientation seems sensitive to the addition of titanium as this disappeared in the TiO_2 doped WO_3 thin film. However, the crystal structures in both case favor monoclinic due to the same heat treatment conditions but hexagonal crystallographic structure was observed for hydrothermally produced thin films in Chapter 3.
2. As with the hydrothermal method XRD and TEM investigations of the anodized films suggested that the TiO_2 doped WO_3 thin film was achieved by replacement of W^{6+} by Ti^{4+} ions in the WO_3 structure, rather than discrete phases of WO_3 and TiO_2 .

3. In Chapter 5, both XRD and Raman spectroscopy results revealed that the higher the quantity of incorporated titanium the lower the crystallinity. This phenomenon was also observed when comparing pure WO_3 thin film with TiO_2 doped WO_3 thin film synthesized by hydrothermal method.
4. XPS spectroscopy proved that the valence of tungsten and titanium elements in both as-prepared pure WO_3 and TiO_2 doped WO_3 thin film were 6+ and 4+ respectively without any traces of alternative valences.
5. Through comparing the capacitances, electrochromic properties and electrochemical impedance spectra among all thin films, the data showed that the optimum atomic percentage of mixed titanium contents was around 10 at.% which exhibited obvious improvements in these aspects:
 - First for the films anodized in an aqueous environment WT10 displayed best durability only having a loss of charge capacitance of 5% after 1000 cycles, contrasting with 39.4%, 14.6% and 31.5% for WT0, WT7 and WT15 respectively.
 - The TiO_2 doped WO_3 thin film anodized in ethylene glycol and also have ca. 10 at.% Ti, in Chapter 4, which lost 26% of its charge capacitance after 1000 cycles, also exhibited better durability than

pure WO₃ thin film 51%, but worse than WT10 possibly due to the thicker thickness of films in chapter 4. Therefore, the inserted charges cannot be extracted totally within the same discharge period; hence these impede the insertion of charges in later cycles.

- The WT10 film exhibited superior transmittance modulation ability of 58.5%, 72% and 77.7% at 550 nm, 632.8 nm and 800 nm respectively, which was 26.6%, 30.1% and 40.7% higher than WT0. In addition, WT7 and WT15 also illustrates significant improvement on transmittance change range within the NIR range, indicating that the addition of titanium contents assists in promoting the absorption of the light within NIR range.
 - The WT10 also provided shorter coloration/bleach time of 38 s/34 s, 33 s/60 s and 10 s/64 s respectively compared with 39 s/52 s, 39 s/50 s and 32 s/90 s of WT0. Furthermore, the electrochemical impedance spectroscopy implied that the titanium oxide has positive impact by reducing the charge transfer and diffusion resistance.
6. Finally, a comparison of the properties between WT10 and the TiO₂ doped WO₃ thin film anodized from organic solutions (O-WO₃/TiO₂) showed that, firstly, the charge capacitance of O-WO₃/TiO₂ thin film was 0.05 C cm⁻² higher than WT10 at the first cycle, which was likely

ascribed to the film thickness differences. Secondly, the transmittance change (ΔT) was almost the same for both films except the ΔT at 800 nm. WT10 was 8 % higher than O-WO₃/TiO₂ thin film due to the essential lower transparency of the later film. Thirdly, the coloration time of WT10 was shorter than O-WO₃/TiO₂ thin film, but it has a longer bleach time. The shorter coloration time was originated from the smaller capacitance respect to O-WO₃/TiO₂ thin film, thinner thickness and spacious charge transport channels observed from respective SEM images. However the shorter bleach time observed in O-WO₃/TiO₂ thin film benefited from the pores penetrating to the substrate.

References

- [1] H. Matsuoka, S. Hashimoto, H. Kagechika, *Hyomen Gijutsu, J. Surface Finish. Soc. Jpn*, **42** (1991) 246
- [2] S. Hashimoto, H. Kagechika, *J. Electrochem. Soc.*, **138** (1991) 2403.

Chapter 7 Suggestions on future research work

To further understand the TiO₂ doped WO₃ system, investigation on its structure such as structure refinement can be considered. Besides, for applications, the design of electrochromic device and looking for other alternative materials focusing on shortening electrochromic response time should be studied in next steps.

1, Study further on the arrangement of the mixed Ti atoms in W matrix after co-anodization by doing simulations and the structural refinement in order to find the accurate role of mixed Ti in the evolution of the structures during the co-anodization process.

2, In addition to WO₃, viologens have also attract intensive interesting due to their property of high contrast and fast kinetic process on electrochromic display applications. Viologens are derivatives of 4,4'-bipyridyl. Based on recent literature, the studies on viologen-based electrochromism have been combined with TiO₂ by confining viologen molecular on surface of TiO₂ nanotubes. Therefore, in the future work the investigation of viologen/WO₃ and viologen/WO₃ /TiO₂ electrochromic systems could be developed by coating a monolayer of self-assembled, phosphonated, chemisorbed viologen molecules on the electrodeposited or anodized oxide thin film. Under the consideration of commercial application, the industry standard printing techniques, such as

flexographic, screen and inkjet, could be applied on producing the viologen/ WO_3 electrochromic thin films.

3, A solid system will be more flexible and show better resistance to mechanical shock. Therefore, the fabrication of solid EC device by replacing aqueous solutions with ion containing sol-gel electrolyte, such as polystyrene sulfonic acid, on the studied WO_3/TiO_2 system above will be another interested topic.